

Investigations for Robust and Low-Power Heartbeat Sensing using Wearable,  
Implantable and Doppler-based Non-Contact Bio-Sensors

by

Vighnesh Rudra Das, B.E

A Thesis

In

ELECTRICAL ENGINEERING

Submitted to the Graduate Faculty  
of Texas Tech University in  
Partial Fulfillment of  
the Requirements for  
the Degree of

MASTER OF SCIENCE

IN

ELECTRICAL ENGINEERING

Approved

Dr. Donald Y.C. Lie

Dr. Mary Baker

Dominick Casadonte  
Dean of the Graduate School

December, 2012

Copyright 2012, Vighnesh Rudra Das

## ACKNOWLEDGMENTS

First and foremost, I humbly thank the omniscient and omnipresent *Divinity*.

I owe my sincere gratitude to my advisor Dr. Donald Lie for the continuous support throughout the study and research for my MS program. His patience, motivation, encouragement, enthusiasm, and immense knowledge were the guiding light in my academic pursuits. His quest for excellence has always motivated me and made me strive towards my goal. I am obliged to him for providing me the opportunity to be a part of his research endeavors in the bio-medical field.

During my research I found a great mentor in Dr. Jerry Lopez, whose insightful ideas and suggestions always helped me to be focused and determined towards my goal. His technical acumen aided my research work and made me develop a better technical understanding.

I would like to make a special mention of Mr. Yen-Ting Liu, whose supportive nature and deep understanding of analog design made me comprehend various fundamental concepts and helped me shape my research. I am extremely pleased to convey my heartfelt appreciation to Mr. Weibo Hu, Mr. Alex Boothby, Mr. Cliff Schecht, Mr. Royce Hwang, Mr. Jerry Tsay and Mr. Ruili Wu for their valuable help during my research as well.

I sincerely thank Dr. Mary Baker for generously accepting to serve on my thesis examination committee. I am grateful to her for introducing me to the field of bio-medical signals and signal processing, which helped my research work immensely.

I thank my father Dr. Rudra Pratap Das, for the constant inspiration and encouragement which developed the interest in me towards research. I would also like to thank my family and friends for their good wishes. Finally, I express my deepest appreciation to my wife Lubna, whose absolute trust and unflinching support made it possible for me to pursue my research goals.

## TABLE OF CONTENTS

<b>ACKNOWLEDGMENTS</b> .....	<b>ii</b>
<b>TABLE OF CONTENTS</b> .....	<b>iii</b>
<b>ABSTRACT</b> .....	<b>v</b>
<b>LIST OF TABLES</b> .....	<b>vi</b>
<b>LIST OF FIGURES</b> .....	<b>vii</b>
<b>1. INTRODUCTION</b> .....	<b>1</b>
1.1 Wearable ECG Sensors .....	3
1.1.1 Electrodes – Wet, Dry and Capacitive Coupled .....	3
1.1.2 Components of the wearable ECG sensor system .....	7
1.2 Implantable Cardioverter Defibrillator (ICD) .....	9
1.2.1 Defibrillation.....	11
1.2.2 Electrodes and Lead-assembly .....	13
1.2.3 Components of the ICD system.....	15
1.3 Doppler-Based Non-Contact Vital Signs (NCVS) Sensor.....	18
1.3.1 Doppler-radar principle for NCVS sensor .....	19
1.3.2 Quadrature receiver and arc-tangent demodulation for NCVS sensors .....	23
1.3.3 Direct-conversion receiver and range correlation in NCVS sensors .....	25
1.3.4 Generations of NCVS sensor at Dr. Lie’s Group in Texas Tech .....	27
1.4 Summary of Heart Beat Sensing Techniques.....	31
<b>2. ANALOG FRONT-END DESIGN AND SIMULATION OF BIO-SENSOR: ECG and ICD/PACEMAKER</b> .....	<b>33</b>
2.1 Biosignal Instrumentation Amplifier (INA) .....	35
2.1.1 Design Consideration.....	37
2.2 Chopper Stabilization Technique.....	39
2.2.1 Noise Analysis – Chopper Stabilization .....	41
2.3 Differential Difference Amplifier based chopper stabilized INA.....	44
2.3.1 Differential Difference Amplifier (DDA).....	45
2.3.2 Chopper Switches .....	47
2.3.3 DDA-based chopper stabilized INA – Circuit and System Design.....	47
2.3.4 DDA-based chopper stabilized INA – Simulation.....	54
2.3.5 Achieved specifications by simulation .....	58
2.3.6 Noise Efficiency Factor (NEF).....	59
2.3.7 State-of-the-art performance comparison .....	60
2.4 Low-noise design paradigm .....	62
2.5 Fully-differential folded-cascode based chopper stabilized INA.....	64
2.5.1 Folded-cascode OTA with current scaling technique.....	66
2.5.2 Design considerations for current scaling technique.....	68
2.5.3 Device sizing using $g_m/I_D$ method .....	71
2.5.4 Chopper modulation .....	72
2.5.5 Switch-capacitor-based common-mode feedback circuit .....	73
2.5.6 Fully-differential chopper-stabilized INA - simulation .....	75
2.5.7 Simulated performance comparison.....	82

2.5.8 State-of-the-art-performance comparison.....	83
<b>3. ANALOG FRONT-END CIRCUITS AND SYSTEM CHARACTERIZATION AND TESTING OF BIO-SENSOR: ECG AND ICD/PACEMAKER.....</b>	<b>84</b>
3.1 Setup for die characterization.....	84
3.2 Measurement results for the DDA-based chopper stabilized INA.....	86
3.3 Measurement results for the fully differential folded cascode-based chopper stabilized INA .....	89
3.4 Electrocardiogram (ECG or EKG) measurement .....	92
<b>4. ANTENNA EVALUATION OF A NON-CONTACT VITAL SIGNS (NCVS) SENSOR FOR CONTINUOUS HEART AND RESPIRATION RATES MONITORING .....</b>	<b>100</b>
4.1 NCVS system for the antenna evaluation at Dr. Lie's lab .....	101
4.2 Phase noise and Range Correlation.....	103
4.3 Antenna characterization - Directivity and Radiation patterns .....	105
4.4 NCVS system based antenna evaluation setup .....	112
4.5 Experimental results and analysis .....	116
<b>5. CONCLUSION AND FUTURE WORK .....</b>	<b>121</b>
5.1 Future Work .....	122
5.1.1 dc-servo loop (DSL) for electrode offset reduction .....	122
5.1.2 Active grounding for ECG measurements .....	123
5.1.3 System-on-a-Chip (SoC) realization of the NCVS system .....	123
5.1.4 Harmonic Cancellation for the NCVS sensor system .....	124
<b>REFERENCES .....</b>	<b>125</b>

## ABSTRACT

The research and development for robust, accurate and power-efficient sensors for the *continuous monitoring* of physiological vital signs of patients is of great importance. For example, accurate and continuous heart rate monitoring will not only provide key medical insights regarding the individual's heart conditions, but it may also be critically important in providing life-saving treatments and therapies. This thesis, therefore, presents a study on several robust and low-power techniques for continuous heartbeat sensing using: (1) a wearable electrocardiogram (ECG) sensor; (2) an implantable cardioverter defibrillator (ICD); and (3) a Doppler-based non-contact vital signs (NCVS) bio-sensor.

To realize effective wireless-assisted-living solutions and provide reliable ambulatory healthcare, low power and miniature cardiac monitoring sensor systems are essential. In this context, low-power and low-noise instrumentation amplifiers (INAs) were studied and designed to be a part of the bio-sensor analog front end (AFE) integrated circuit (IC). Circuit techniques and topologies for low-power and low-noise design were used to realize CMOS INAs, which would enable robust and battery friendly ECG bio-sensors. This thesis discusses the circuit design techniques, and presents the simulation and measurement results of the low-power CMOS INAs with and without the chopper techniques to reduce the  $1/f$  noise.

Doppler-based non-contact vital signs (NCVS) bio-sensor was also investigated for reliable and robust detection of heart rate. On the system level, the antenna evaluation of the non-contact vital sensor has been explored to understand the relationship between the antenna characteristics and heart-rate detection accuracy. The original PCB-based NCVS sensor system used in the study was designed by former students of our group, but this thesis reports the various efforts to make the system more reliable and robust.

## LIST OF TABLES

1.1 Heart beat sensing techniques – a comparison.....	32
2.1 Biosignal : Amplitude and Frequency range.....	34
2.2 Design Specification .....	39
2.3 Noise Response (without chopper stabilization).....	54
2.4 Noise Response (with chopper stabilization).....	55
2.5 Simulated INA Frequency Response (with chopper stabilization).....	56
2.6 Achieved Specification by Simulation (with chopper stabilization).....	58
2.7 State-of-the-art performance comparison. ....	60
2.8 Device sizing.....	71
2.9 Noise Simulation Comparison .....	79
2.10 Topological Comparison (post-layout simulation) .....	82
2.11 Performance Comparison (post-layout simulation) .....	82
2.12 State-of-the-art performance comparison .....	83
3.1 Summary of our 0.35 $\mu$ m CMOS INA performance in TI LBC7.....	89
4.1 Phase noise performance comparison .....	105
4.2 Basic antenna characteristics based on the radiation patterns.....	106
4.3 Antenna characteristics based on the radiation patterns. ....	112
4.4 Inter-quartile Range (IQR) for different antennas based on Fig. 4.11 .....	117
4.5 Measured accuracy table for the non-contact vital signs system based on different antennas (for front readings only) .....	117
4.6 Inter-quartile Range (IQR) for different antennas based on Fig. 4.13 .....	119
4.7 Measured accuracy table of NCVS system for the gain-equalization experiment (for front readings only) .....	120

## LIST OF FIGURES

1.1 Representation of a normal ECG signal.....	2
1.2 Equivalent circuit of an electrode placed on skin. ....	4
1.3 (a) Cross-sectional view of the epidermis. (b) Depicting the use of conical and diamond-shaped dry electrodes .....	6
1.4 Electrode body interface with equivalent electrical circuit.....	7
1.5 A typical wearable ECG sensor system .....	9
1.6 An Implantable Cardioverter Defibrillator (ICD) inside a human heart.....	11
1.7 Intra-cardiac transvenous leads:.....	14
1.8 A typical modern ICD/pacemaker system .....	17
1.9 A typical Doppler-radar based NCVS sensor .....	19
1.10 Simplified depiction of Doppler-radar principle used for NCVS sensor .....	21
1.11 Range-correlation in a direct-conversion Doppler-based NCVS sensor .....	26
1.12 The four generations of NCVS sensor hardware developed at Prof. Donald Lie’s Lab at the Texas Tech University .....	29
2.1 A typical wearable ECG sensor showing the AFE circuitry.....	34
2.2 Electrode-electrolyte interface. ....	35
2.3 Electrode-INA interface, showing the electrode impedance and electrode offsets .....	37
2.4 Chopper stabilization technique.....	40
2.5 Chopper modulation of noise.....	41
2.6 Spikes due to chopper modulation .....	44
2.7 DDA-based INA.....	45
2.8 DDA symbol .....	45
2.9 The DDA operation principle.....	46
2.10 The chopper switches design schematics.....	47
2.11 A block diagram of the proposed chopper stabilized INA.....	48
2.12 The schematics of the chopper stabilized DDA-INA .....	49

2.13 The schematics of the chopper stabilized DDA-INA, for the clock P1 “High” and clock P2 “Low”.	50
2.14 The schematics of the chopper stabilized DDA-INA, for clock P1 “LOW” and clock P2 “High”.	51
2.15 Selective feedback arrangement used for gain selection.	52
2.16 An example of non-overlapping clock signals.	53
2.17 The non-overlapping clock generator.	54
2.18 Noise response for EEG and ECG mode without chopper stabilization	54
2.19 Post-layout noise response for EEG and ECG mode	55
2.21 Layout of the DDA-based INA	57
2.22 Fully-differential capacitive feedback chopper stabilized INA.	65
2.23 Circuit implementation of the folded-cascode OTA.	67
2.24 Transconductance efficiency for different operating regions of a typical TSMC n-channel MOSFET of length = 3 $\mu\text{m}$ .	68
2.25 (A) The circuit schematic for source admittance. (B) The circuit schematic for drain admittance.	69
2.26 The circuit schematic of the OTA with the current-scaling technique.	71
2.27 The circuit schematic of the OTA with current-scaling technique.	72
2.28 Switch-capacitor based CMFB	74
2.30 Open-loop dc-gain and phase-response of the folded-cascode OTA.	76
2.31 CMRR response simulation of the OTA with input pair length mismatches.	76
2.32 PSRR response simulation of the OTA with input pair length mismatches.	77
2.33 Loop Stability response for the capacitive feedback OTA.	77
2.34 Noise simulation response without chopper showing the spot noise @ 10Hz	78
2.35 Noise simulation response (log) without chopper showing the $1/f$ noise corner @ 1 kHz.	79
2.36 Noise simulation response with chopper showing the transposition of the flicker noise pole to 1 kHz.	79

2.37 Frequency response simulation with chopper .....	80
2.38 Layout of the fully differential capacitive feedback chopper stabilized INA in TSMC CMOS 0.18 $\mu\text{m}$ process.....	81
3.1 Measurement setup for chopper-stabilized INA transient and frequency response characterization. ....	85
3.2 Measurement setup for the chopper-stabilized INA noise characterization .....	85
3.3 Measured transient response for our chopper-stabilized INA before (lower) and after (top) the low-pass filter. ....	86
3.4 Measurement result for noise response of our chopper stabilized amplifier .....	87
3.5 SPICE simulation result for noise response of our chopper stabilized INA .....	87
3.6 Measurement result for noise response without chopper stabilization. ....	88
3.7 SPICE simulation result for noise response without chopper stabilization .....	88
3.8 Measured frequency response with our chopper amplifier for the ECG mode.....	89
3.9 Measurement setup for our chopper-stabilized INA transient response.....	90
3.10 Single-ended transient response of the fully-differential folded- cascode based INA.....	91
3.11 FFT response of the output for 125 Hz input signal of the fully- differential chopper INA.....	91
3.12 Current measurement setup using a Keithley Pico-ammeter .....	92
3.13 Dipole moment vector showing heart's electrical nature.....	93
3.14 Estimation of cardiac vector using lead vectors.....	94
3.15 Einthoven's triangle for ECG .....	95
3.16 Fully differential PCB-based AFE.....	96
3.17 Frequency response of the fully differential PCB-based AFE circuits.....	96
3.18 Measured transient response of the fully differential PCB-based AFE circuits using inputs from a Simulaid <sup>TM</sup> ECG simulator.....	97

3.19 Simulaid <sup>TM</sup> NSR ECG waveform recorded using the fully differential PCB-based AFE circuits.....	98
3.20 Simulaid <sup>TM</sup> NSR ECG overlaid with Physionet data. ....	98
3.21 Human subject ECG recorded using the fully differential PCB-based AFE circuits .....	99
3.22 A human subject ECG waveform recording using our PCB-based AFE circuits overlaid with a Physionet ECG data (the same one shown in Fig. 3.19).....	99
4.1 Fourth generation NCVS sensor hardware. ....	102
4.2 The CMOS inverter based 10.24 MHz reference oscillator.....	102
4.3 Measured phase noise of the synthesizer used in our fourth generation NCVS sensor hardware. ....	103
4.4 Typical radiation pattern of an antenna.....	107
4.5 (A) Measured radiation patterns of the custom built helical antenna. (B) The custom built helical antenna .....	108
4.6 (A) Measured radiation patterns of the Log-periodic antenna. (B) The Log-periodic antenna. ....	109
4.7 (A) Measured radiation patterns of the patch antenna. (B) The patch antenna. ....	110
4.8 (A) Measured radiation patterns of the Yagi antenna. (B) The Yagi antenna. ....	111
4.9 (A) Diagrammatic representation of the NCVS sensor measurement set up; (B) The test setup in the anechoic chamber at Dr. Lie's lab.....	113
4.10 The flow chart for the LabVIEW <sup>TM</sup> code used in antenna evaluation using NCVS system at Dr. Lie's lab. ....	115
4.11 Box-Whisker plots for different antennas for <i>front</i> readings only.....	117
4.12 Time based arctangent demodulated signal for heart rate extraction (front readings).....	118
4.13 Box-Whisker plots for different antennas for <i>front</i> readings only with equalized gains.....	119

## **CHAPTER 1**

### **INTRODUCTION**

Vital signs are the physiological indicators which aid doctors, surgeons and health-care professionals to analyze the current medical conditions of the patient. Vital signs monitoring makes it possible for the necessary medical intervention can be performed as required. Conventional vital signs include the body temperature, heart rate, blood pressure and respiratory rate. Continuous monitoring of physiological vital signs is of paramount importance for patients in the Intensive Care Unit (ICU) and Emergency Room (ER). It is also important for medical diagnosis, as well as for wireless-assisted living.

The accurate and robust detection of a person's heart rate is desirable in both his/her normal healthy conditions as well as the conditions where uninterrupted medical observation is required. With the number of individuals succumbing to cardiac disorders, heart rate monitoring and related diagnosis have become more important than ever before. Heart rates are traditionally monitored using the electrical bio-potentials emanating from the heart, which can be tapped either externally at the body-skin surface through transducers, or internally using electrical leads planted inside the ventricular/atrial chamber of the heart. The bio-potential obtained from the body-skin surface is popularly known as Electrocardiogram (ECG) or Elektrokardiogram (EKG). Similarly the cardiac bio-potential recorded from the ventricular chamber is known as Intracardiac Electrogram or simply Electrogram (EGM). Microwave and Doppler-based techniques have also been explored to estimate heart-rate utilizing the physiological chest-wall displacement corresponding to the periodic cardiac systole-diastole. The concept of *Non-Contact Vital Signs (NCVS) Monitoring* using a radio-frequency (RF) Doppler sensor has existed for decades [1].

A normal ECG signal with its components is shown in Fig. 1.1 [2]. A typical ECG signal is a surface biopotential from a combination of atrial and ventricular

depolarization and repolarization, which translate into electrical events. The atrial depolarization is named as the P-wave, and it signifies the initiation of a cardiac cycle. The QRS complex represents the ventricular depolarization whereas the T-wave represents the ventricular repolarization. The atrial repolarization is overwhelmed by the QRS complex, hence is not noticeable [3].

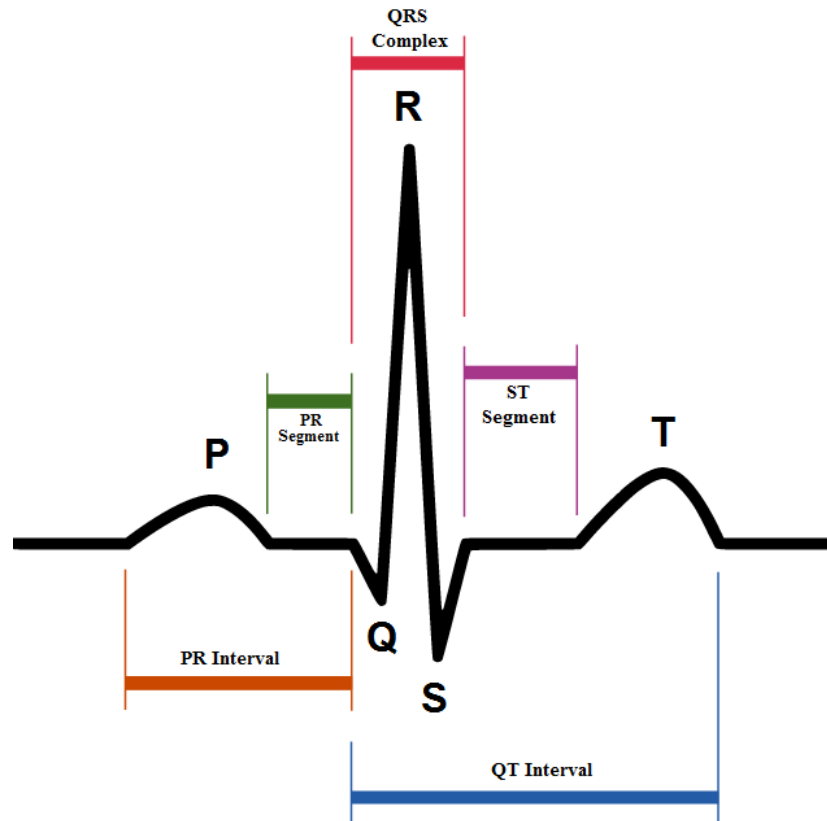


Fig. 1.1 Representation of a normal ECG signal [2]

The intracardiac signals (EGM) can be obtained using bipolar leads placed in the tricuspid valve annulus which lies in the apex region of the right ventricle [3]. Similar to ECG, the EGM is also composed of ventricular events and atrial events. The ventricular events are also termed as “near field” effects whereas the atrial events are known as the “far field” effects. The various components of the EGM signal are also named according to the convention used to describe the components of the ECG waveform. Typically, the analog front end of a wearable ECG sensor or an

implantable pacemaker/defibrillator would monitor the cardiac rhythm by recording the periodicity of the ventricular depolarization signal, the R-wave (or the QRS complex) as it is easier to detect these peaks more reliably.

Different types of cardiac bio-sensors have evolved over the past few decades depending upon the type of cardiac signals used to estimate the heart-rate. Wearable cardiac biosensors use ECG as the input for heart-rate detection, whereas Implantable Cardioverter Defibrillator (ICD) uses EGM to monitor heart-rate as well as to provide necessary defibrillation to maintain proper heart rhythm. However, a Doppler-based non-contact vital signs sensor monitors the physiologically modulated cardio-pulmonary movement signal to detect the heart rate, the more detailed physics of which will be discussed in the later part of this thesis.

## **1.1 Wearable ECG Sensors**

Wearable ECG sensors are non-invasive cardiac sensors which use the surface biopotential to record, estimate and monitor the physiological state of the heart. Wearable ECG sensors are available in many varieties from bulky clinical instrumentation to ambulatory monitoring systems. One of the most popular wearable ECG sensors is the Holter Monitor, where a patient would wear this 5/7 leads wired sensor at the belt to record his/her ECG for 24-72 hours continuously and then return to the physicians afterwards for diagnosis and evaluation. When combined with wireless transmission/communications capabilities, these latest wearable ECG sensors can play a very crucial and indispensable role in wireless-assisted living, acute-care centers and for telemetric medicine where the patients are under constant monitoring and any medical emergency conditions can be addressed immediately [5], [6], [7].

### **1.1.1 Electrodes – Wet, Dry and Capacitive Coupled**

A typical wearable ECG sensor most importantly includes an interface between the skin and the electrical circuitry to tap the cardiac surface biopotentials. Biopotential electrodes in conjunction with special dedicated gels are used for this

crucial interface. The electrolytic gels are used to create a conductive layer between the skin and the electrode. Two kinds of electrodes are available, the polarizable electrodes and the non-polarizable electrodes. Polarizable electrodes do not allow the passage of charge across the electrode-electrolyte interface on the application of current and exhibit capacitive effects, making them susceptible to undesirable motion artifacts. Non-polarizable electrodes allow a convenient flow of current across the electrode-electrolyte interface and are less susceptible to motion artifact pickups, thus making them suitable for surface biopotential sensing [3]. Usually silver/silver chloride (Ag/AgCl) electrodes are preferred as they closely resemble the non-polarizable property and are easy to manufacture [3]. The typical body skin-surface electrode and skin interface can be modeled as shown in Fig. 1.2.

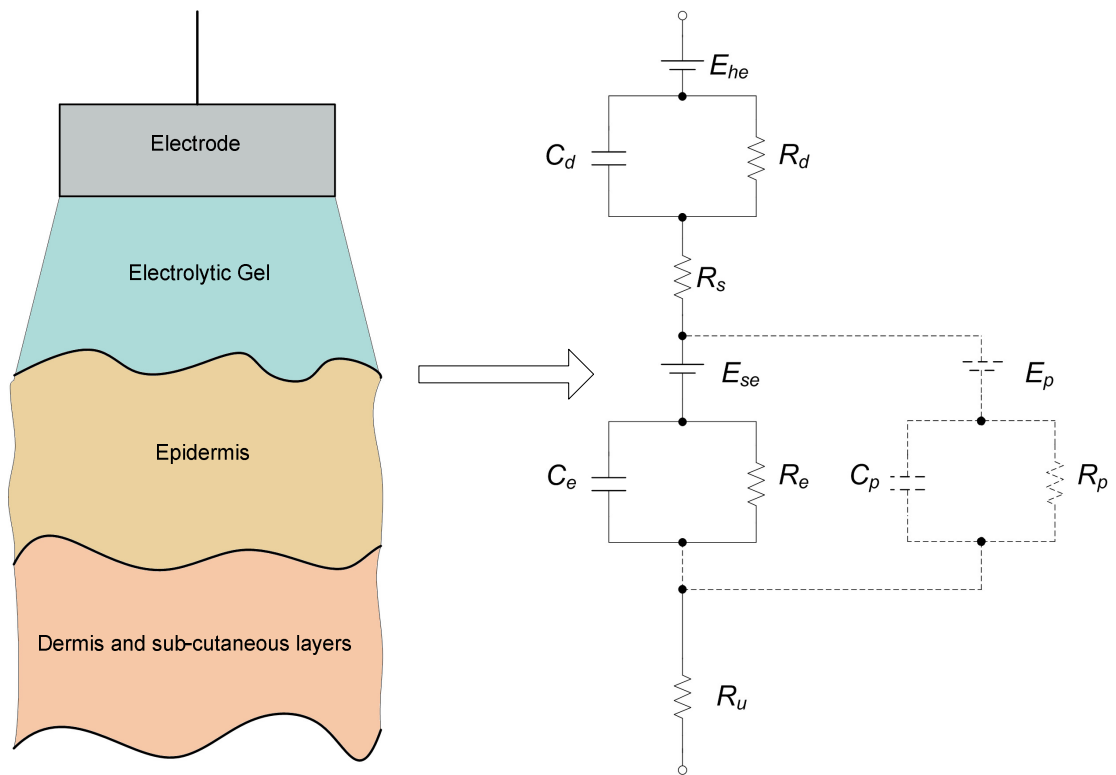


Fig. 1.2 Equivalent circuit of an electrode placed on skin.[3]

Electrolytic gels when applied on to the skin of the patient for prolonged monitoring may lead to uneasiness as well as skin inflammation due to allergic actions [8]. In order to achieve better connectivity, usually the skin is prepared by rubbing and removing the highly resistive outer layer of the skin called the *stratum corneum*. This method of causing skin abrasion will only temporarily provide better electrical connectivity because the *stratum corneum* is regenerated on a regular basis [9], thus making it ineffective for prolonged monitoring purposes. Moreover, as the wetness of the gel reduces over time the impedance observed between the skin-electrode interface increases, degrading the biopotential ECG signal quality. In the pursuit of making wearable ECG sensors robust, convenient, more acceptable and applicable for long-term monitoring, ‘dry’ electrodes have been proposed and used [10], [11]. An example of the single dry electrode is made up of an array of microprobes which penetrate the *stratum corneum* to connect to the more conductive layer lying underneath known as the *stratum germinativum*. This allows a higher level of conductivity and enabling an electrical connectivity better than or at least at par with that is obtained using electrolytic gel based electrode connections. The *stratum corneum* is a protective outer layer of the epidermis and is mostly made up of dead cells and therefore is highly resistive, whereas the *stratum germinativum* constitutes the living epidermis and forms a more conductive layer. Skin penetration using conical microprobes provides stable electrical conductivity without a possible irritant electrolytic gel, but it is still a contact based method where possible damage to the skin tissue is involved [9]. Recent work has reported using diamond shaped microprobes to reduce the tissue harm and also to establish more robust connection, making it a better alternative compared to the conical microprobes, as shown in Fig. 1.3 [12].

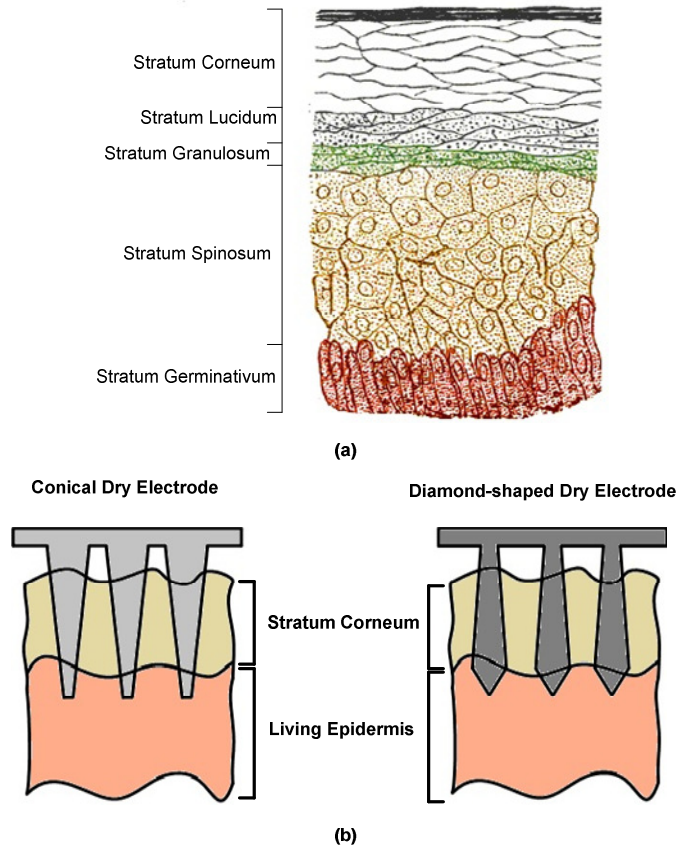


Fig. 1.3 (a) Cross-sectional view of the epidermis. (b) Depicting the use of conical and diamond-shaped dry electrodes [13], [9], [12].

We can apply the wearable ECG sensors by either using wet gel-based electrodes or dry microprobe-based electrodes, dependent upon the preferred skin contact. Any type of skin contact can be a cause of uneasiness and inconvenience in varying degree, thus hampering the utility and applicability of ECG sensors for long duration out-of-hospital monitoring. A non-contact based ECG sensor completely gets rid of the inconvenience involved in contact-based ECG sensors thus making it more appealing. Capacitive-coupling based non-contact wearable ECG sensors have been recently explored and reported [14]. As shown in [14], the capacitive-coupling used in the non-contact ECG sensor is achieved using the combination of a metal electrode and the human skin with a layer of insulator-type material in between. An efficient and effective signal coupling requires a higher value of the capacitance formed between

the human body and the metal electrode. To obtain higher value of capacitance, either the area of the metal electrode can be increased, the insulator layer used can be chosen to have a high dielectric constant, or the thickness of insulator layer can be reduced as much as possible [14], [15]. Works using various dedicated dielectric material and with varying sizes of electrodes have been reported. In order to make the wearable sensor more user-friendly, typically-worn normal clothing was considered as the insulator layer [14]. However, capacitive-coupling based non-contact wearable ECG sensors suffer from degraded ECG signal quality due to much higher impedance presented by the capacitive electrodes. Furthermore, since the capacitive electrodes are fixed on the clothing they are susceptible to motion artifacts which results in variations in the capacitance of the electrodes, this leads to unwanted variations in the ECG biopotential. The aging of the textile fabrics and the body movements are just some of the thorny problems that need to be resolved for practical implementation of these noncontact C-V based ECG sensors.

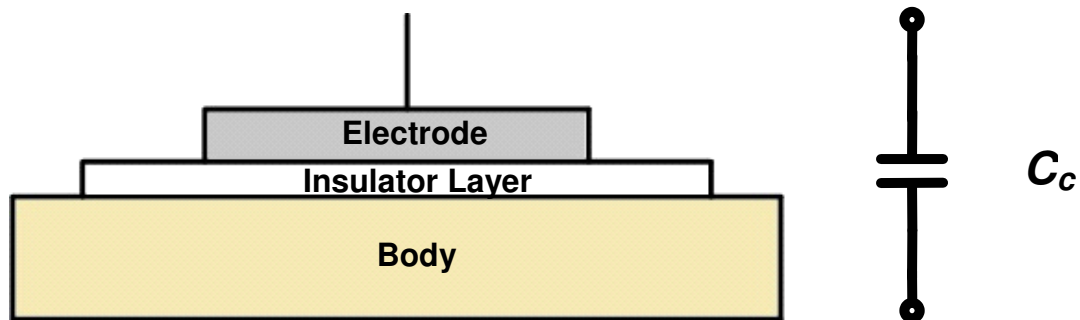


Fig. 1.4 Electrode body interface with equivalent electrical circuit [14]

### 1.1.2 Components of the wearable ECG sensor system

For a typical wearable ECG sensor, the biopotential electrode is placed next to the Analog Front End (AFE) circuitry. The electrode acts as a transducer between the ionic transport of the nerves on the skin and the electronic transport of the conductive material. This transducer action makes the analog biopotential electrical ECG signals

available (converting from the ionic currents generated by heart movements) for the AFE IC to sense. The surface ECG signals collectible from the electrodes are normally weak, having amplitudes in the range of 0.5mV to 4mV and containing meaningful information in the frequency range of 0.01Hz to 250Hz [3]. Furthermore, this analog signal has to be made available for digital signal processing in order to show and extract the ECG signal information in a desirable manner. Thus, the AFE circuitry is required to amplify, filter and subsequently digitize the cardiac biopotential signal. Many research groups naturally consider amplification and filtering as the only required functionalities of an AFE circuitry (just like us), and treat digitization of the signal as a separate unit under the analog-to-digital converter (ADC) block [16]

A typical wearable ECG sensor system consists of the following distinct components, as shown in Fig. 1.5 [12], [16]:

- (1) Biopotential Electrode placed at defined points on the human body.
- (2) Analog Front End (AFE) Circuitry.
- (3) A microprocessor Unit.
- (4) Wireless connectivity.
- (5) Software designed to monitor and record the physiological data.

In the recent decades the bio-medical community has strived for miniaturization and ease of use for the entire ECG recording system to enhance its various applications. Studies on different types of electrodes, high-performance circuit topologies and efficient systems implementation, including incorporating wireless connectivity between the ECG sensor and the monitoring computer, have all been reported [5], [6], [7], [8], [9], [10], [11], [12], [13], [14]. A key enabler for realizing an efficient, conveniently sized and accurate wearable ECG sensor lies in the AFE circuitry design. To increase the applicability of ECG sensors and to achieve miniature sizes, the power consumption has to be made as small as possible, thus permitting the system to be powered using tiny batteries. Amongst the components of an ECG sensor

system, the AFE circuitry plays a pivotal role in deciding the overall power-consumption as it has to be ALWAYS on for continuous monitoring. A low-power high performance monolithic AFE integrated circuits (IC), when integrated with the ADC, RF transceivers and microprocessor with memories, can become a completely integrated System-on-Chip (SoC) to help realizing portability, signal integrity, small form factor, and low-power wireless connectivity.

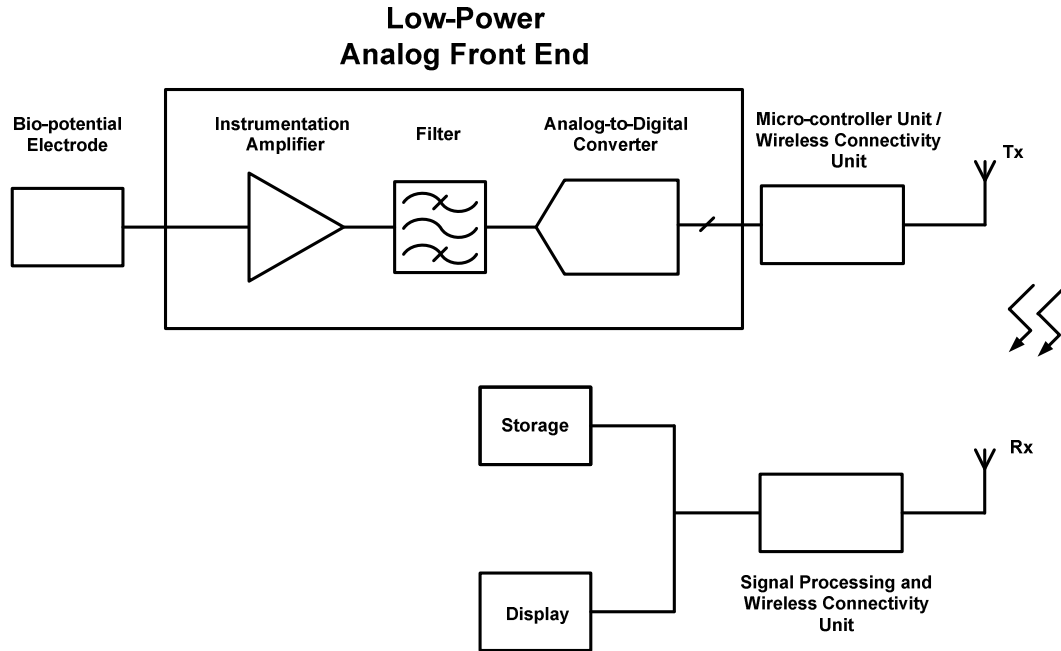


Fig. 1.5 A typical wearable ECG sensor system [12]

## 1.2 Implantable Cardioverter Defibrillator (ICD)

Monitoring of the key cardiac parameters is very important, and if the information obtained from such a monitoring system can be used to provide immediate therapeutic treatment then it can act as a basic life-saving system. For example, cardiac arrhythmia, which is caused either due to pathological or physiological abnormalities, has been reported to be a prime cause of sudden cardiac death (SCD) [4]. Arrhythmia involves irregular cardiac patterns which lead to cardiac fibrillation, a condition where the cardiac output can be diminishing to close to zero, leading to an asystolic state followed by irreparable brain damage and ultimately death

[3]. Cardiac fibrillation, especially ventricular fibrillation, is the most lethal one and in the absence of immediate resuscitation, can lead to an instant death. Studies have shown that the chances of survival are strongly dependent on the time delay before which defibrillation was administered [4]. In such a scenario availability of an immediate defibrillation subsequent to successful monitoring and detection of a lethal arrhythmia can save numerous lives.

Conceptually, if a reliable and ultralow-power ECG sensor is implanted inside a patient's body, it would be able to sense arrhythmia and perform defibrillation whenever needed. Therefore, implantable cardioverter defibrillator (ICD) was first conceived by M. Mirowski in the late-1960s and then seconded by J. C. Schuder in the 1970s [17], [18]. Subsequent research and developments led to the first ICD to be implanted in a human body in February 1980. The first ICD to be approved by the Food and Drug Administration (FDA) in 1985 for general usage was the 1400 series from Cardiac Pacemakers Inc. [4]. The first generation of ICDs included non-programmable hardware and was built using application specific integrated circuits (ASICs). The second generation of ICDs was equipped with programming capabilities, allowing the physicians to program the therapy rate thresholds without any surgical operations. Further advancements were aimed at combining the defibrillator with the pacemaker functionality to administer immediate therapy in case of various cardiac irregularities. Additional improvements include signal processing to classify cardiac rhythm and also to record the cardiac data of the patient. These advancements are classified under third generation systems. Modern ICDs are equipped to provide both, the high-voltage pulses of about 800V to achieve defibrillation when ventricular fibrillation is detected, and mild electrical pulses of 6-8V as a part of the pacemaker functionality to stabilize the heart rate [19]. Wireless connectivity is also being harnessed for enabling medical telemetry and continuous monitoring of the patients critical cardiac condition [20]. A typical modern dual-chamber ICD with the intra-cardiac transvenous leads inside a human heart is shown in Fig. 1.6.

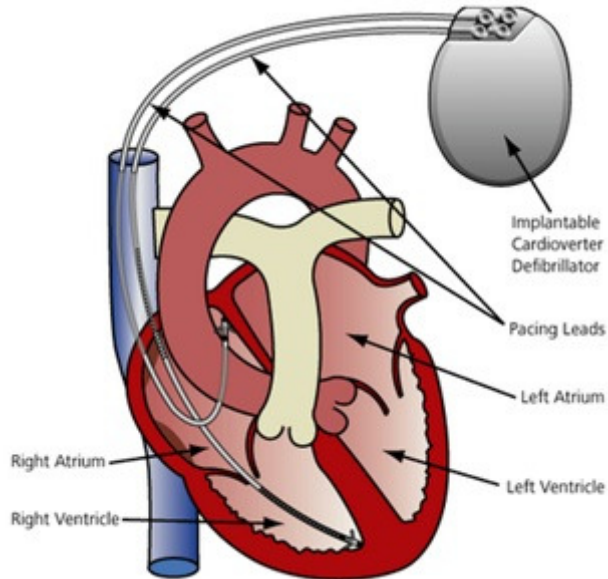


Fig. 1.6 An Implantable Cardioverter Defibrillator (ICD) inside a human heart [20]

### 1.2.1 Defibrillation

Defibrillation is usually provided using an electric shock to revive the normal cardiac rhythm [3]. If not using an ICD, the electric shock can be provided using electrodes either placed immediately on the myocardium or placed trans-thoracically. It requires lesser current to provide the required electrical energy when using electrodes placed on the myocardium, but it requires a surgical operation of the heart. Arrhythmias may exhibit bradycardia, a condition where the heart rate is way below the normal sinus rhythm; or tachycardia, a condition of faster heart rate that may eventually result in cardiac fibrillation. An ICD can be designed in such a way that it can also act as a pacemaker for a bradycardia to rectify the heart rate, while also perform defibrillation for serious tachycardia.

When the electrical energy required for defibrillation is applied during the T-wave (ventricular repolarization), it results in reinforcement of the ventricular fibrillation thus increasing the risk of SCD. To circumvent these problems, it is required that the defibrillation is synchronized to the R-wave and is administered

much ahead of the T-wave. Defibrillator systems which are designed so are known as cardioverters [3].

The importance of ICDs can be understood by the fact that the prompt therapy delivered by the ICDs has remarkably increased the survival chances of SCD-prone patients. During the days when ICDs were not in use it was understood in the medical community that 30 % patients who were resuscitated following a SCD event would eventually die within a year. But the mortality rate of a similar group of patients who were administered immediate therapy using ICDs was just 2%, proving the life-saving effectiveness of the ICDs [4].

ICDs are implanted inside a human body and are expected to last at least for the duration of 5 to 7 years [4]. The defibrillation and pacemaker functionalities are invoked whenever exigencies like sudden cardiac arrest or heart block arise but the monitoring system is needed to be continually active for the entire duration of the event. Similar to the wearable ECG sensors the monitoring/sensing system comprises of the combination of electrodes and analog front end circuits. The sensing system is used to detect either bradycardia or ventricular tachycardia, and accordingly either pacemaker or defibrillator is invoked. Defibrillation is successfully administered by providing electrical pulses of around 800V for a period of 4-8ms [4], implying that energy capacity of 35-40 J is required to be delivered by the in-built high-voltage generator each time. A modern ICD typically is made up of dedicated intra-cardiac electrodes, AFE circuitry with ADCs, a high-voltage generator, a microprocessor, memories, power-management circuits and additional circuitry enabling wireless connectivity [19]. A successful ICD implementation is guaranteed if low-power operation and optimal miniaturization is achieved, which is possible by using integrated circuits based SoCs design.

### **1.2.2 Electrodes and Lead-assembly**

As with the wearable ECG sensors, the electrodes in an ICD system again play a pivotal role in determining quality and accuracy of intra-cardiac biopotential signal (EGM) acquisition. Additionally, the leads connecting the ICD device to the electrodes placed in the heart are also a critical part of the entire ICD system. The modern ICD systems use dual-chamber transvenous endocardial leads placed in both the right atrium and the right ventricle. These leads are capable of supporting sensing, pacing as well as defibrillation of the cardiac rhythms. The transvenous endocardial ICD leads are expected to be good electrical conductors, and they also must possess mechanical durability. The leads are exposed to constant and periodic stress due the cardiac contractions, which can result in torsional bending and compression forces being applied on them for almost 37 million times per year [22]. The leads are designed to endure high voltage levels as well as additional thoracic stresses due to the arm and chest movements of the patient. The transvenous leads are also required to have excellent insulation in order to ensure accurate sensing of the intra-cardiac EGM, and the application of electrical pulses whenever required. The leads also have to endure the oxidative stress in chemically hostile environment of the heart [3], [22]. Similarly, the ICD electrodes also need to be able to tolerate the mechanical stress due to cardiac activity and must be able to maintain their positions such that they can support the administering of the electrical pulses when required. The electrodes are required not to react and corrode, as otherwise undesirable irritation to the heart tissues may be experienced, making the implantation medically inappropriate. Additionally, interactions/reactions of the electrodes with the heart tissues are unwanted, as it may lead to an increase in the stimulation threshold.

The intra-cardiac electrodes are of the following three types [3];

- (1) Epicardial electrodes, which are placed on the external surface of the heart;
- (2) Endocardial electrodes, which are fixed on the inside wall of the heart;
- (3) Intramyocardial electrodes, which are buried within the heart walls

The transvenous leads are constructed in the form of helical coils of spring-wire alloy molded in a silicone-rubber or polyurethane cylinder [3], [22]. The helical construction reduces the effective stress, and thus increasing durability. The silicone enclosure aids in structural flexibility and provides electrical insulation and biological compatibility [3], [22]. The ICD electrodes are typically made up of the same material as the ICD leads. The ICD electrodes and leads are desired to have low-resistance so as to reduce the voltage drops and heat generation during the high-voltage applications [4], [22]. Many materials as well as combination of materials such as platinum, carbon, titanium and stainless steel have been used. Special alloys like Elgiloy (an alloy of cobalt, chromium, iron, nickel, molybdenum, manganese, carbon and beryllium), and MP35N<sup>®</sup> (an alloy of cobalt, chromium, molybdenum and iron) have been used [3]. MP35N<sup>®</sup>, developed by SPS Technologies, Cleveland, OH has been preferred due its low susceptibility to corrosion and mechanical fatigue. But for high-voltage application often a combination of MP35N<sup>®</sup> and silver is employed to manufacture the electrodes and helical coils of transvenous leads [22].

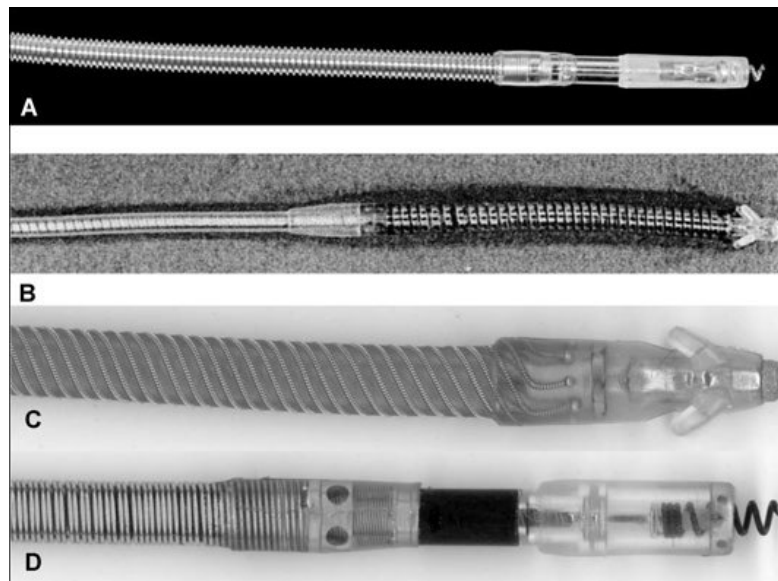


Fig. 1.7 Intra-cardiac transvenous leads: (A) Medtronic Transvene, (B) CPI Endotak, (C) Ventrax TVL/SPL and (D) St. Jude Medical TVL-ADX 1559 [22]

One of the most important reasons for the malfunction or failure of the ICD system is the ICD lead failure [22]. Additionally, the need for vascular surgery for ICD implantation also impeded its wide-spread applications. With the advent of the revolutionizing technology of Subcutaneous-ICD systems (S-ICD<sup>®</sup>, developed by Cameron Health Inc, later acquired by Boston-Scientific Corporation in 2012), the risks and failures related to vascular surgery and prolonged usage of intra-cardiac transvenous leads can be completely diminished. S-ICD<sup>®</sup> systems use tunneled subcutaneous lead-electrode assembly, placed approximately 1 cm left of the sternum instead of the intra-cardiac transvenous leads, and are implanted in small pouch formed under the skin near the sixth rib [23], [24]. The S-ICD<sup>®</sup> systems have obtained FDA approval and are under clinical trials. Preliminary trial results indicate their therapeutic efficiency in tackling ventricular fibrillation, but also reflect inadequacies with respect to ventricular tachycardia due to lack of anti-tachycardia pacing [24]. Furthermore the S-ICD<sup>®</sup> systems are reported to require higher energy levels to administer the cardiac therapy in comparison with the traditional intracardiac transvenous ICD [24], [25]. Additional trials with higher volume of subjects in the age-groups prone to cardiac dysfunction are required to understand and characterize the S-ICD<sup>®</sup> systems more [24].

### **1.2.3 Components of the ICD system**

Along the same lines of the wearable ECG sensor, the transvenous ICD lead-electrode assembly is followed by the AFE circuitry of the ICD system. The ICD system is a more complex system, of which the AFE circuitry helps to form the EGM signal sensing component. As mentioned before the intra-cardiac EGM signal is composed of ‘near-field’ electrical events of ventricular depolarization and repolarization, as well as the ‘far field’ electrical events of atrial depolarization and repolarization. The intra-cardiac EGM signal spectrum can be classified using the similar nomenclature as used for surface ECG signals below [19], [21]:

- (1) Intra-cardiac ventricular QRS-complex signal, which signifies the ‘near field’ ventricular depolarization, and occupies the frequency range from 20Hz to 60Hz;
- (2) Intra-cardiac P-wave signal, which signifies the ‘far field’ atrial depolarization and occupies the frequency range from 40 Hz to 100 Hz;
- (3) The intra-cardiac T-wave signal, which signifies the ‘near field’ ventricular repolarization and occupies the frequency band below 10 Hz;
- (4) The frequency band from 100 Hz to 2 kHz is occupied by muscle myopotentials, such as diaphragmatic myopotentials.

In comparison with the ECG signals, intra-cardiac EGM signals have stronger amplitudes in the range of 0.1 mV to 20 mV [4]. Furthermore, this analog signal has to be made available for digital signal processing in order to decide the kind of therapeutic measure needed, as well as to show the signal information in a desirable manner. Therefore, the AFE circuitry is required to amplify, filter and digitize the intra-cardiac EGM signals. The AFE filter is designed to effectively filter out and attenuate the low-frequency T-wave signals to rule out the possibility of a false detection. Additionally, the high frequency muscular artifacts also need to be rejected. A typical ICD/pacemaker system consists of the following distinct components, [20] as shown in Fig. 1.8:

- (1) Intra-cardiac electrode and transvenous lead assembly.
- (2) Analog Front End Circuits.
- (3) Bio-Signal Processing Block.
- (4) System Controller to control the pacing and defibrillation modules.
- (5) Wireless connectivity.

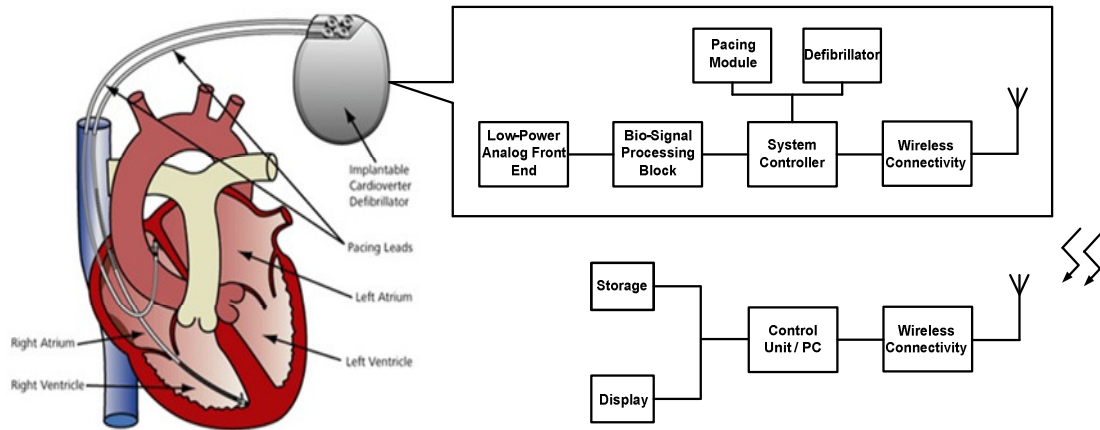


Fig. 1.8 A typical modern ICD/pacemaker system [20]

The wireless connectivity for a modern ICD/pacemaker system depicted in Fig.1.8 is achieved using ‘Zigbee’, which is defined by IEEE 802.15.4 protocol [20]. Zigbee enables data transmission of 40kbps utilizing a sub-1GHz frequency band, making it suitable for low-power implantable implementations like ICD/pacemakers.

Continuous efforts towards the miniaturization and precision enhancement of the ICD recording system are being done. Studies on different types of electrodes, lead wire assemblies, high-performance circuit topologies, efficient algorithms for diagnosis and efficient system implementations, such as incorporating wireless connectivity between the ICD system and the monitoring computer, have been reported [20]. Since each implantation of the ICD involves surgery, one of the most important factors for an ICD system is the operational longevity, which is dependent on the current consumption of the dedicated electronic circuitry as well as the battery capacity (say Li-ion battery) used to power the ICD/pacemaker. The lower the current consumption, the higher is the longevity, and typically for a 5-year ICD device lifetime the sensing component which includes the AFE circuits must have a current consumption of less than  $5\mu\text{A}$  [4]. A low-power high performance completely integrated AFE System-on-Chip (SoC) helps in both longevity and accuracy with digital processing capabilities.

### **1.3 Doppler-Based Non-Contact Vital Signs (NCVS) Sensor**

It has been seen that using wearable ECG sensors can cause discomforts to the patient involved, and the sensors have to be designed with the strict power consumption and miniature form factor requirements to make them applicable for ambulatory monitoring. In this context, non-contact vital signs sensing is very attractive, especially the heart-rate and respiration rate detection based on Doppler radar operating at microwave frequencies that has been reported since 1970s [25], [27]. The Doppler-based non-contact vital signs (NCVS) sensor can be used for physiological monitoring of patients with different types of respiration or cardiac complaints without the need of any contact or invasive implantation. The NCVS sensor uses the external periodic cardio-pulmonary movements as the information source to detect the respiration rate and heart rate. The NCVS system can also act as a ‘life-detection’ system when looking for survivors underneath debris and rubbles [28]. In cases of patients with burn injuries NCVS sensor can be employed for the heart-rate monitoring instead of using wearable ECG sensors, which are likely to cause discomforts and pains for the patients. A robust and advanced NCVS sensor installed on a patient’s bed or mounted on the ceiling in hospitals, nursing homes or residential houses can be used for long-term monitoring even without the need for the patient’s direct involvement. Since NCVS sensors can be placed at some distance away from the patients, they do not cause discomforts or irritations due to movement restrictions that is typically associated with wearable ECG sensors. As discussed earlier, battery consumption and a small form factor are very important considerations for the long-term wearable ECG or ICD-based monitoring systems. However, since NCVS sensors are usually placed externally at a distance from the patient, they can be powered by mains power from the wall sockets or by replaceable batteries, thus making them an attractive alternative for long-term monitoring of heart rate and respiration rate. NCVS sensors can be designed for Industrial, Scientific and Medical (ISM) microwave frequencies, such as 2.4 GHz [29], [30], [31] and 5.8GHz to make them universally acceptable for monitoring.

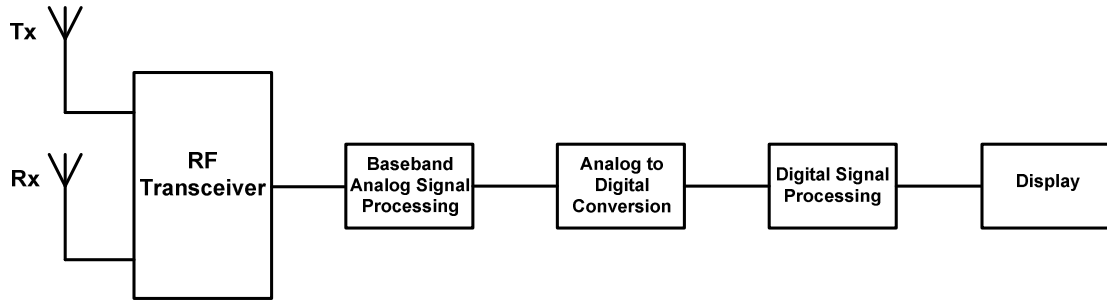


Fig. 1.9 A typical Doppler-radar based NCVS sensor [30]

According to the Doppler effect, a target with a time-varying position and a zero-velocity reflects the illuminating signal with its phase modulated proportional to the time-varying target position [29], [33]. The NCVS sensor applies the Doppler radar theory by illuminating a stationary patient's chest wall having periodic movements with the continuous wave (CW) incident wave. The RF transceiver block of the NCVS sensor can act as the CW radar to transmit the signal at an ISM frequency with 0 dBm power, and the phase modulated signal from the physiological movements is reflected from the patient's chest wall, which is then received by the RF transceiver block as well. The reflected signal contains the periodic cardio-pulmonary movement data, and demodulating the phase of this signal and extracting the time-varying cardio-pulmonary information can provide good estimates of the heart-rate as well as the respiration rate.

### 1.3.1 Doppler-radar principle for NCVS sensor

The classic Doppler-effect or the Doppler-shift in frequency is given as,

$$f_d(t) = \frac{2f}{c} v(t) = 2 \frac{v(t)}{\lambda} \quad (1.1)$$

Here  $v(t)$  is the velocity of the target,  $f$  is the transmitted frequency,  $c$  is the velocity of propagation and  $\lambda$  is the wavelength of the transmitted signal. Considering the case

when the target has a zero net velocity with a periodic cardio-pulmonary movement  $x(t)$ , the Doppler effect can now be represented as a phase modulation given by [34]:

$$\theta(t) = \frac{2f}{c} (2\pi x(t)) = \frac{4\pi x(t)}{\lambda} \quad (1.2)$$

The signal transmitted from the CW radar is represented as,

$$T(t) = A_T \cos(2\pi ft + \phi(t)) \quad (1.3)$$

Here  $A_T$  is the amplitude of the CW transmitted signal,  $\phi(t)$  is the phase-noise introduced by the oscillator of the transceiver block. Considering the distance between the target and the NCVS sensor to be  $d_0$  and the periodic cardiopulmonary movement to be  $x(t)$ , the time-varying total distance between the target and the sensor can be expressed as  $d(t) = d_0 + x(t)$ .

The time delay can be obtained by dividing the time-varying total distance by the signal propagation velocity,  $v(t)$ . Considering the periodic movement of the chest wall, the total distance between the sensor and the chest is expressed as:

$$d(t) = d\left(t - \frac{d(t)}{c}\right) \quad (1.4)$$

The total time-delay seen by the signal for a round-trip path (i.e., sensor  $\rightarrow$  chest wall  $\rightarrow$  sensor), is given as ,

$$t_d = \frac{2d\left(t - \frac{d(t)}{c}\right)}{c} = \frac{2(d_0 + x\left(t - \frac{d(t)}{c}\right))}{c} \quad (1.5)$$

The signal received at the sensor's receiver is a time-delayed phase-modulated version of the transmitted signal and can be expressed by using equation (1.3) as,

$$R(t) = A_R \cos(2\pi f(t - t_d) + \phi(t - t_d) + \theta_0) \quad (1.6)$$

Here  $\theta_0$  is the phase delay due to the physical distance between the NCVS sensor and the subject. This quantity is a constant for a given setup. Substituting,  $t_d$  in equation (1.6), we get

$$R(t) = A_R \cos \left[ 2\pi ft - \frac{4\pi d_0}{\lambda} - \frac{4\pi x \left( t - \frac{d(t)}{c} \right)}{\lambda} + \phi \left( t - \frac{2d_0}{c} - \frac{2x \left( t - \frac{d(t)}{c} \right)}{c} \right) + \theta_0 \right] \quad (1.7)$$

As the time-period of cardio-pulmonary movement,  $T \gg d(t)/c$ , implying that

$x \left( t - \frac{d(t)}{c} \right) \approx x(t)$ . And considering  $\frac{2x \left( t - \frac{d(t)}{c} \right)}{c}$  in the phase-noise term to be negligible as  $d_0 \gg x(t)$ , equation (1.7) can be expressed as,

$$R(t) \approx A_R \cos \left[ 2\pi ft - \frac{4\pi d_0}{\lambda} - \frac{4\pi x(t)}{\lambda} + \phi \left( t - \frac{2d_0}{c} \right) + \theta_0 \right] \quad (1.8)$$

As mentioned earlier and expressed in equation (1.8), it is easily seen that the reflected signal with cardio-pulmonary information is simply a time-delayed and phase modulated version of the transmitted signal. Demodulation of this signal will enable estimation of the heart rate and respiration rate.

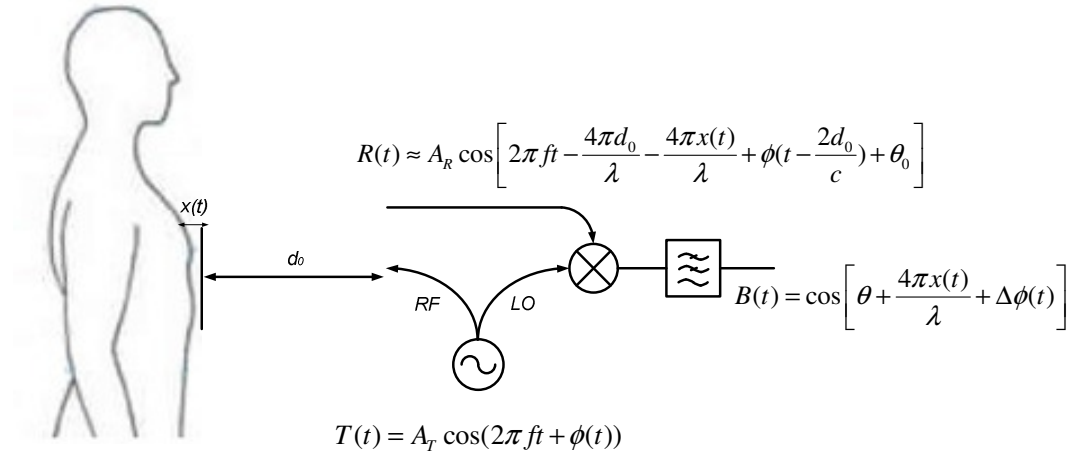


Fig. 1.10 Simplified depiction of Doppler-radar principle used for NCVS sensor [32]

The baseband signal obtained after the down-conversion mixing using the CW transmit signal shown in equation (1.1) is given as below (ignoring the amplitudes for simplicity):

$$B(t) = \cos \left[ \frac{4\pi d_0}{\lambda} + \frac{4\pi x(t)}{\lambda} + \phi(t) - \phi(t - \frac{2d_0}{c}) + \theta_0 \right] \quad (1.9)$$

On simplification, equation (1.9) can be re-written as,

$$B(t) = \cos \left[ \theta + \frac{4\pi x(t)}{\lambda} + \Delta\phi(t) \right] \quad (1.10)$$

Here  $\theta$  is phase term dependent on the position of the subject with respect to the NCVS sensor, and  $\Delta\phi(t)$  is the residual phase noise after range correlation. Considering the case when  $\theta$  is an odd multiple of  $\pi/2$ , implying

$\theta = \frac{2k+1}{2}\pi$  for  $k = 0, 1, \dots, n$ , and using small-angle approximation, equation (1.10) can

be re-written as,

$$B(t) \approx \frac{4\pi x(t)}{\lambda} + \Delta\phi(t) \quad (1.11)$$

As can be seen from equation (1.11), the baseband signal  $B(t)$  represents the phase-modulation information corresponding to the cardio-pulmonary movements. The condition when  $\theta$  is an integer multiple of  $\pi$ , implying  $\theta = k\pi$  for  $k = 0, 1, \dots, n$ . The baseband signal of this non-quadrature single-channel NCVS sensor is represented as,

$$B(t) \approx 1 - \left[ \frac{4\pi x(t)}{\lambda} + \Delta\phi(t) \right]^2 \quad (1.12)$$

It is observed that the base-band signal does *not* optimally represent the cardio-pulmonary movements anymore and hence presents a ‘null-point’. The ‘null-point’ is seen whenever the LO signal and the incoming RF signal carrying the cardio-pulmonary information are in-phase or  $180^\circ$  out-of-phase, and the optimal sensitivity condition is observed when they are quadrature to each other. As  $\theta$  is dependent on

the distance of the subject from the NCVS sensor, the ‘null-points’ are seen every quarter wavelength ( $\lambda/4$ ). For a 2.4 GHz system,  $\lambda/4$  is almost equal to 3 cm, which is a very small distance for optimal adjustments to be done to avoid the ‘null-points’. Considering the above condition, quadrature receivers have been advocated to overcome this problem of the non-quadrature Doppler-based NCVS sensors [33].

### 1.3.2 Quadrature receiver and arc-tangent demodulation for NCVS sensors

A quadrature receiver is essentially a dual channel receiver where the RF input signal is split in two signal paths (e.g., using a 2-way  $0^\circ$  balun) and each of the RF paths are then down converted using two mixers with quadrature LO inputs. The mixers’ quadrature LO signals can be obtained; for example, from the same LO signal using a 2-way  $90^\circ$  power splitter. Following equation (1.10), the two orthonormal baseband signals obtained after mixing are given as,

$$B_I(t) = \cos \left[ \theta + \frac{4\pi x(t)}{\lambda} + \Delta\phi(t) \right] \quad (1.13)$$

And

$$B_Q(t) = \sin \left[ \theta + \frac{4\pi x(t)}{\lambda} + \Delta\phi(t) \right] \quad (1.14)$$

Here  $B_I$  denotes in-phase baseband signal channel and  $B_Q$  denotes the  $90^\circ$  out-of-phase or the quadrature baseband signal channel. When  $\theta$  is an odd multiple of  $\pi/2$ ,  $B_I$  channel experiences a ‘null-point’ whereas  $B_Q$  is at its optimum point. Again when  $\theta$  is an integer multiple of  $\pi$ ,  $B_I$  channel experiences a optimum point whereas  $B_Q$  is at its ‘null-point’. Thus, the mutual orthonormality between the channels ensures that for every  $\pi/2$  phase or every  $\lambda/4$  distance a simultaneous null-point and an optimum point are observed on either of the channels. Since information on any one of the channel can be used to cardio-pulmonary rates, the quadrature receiver, theoretically, eradicates the problem of null-point.

The quadrature baseband signals undergo various stages of analog-signal processing such as amplification and filtering before being digitized for further digital signal processing and demodulation. The use of an efficient demodulation technique decides the efficacy and accuracy of heart rate and respiration rate detection using the Doppler-radar based NCVS sensor. In the recent past, various signal processing techniques have been reported such as linear demodulation, arc-tangent demodulation, linear-regression and complex-signal demodulation, each having its share of pros and cons [30], [34]. Over the years arc-tangent demodulation technique has emerged as more opted choice due to its simple implementation and reasonably robust performance [30], [31], [36]. The accuracy of the arc-tangent demodulation technique increases when adequate dc-offset compensation techniques are employed in order to discard the unwanted dc-offset and preserve the dc-information regarding the target position [37], [38]. Using equation (1.13) and (1.14) the arc-tangent demodulation can be implemented as represented in equation (1.15) below to obtain the cardio-pulmonary information,

$$\phi_{\text{arc-tangent}}(t) = \arctan \left[ \frac{B_Q(t)}{B_I(t)} \right] = \arctan \left[ \frac{\sin \left[ \theta + \frac{4\pi x(t)}{\lambda} + \Delta\phi(t) \right]}{\cos \left[ \theta + \frac{4\pi x(t)}{\lambda} + \Delta\phi(t) \right]} \right] = \left[ \theta + \frac{4\pi x(t)}{\lambda} + \Delta\phi(t) \right] \quad (1.15)$$

As discussed later, depending upon the range-correlation effect, the residual phase noise term can be considered small enough and the equation (1.15) can be represented as,

$$\phi_{\text{arc-tangent}}(t) \approx \theta + \frac{4\pi x(t)}{\lambda} \quad (1.16)$$

This time-varying phase modulated cardio-pulmonary information enables the detection of heart rate and respiration rate. The expression in equation (1.16) is an ideal scenario; however in real-world implementations, there exists imbalance between the I and Q channels and also the dc-offset. These will act as linear

transforms on the I and Q channels and following which the arc-tangent demodulation will result in:

$$\phi'_{\text{arc-tangent}}(t) = \arctan \left[ \frac{B_Q(t)}{B_I(t)} \right] = \arctan \left[ \frac{V_Q + A_e \sin \left[ \theta + \frac{4\pi x(t)}{\lambda} + \Delta\phi(t) + \phi_e \right]}{V_I + \cos \left[ \theta + \frac{4\pi x(t)}{\lambda} + \Delta\phi(t) \right]} \right] \quad (1.17)$$

Here  $A_e$  and  $\phi_e$  represent the amplitude error and phase error generated due to the channel imbalance, whereas  $V_I$  and  $V_Q$  are the dc-offsets of the system. Methods like Gram-Schmidt procedure can be used to compensate the amplitude and phase errors [30], other advanced techniques also have been reported [37]. But the inherent dc-offsets require special attentions, and several methods for dc-offset cancellation and compensation have been published, while one of the most prominent one being the center tracking method [38].

### 1.3.3 Direct-conversion receiver and range correlation in NCVS sensors

It has been established that direct-conversion quadrature receivers are well-suited for NCVS sensors [29], [30], [31]. The direct-conversion receivers or zero-IF receivers directly down-convert the RF signal to the baseband for further signal processing, and this reduces the design complexity of the zero-IF receivers when compared to heterodyne receivers. Using a lesser number of components also reduces the overall power consumption and the form factor. A crucial advantage of using direct-conversion receiver for NCVS sensors is the ‘range-correlation’ effect, which remarkably reduces the noise spectrum at baseband [29], [40]. The ‘range-correlation’ effect is applicable in designs where the transceiver uses the same source to generate the transmit signal and the local oscillator (LO) signal for the down-converting mixers. Since the physiologically phase-modulated signal reflected from the patient’s chest wall is a time-delayed version of the transmit signal, there exists a correlation between this signal and the local oscillator (LO) signal of the down-converting mixers. Upon frequency mixing, this correlation reduces the resultant phase noise at baseband. The

degree of correlation is dependent on the time delay between the transmitted RF signal and the received signal, and again this time delay is proportional to the target range (hence the name ‘range correlation’). The target range is the distance between the illuminated subject and the NCVS sensor radar. The range-correlation effect is shown conceptually in Fig. 1.11 [29]. Consequently the use of direct-conversion receiver helps in relaxing the phase-noise requirement of the voltage-controlled oscillator (VCO) used as the signal source for both the transmit signal and the LO signal. The signal of interest at baseband has the relevant cardio-pulmonary data in the signal range of 0.1 Hz – 10Hz where the effect of high phase-noise is detrimental, and this range-correlation effect helps circumventing the VCO phase-noise effect, thus increasing the detection accuracy and robustness.

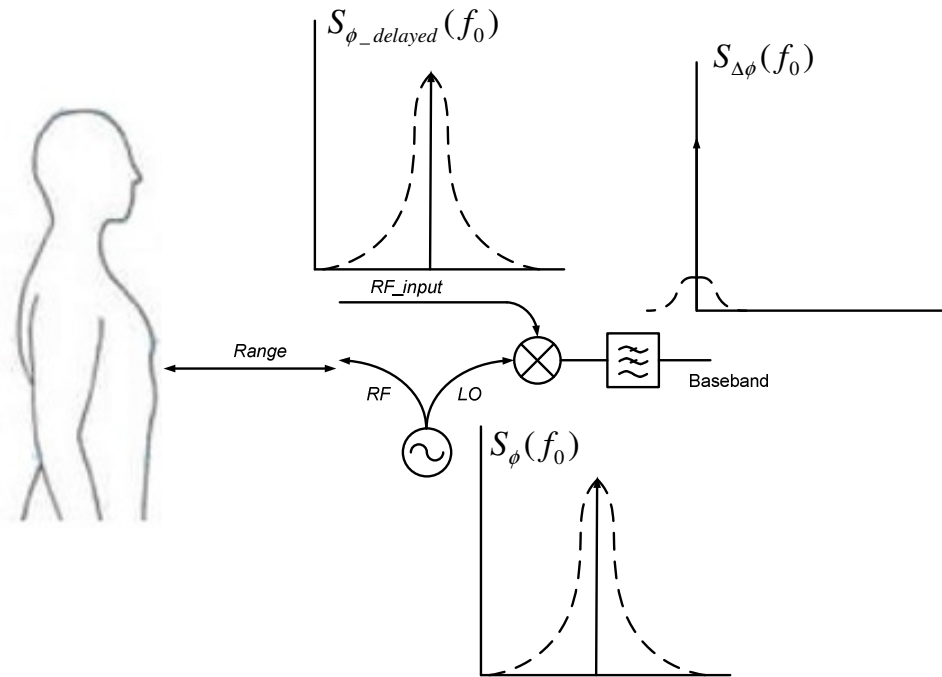


Fig. 1.11 Range-correlation in a direct-conversion Doppler-based NCVS sensor [29]

Here  $S_{\phi}(f_0)$  is the phase noise of the signal source used as the LO and the transmit RF signal,  $S_{\phi\_delayed}(f_0)$  is the phase noise of the physiological modulated

reflected RF signal and  $S_{\Delta\phi}(f_0)$  is the residual phase noise seen at baseband after phase noise filter due to the range-correlation effect. The direct-conversion receivers also have their share of disadvantages, where the most important one being the inherent problem of dc-offsets. This dc-offset is a result of using the same frequency for the mixer LO as the input RF signal. LO self-mixing caused by the LO feedthrough also contributes to the dc-offset problem. The inherent dc-offset of the direct-conversion receiver combined with the dc-offset due to background clutters and the non-cardiopulmonary signals reflected from rest of the body of the subject can add up to a noticeably large dc-offset, which needs to be filtered or compensated to avoid saturation of the subsequent baseband circuitry. Since the cardio-pulmonary signals are at very low frequencies (close to dc), the issue of dc-offset poses a challenge in accurate detection of the heart rate and respiration rate.

### **1.3.4 Generations of NCVS sensor at Dr. Lie's Group in Texas Tech**

In the past few years at Dr. Donald Lie's RF/Analog-SoC lab, continuous and dedicated efforts towards improving the 2.4 GHz Doppler-radar based NCVS sensor have resulted in four generations of discrete PCB designs. Each generation achieved different levels of improvement and the related study and observations were published in various conferences internationally [31], [36], [41], [42], [43]. The first generation design consisted of single-channel direct conversion receiver PCB and the analog signal processing was initially implemented using high-precision SR560 low-noise pre-amplifier but later the bulky and expensive SR560 was replaced with an analog-signal processing PCB with equivalent functionalities. The analog data was digitized using a NI-DAQ and was analyzed using MATLAB based algorithms. The first generation NCVS system used patch antennas for transmitting and receiving the RF signals. The major improvement achieved through the first generation design was the replacement of the SR560 pre-amplifier with a portable analog signal processing PCB. Since the RF transceiver was based on single channel architecture, it needed to be changed to overcome the related disadvantages such as the null-point problem [33].

The second generation design was improved by changing the single-channel receiver with a quadrature receiver and the arc-tangent demodulation technique was used to combine the two quadrature signal channels. The analog signal processing architecture remained the same as the first generation with Sallen-Key band-pass filter and low-noise op-amp based amplifier. The third generation NCVS sensor was designed to make the entire NCVS system more portable and this was achieved by combining the RF-transceiver PCB and analog signal processing PCB onto a single PCB. The second and third generation systems both used the PCB-YAGI antennas. The fourth generation PCB, which is the current NCVS system, uses a frequency synthesizer instead of the VCO and also has a gain-booster block to boost the LO signal; and like the third generation PCB it has both the RF section and analog section on one PCB. Another feature of the fourth generation PCB is that it has the low-dropout (LDO) power supplies on the PCB, thus increasing the portability and can be charged by the wall power socket. Additionally, the fourth generation system uses the custom built helical antenna, though it can still use other different kinds of antennas.

Each generation has improvements in not only the hardware but also the signal processing schemes to make it more robust and real-time. In the first generation only autocorrelation was used, whereas in the second and third generations the vital signs were estimated using three different techniques: Fast-Fourier Transform (FFT) in frequency domain, time-domain auto-correlation and peak-detection, and FFT of the auto-correlated output [34]. The fourth generation uses system time-domain auto-correlation followed by a FFT and then the peak-detection to estimate the cardio-pulmonary rates [36]. In all the generations except for the fourth generation, the signal processing was done over the accumulated set of data and the result was displayed at the end of the data acquisition. However, for the fourth generation system, the respiration rate and the heart rate are made available almost real-time, with only the exception of the first 30s required for filter settling.

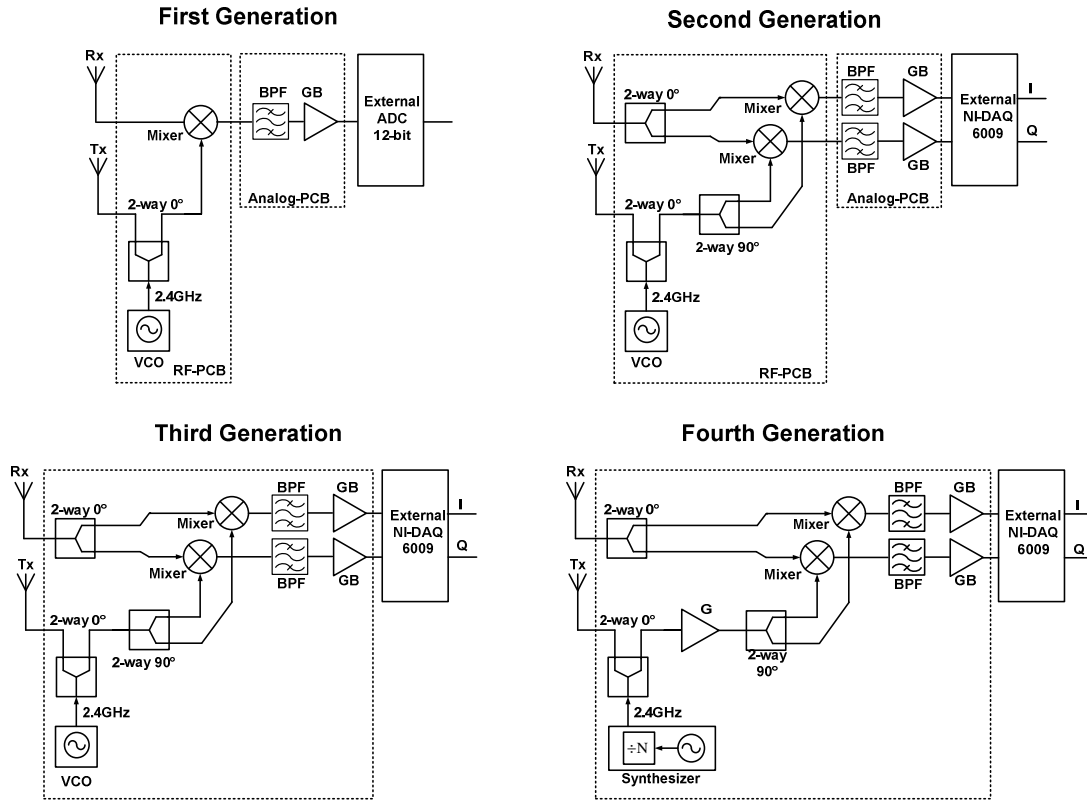


Fig. 1.12 The four generations of NCVS sensor hardware developed at Prof. Donald Lie’s Lab at the Texas Tech University [34]

In all the implementations two antennas were used, one for the transmit path and one for the receive path for each sensor, instead of using the bulky circulator. This was done to avoid self-mixing, which may result from the inadequate transmit-to-receive port isolation on the circulator. Since self-mixing is one of the contributors of dc-offset, not using a circulator helps in reducing dc-offsets [44]. Additionally, using a bulky circulator will make it very difficult for the sensor to be integrated as a System-on-a-Chip (SoC) in the future. The different generations of NCVS sensors developed in Dr. Donald Lie’s lab are shown in Fig. 1.12. The first, second and third generation systems were designed by Mr. Ravi. Ichapurapu, Dr. Jerry Lopez and the team. The fourth generation system was designed by Mr. Alex Boothby, Dr. Jerry Lopez and the team. The 10.24 MHz reference oscillator required for the frequency synthesizer on the fourth generation system was designed by myself.

Over the past decade considerable research has been done and systems with excellent accuracy for respiration rates and also with reasonable accuracy for heart rate detection have been reported for Doppler-based NCVS sensors placed at a distance of 0.5m to 1m [29], [30], [31]. The considerably inferior accuracies of heart rate detection vs. respiration rate detection are due to the physiological nature of the respective signals. Since the heart lies beneath the chest wall, the periodic cardiac movement is subdued by the stronger periodic pulmonary movement (thus masking the cardiac signal). The overwhelming pulmonary signal with its movement is orders of magnitude larger than the cardiac signal (i.e., mm heart movements vs. cm chest diaphragm movements), making the detection of heart rate a challenge for the NCVS sensors [29], [30]. Apart from the obvious advantages, the NCVS sensors suffer from problems related to strong background clutter picked up by the RF receiver system, along with the small cardiac signals, the motion artifacts due to the patient's movements (or movements of individuals around the patient), and possible PCB and circuit-level signal losses with added noise due to mismatches and parasitics at RF frequencies. The harmonic interference due to the harmonics of a much stronger respiration signal can also overwhelm the heart signals sometimes, leading to serious consistent heart rate detection issues [30], [35], [45]. Algorithms for random-body movement cancellation and harmonic cancellation have been reported, but they have not been able to provide the required robustness to convert the Doppler-based NCVS system into full-fledged products capable of being installed at hospitals, nursing homes or residential complexes for vital signs monitoring. Recently, the FDA has approved the first Doppler-based NCVS system developed by Kai Sensors (HI, USA) called the Kai RSpot, for non-contact respiration rate check only. In 2012 Kai Sensors (HI, USA) have obtained the patent for Doppler-based NCVS system which can be used for apnea therapy, patient identification, sway cancellation and multi-parameter vital signs monitoring [46]. But still, the application of Doppler-based system for heart rate detection remains a big challenge.

## 1.4 Summary of Heart Beat Sensing Techniques

With the various types of heart beat sensing techniques like the wearable ECG sensors, implantable cardioverter defibrillators (ICD)/pacemakers and the Doppler-based non-contact biosensors discussed thus far, it is imperative to investigate the efficient techniques to realize robust and reliable heart rate sensing for a given application. The objective of my research is to understand the system level details and try to derive important design paradigms which would make the existing systems more robust, reliable and power-efficient. A system-level comparison has been shown in Table.1.1, and as can be observed that each of the heart beat sensing technology has its own share of pros and cons. For example, the wearable ECG sensors have better detection accuracy but the use of various electrodes is a cause of discomfort for the monitored patient, thus hampering long-term cardiac monitoring. In the case of pacemakers/ICDs, administering pacing/defibrillation requires a proper knowledge of the instantaneous state of heart deflections, since if the defibrillation is provided during a T-wave instead of the R-wave it can escalate the fibrillation leading to lethal consequences [3]. Furthermore, defibrillation or pacing is effectively realized only by using the electrode-lead assembly and the sensing-defibrillation module implanted inside the human body. This needs a vascular surgery which is a definite impediment to be used on some patients, even though recently the subcutaneous-ICD (S-ICD<sup>®</sup>) mentioned earlier may be able to alleviate this serious transvenous surgical pains and electrode-lead failures in the future. On the other hand, the use of NCVS sensor systems for continuous monitoring appears to be attractive for its higher comfort level and relatively relaxed power requirements, but this technology can be plagued with less reliable heart rate detection accuracy due to various artifacts and clutters. The NCVS sensor system records the periodicity of the physical heart movement as rather than the exact heart beat signal, making it impossible to be used for defibrillation; therefore a NCVS sensor system is unlikely to replace the contact-based heart sensing technologies, but will be an excellent complimentary technique to provide ubiquitous and continuous monitoring, especially for sleep apnea, etc. For each monitoring

scenario for a given patient, the optimal choice of one or a combination of the three heart rate sensing techniques requires some knowledge of understanding the limitations and strengths with each system.

Table.1.1 Heart beat sensing techniques – a comparison

	<b>Wearable Electrocardiogram (ECG) Sensors</b>	<b>Implantable Cardioverter Defibrillator (ICD)/ Pacemaker</b>	<b>Doppler-based Non- Contact Vital Signs (NCVS) Sensor</b>
<b>Method</b>	Body surface contact	Intra-cardiac contact	No contact
<b>Signal</b>	ECG	EGM	Reflected phased-modulated signal
<b>Low Power Consumption</b>	Critical	Extremely-critical	Less critical
<b>Power Supply</b>	Battery	Li-ion battery	Wall-power or batteries
<b>Position</b>	On the body	Inside the body	Away from the body
<b>Comfort Level</b>	Low	Moderate	High
<b>Robustness (detection accuracy)</b>	High	High	Low
<b>Therapy</b>	None	Defibrillation / Pacing	None
<b>Miniature Form-factor</b>	Recommended	Required	Not critical
<b>Sensing Circuit</b>	Analog	Analog	RF-Analog
<b>Wireless Connectivity</b>	Can be done	Can be done	Can be done

## CHAPTER 2

### **ANALOG FRONT-END DESIGN AND SIMULATION OF BIO-SENSOR: ECG AND ICD/PACEMAKER**

The growing needs for important biosensor systems such as the wearable ECG sensors and implantable pacemaker/ICD in the healthcare industry have pushed for the continuous improvements in the biosensor design. Some of the most critical requirements for effective biosensor systems are the low-power consumption and the miniature form factor, as they can make high-quality and ambulatory healthcare services available even for patients in remote and rural areas. Biosensors are often used for continuous monitoring of biosignals, which are inherently analog in nature and can be electrical signals. This analog characteristic of the biosignals necessitates the design of analog-front end (AFE) circuitry as the signal sensing block in the biosensors. For continuous monitoring, this AFE circuitry needs to be continually operational throughout the life of the biosensor. Thus, if the power consumption of the AFE circuitry can be reduced, then the operational longevity and the effectiveness of the biosensor systems can be improved.

The AFE circuitry of a bio-sensor is required to sense the biosignal and subsequently carry out the necessary signal processing. The nature of the biosignals defines design criteria of the AFE circuitry. Biosignals such as the ECG and intra-cardiac EGM have low amplitudes in the order of tens of  $\mu\text{V}$  to tens of mV and provide diagnostic information at low frequencies in the range of dc to few hundred Hz, as can be seen in Table.2.1 [3], [4], [21]. Such low amplitude and frequency ranges require the AFE to amplify as well as low-pass filter the biosignals in order to filter out the out-of-band noise to extract the desired physiological information. At such low frequencies it is typical to encounter the flicker noise and with such low signal amplitudes this noise can prove to be very detrimental for a biosignal acquisition. After the amplification and filtering stages the AFE is required to help digitizing the analog physiological signals for the following digital signal processing

(DSP) stage. The DSP stage does not form a part of the AFE, but is equally critical as it is here where the various diagnostic and monitoring algorithms are executed to make best use of the information offered by the biosignal. Since the AFE circuitry determines the quality of the extracted biosignal to efficiently process these signals the AFE circuitry needs to be designed with low input referred noise, tunable bandwidth and reconfigurable gain [47]. Advances in CMOS technology as well as low-power, low-noise circuit design techniques can help us to design robust, efficient and battery friendly AFE circuits capable of continuous and reliable cardiac monitoring. A typical wearable ECG sensor was discussed in the preceding chapter and is being shown here again in Fig. 2.1

Table.2.1 Biosignal : Amplitude and Frequency range [3], [4], [21]

Bio-Signal	Amplitude Range	Frequency Range
ECG	0.5mV – 4mV	0.01Hz -250Hz
EKG	100 $\mu$ V – 20mV	dc – 100Hz

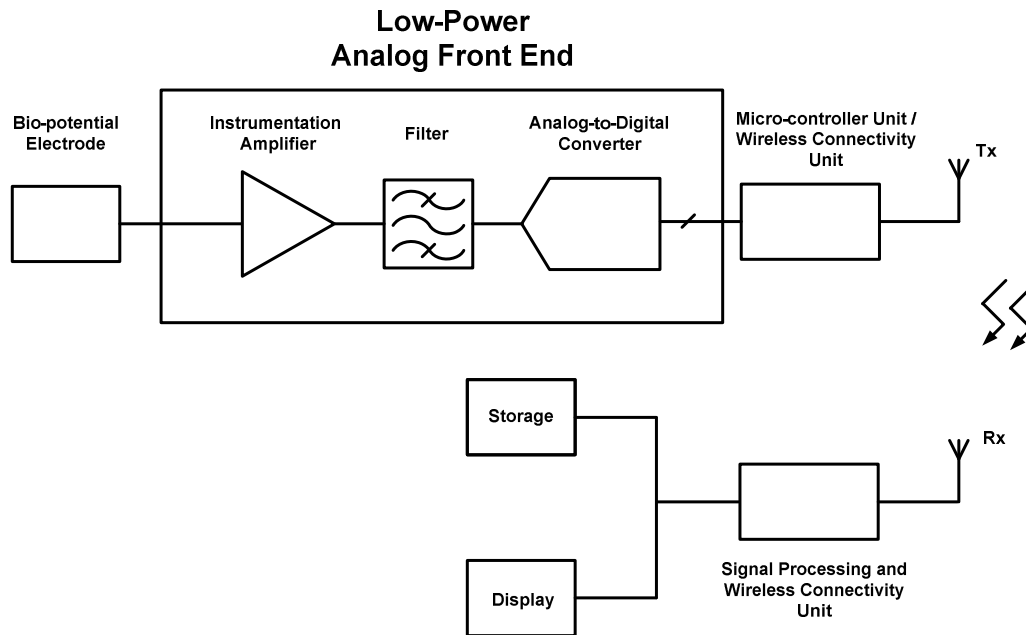


Fig. 2.1 A typical wearable ECG sensor showing the AFE circuitry.

## 2.1 Biosignal Instrumentation Amplifier (INA)

The instrumentation amplifier (INA), as shown in Fig. 2.1, is the first stage of the AFE circuitry and hence is responsible for defining the overall performance of the biosignal AFE circuitry. The INA interfaces the subsequent AFE circuits and electrodes, and hence it has to be designed considering the characters of both. Biosignals are usually associated with electrode dc-offsets, which in the case of ECG arise due to the half-cell potentials of the electrode-electrolyte and electrolyte-skin interfaces [3]. The half-cell potential develops at the electrode-electrolyte interface because of the oxidation-reduction chemical reaction between the constituents of the electrode and aqueous electrolyte. The current across the electrode-electrolyte interface consists of the electrons ( $e^-$ ), cations ( $C^+$ ) and anions ( $A^-$ ), as shown in Fig.2.2 [3]. The continuous chemical reaction at the interface brings about changes in the concentration of cations and anions at the electrode-electrolyte interface, leading to the electrode acquiring net negative charge and the electrolyte acquiring net positive charge. This polarization results in a potential difference known as half-cell potential. For EGM, the electrode offsets can be attributed to the formation of a dense fibrous capsule around the intra-cardiac electrode [22].

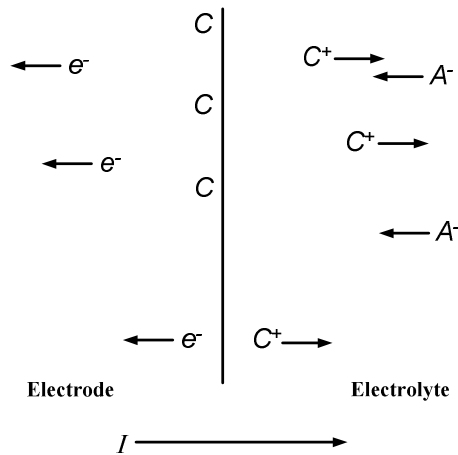


Fig. 2.2 Electrode-electrolyte interface. [3]

Biosignals offer physiological information in the low frequency range (on the order of few Hz) and therefore the in-band noise is often dominated by the  $1/f$  noise. Moreover the presence of the common-mode 60Hz signal due to mains-power line is always a strong noise source. In view of the above facts, the INA is required to filter the electrode dc-offsets, suppress the in-band  $1/f$  noise and reject the common-mode signal to increase the sensitivity to cardiac biosignals [47].

In order to seamlessly interface with the biopotential electrodes, the bio-signal instrumentation amplifier needs to be designed to provide high impedance at the amplifier inputs to avoid loading the bio-potential electrodes. Additionally the INA must be able to suppress the electrode dc-offsets. A typical electrode-INA interface is shown in Fig. 2.3 [3], [48], [49]. The series resistance  $R_s$  may be of the order of  $2k\Omega$ , whereas the  $R_d$  and  $C_d$  are in the range of  $2M\Omega$  and  $50nF$  [47]. The electrode-impedance model is a frequency-dependent model: at high frequency, where  $\frac{1}{j\omega C_d} \ll R_d$ , the electrode impedance value is very close to  $R_s$ ; whereas at low frequency for  $\frac{1}{j\omega C_d} \gg R_d$  the electrode impedance value is given as  $R_s + R_d$ . Since the electrode offsets can be large, possibly in the range of tens of mV, they need to be filtered out using a high-pass filter having a very low-cut-off frequency close to dc [47], [53]. Use of a dc servo-loop in the INA design to discard the electrode dc – offsets also has been reported [50], [54].

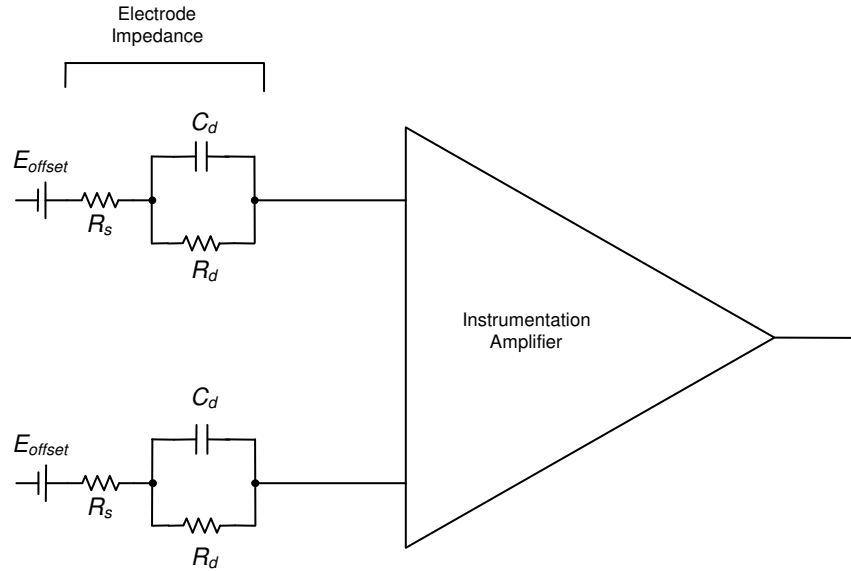


Fig. 2.3 Electrode-INA interface, showing the electrode impedance and electrode offsets [3], [48], [49].

### 2.1.1 Design Consideration

The noise floor of the INA predominantly decides the sensitivity of the AFE circuitry and therefore the biosensor. A noise floor power spectrum density (PSD) of  $100\text{nV}/\sqrt{\text{Hz}}$  over a bandwidth of dc to 250Hz, which is the ECG frequency band, gives an integrated noise value of close to  $1.6\mu\text{V}_{\text{rms}}$  [50]. Commercially available ECG monitoring AFE ICs like ADAS1000 (Analog Devices) and ADS129R (Texas Instruments) achieve noise specifications close to  $2\mu\text{V}_{\text{rms}}$  [51], [52]. This is the expected noise amplitude in the ECG frequency range, and therefore a biosignal with amplitude *larger* than this noise amplitude can be detected by the amplifier with a noise floor PSD of  $100\text{nV}/\sqrt{\text{Hz}}$  or less. The closed-loop dc gain of the INA can be designed in a range of 20 dB to 40 dB depending upon the gain characteristics of the subsequent stages. The common-mode rejection ratio (CMRR) is another important design spec consideration, ideally for battery operated implantable devices a CMRR of greater than 80 dB would be sufficient as it means a suppression of common-mode signal by 10,000 times in comparison with the differential signal [47], [50]. However

for wearable biosensors such as ECG sensors, the commercial INAs often need to achieve a CMRR of over 130 dB to effectively remove all the undesired effects due to mismatches and motion artifacts, etc. [51], [52]. The power-supply rejection ratio (PSRR) specification of the amplifier is also considered for a robust design, as this makes sure that any fluctuation on the power-supply is attenuated so as not to influence the amplifier output significantly. PSRR ratings of greater than 60 dB is considered sufficient for battery operated devices [47]. Since the high precision biomedical AFE circuits cater to not only battery-operated devices only, they can often achieve a PSRR of 90 dB [52]. In addition, the AFE devices from Analog Devices Inc. and Texas Instruments offer wide range of features like configurable gain, tunable noise-power performance, thoracic/respiration impedance measurement, to name a few [51], [52]. The operational longevity of wearable ECG sensors or ICD/pacemakers, to a large extent, is determined by the capacities of Li-ion batteries and the current consumption of the AFE circuitry. This operational longevity can be expressed as,

$$\text{Operational Hours} = \frac{\text{Battery Capacity}}{\text{Current Consumption}} \quad (2.1)$$

According to equation (2.1), a battery capacity of 1.2Ah and current consumption of  $20\mu\text{A}$  gives an operational lifetime of close to 7 years; however this simple calculation does not take into account the deterioration of the battery and circuit performance over the years.

In the pursuit for a low-power and efficient AFE circuitry design, at Dr. Lie's lab the impetus is given towards trying various circuit design techniques to cater to the design requirements of an ultra-low power biosignal AFE circuitry. One of the most important techniques is the design of low-power INA using the chopper stabilization. Chopper stabilization is an elegant method of mitigating the flicker noise and has been explored extensively for biosignal acquisition systems [12], [47], [50], [54], [55], [56].

In this chapter, I will discuss the design of two low-power chopper stabilized INAs for robust cardiac monitoring, based on the specifications and requirements discussed before. To be more exact, the chopper-stabilized INA circuit implementation is aimed at achieving the design specifications listed in Table 2.2

Table.2.2 Design Specification [50]

Amplifier Parameter	Target Specification
Supply Voltage	$< 2 \text{ V}$
Supply Current	$< 2 \mu\text{A}$
Closed-loop dc-Gain	20 – 40 dB
Noise [dc – 250Hz]	$< 2 \mu\text{V}_{\text{rms}}$
CMRR	$> 80 \text{ dB}$
PSRR	$> 60 \text{ dB}$
Bandwidth	$> 5 \text{ kHz}$

## 2.2 Chopper Stabilization Technique

The chopper-stabilization technique has been used in the past for realizing high-precision dc-gains with ac-coupled amplifiers [56]. Recently, this technique has generated interest as an efficient method to suppress the effects of flicker noise as well as of the dc-offset, which are inherent in MOSFET-based INA designs [58]. Chopper stabilization or chopper modulation in a real-sense does not suppress the noise; rather it just transposes the low frequency noise to distinct out-of-band frequencies by design, making it easier to discard the undesired noise. Chopper stabilization provides a solution to remove this in-band low frequency noise in biosignals such as in the cardiac signal, and hence has been reported to be used recently for various biosignal instrumentation amplifiers [12], [47], [50], [54], [55], [57].

Chopper stabilization is realized with the aid of a combination of modulator and demodulator, which are placed in the input and output signal path of the amplifier, as shown in Fig.2.4. The modulator and demodulator are essentially CMOS switches

which are switched at a higher frequency than the baseband biosignal, using a square-wave signal as the input to switches.

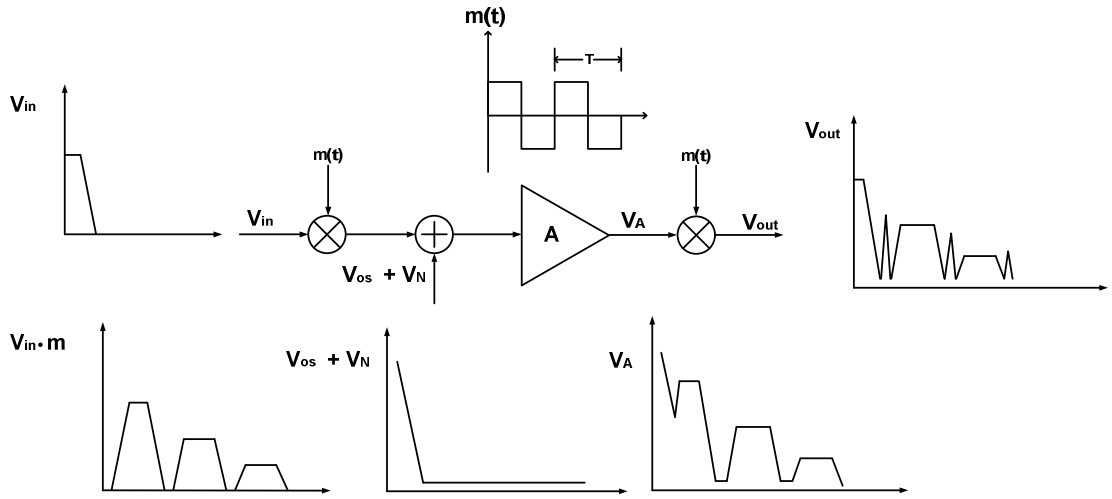


Fig. 2.4 Chopper stabilization technique [56]

The Fourier representation of a square wave is shown in equation 2.2, where  $f_{chop}$  is the modulation frequency also known as the chopper frequency.

$$m(t) = \frac{4}{\pi} \sum_{k=1}^{\infty} \frac{\sin((2k-1)2\pi f_{chop}t)}{(2k-1)} \quad (2.2a)$$

$$m(t) \approx \frac{4}{\pi} \left( \sin 2\pi f_{chop}t + \frac{1}{3} \sin 2\pi(3f_{chop})t + \frac{1}{5} \sin 2\pi(5f_{chop})t + \dots \right) \quad (2.2b)$$

The input signal,  $V_{in}$  is modulated by the square-wave modulator and as seen in equation (2.2b), where the square-wave signal  $m(t)$  can be represented as a series of odd harmonics, and hence the input signal is translated to the odd-harmonics of the chopper frequency. The signal after the chopper modulator action, shown as  $V_{in} \cdot m$  lies in the vicinity of the chopper frequency, while at this higher frequency the signal does not suffer from the semiconductor flicker-noise and is also amplified by the instrumentation amplifier. After this, the amplified signal  $V_A$  is demodulated by the chopper demodulator in the output signal path. This demodulation results in the output signal  $V_{out}$ , which is at baseband, and it is amplified with almost no effects of flicker-

noise and dc-offset. Since the flicker-noise  $V_N$  and dc-offset  $V_{OS}$ , are introduced into the system only after the first chopper modulator, they encounter only one set of chopper switches, and that is at the output path. This arrangement translates  $V_N$  and  $V_{OS}$  to the odd harmonics of the chopper frequency. As can be seen in Fig. 2.4, the output signal  $V_{out}$  contains not only the desired signal but also its harmonics, along with the translated noise and dc offset. Note the harmonics, noise and dc-offset in the output signal are at a higher frequency outside the band of interest of the biosignal, and are easily filtered using a subsequent filtering stage. The chopper modulation technique separates the unwanted in-band flicker noise and dc-offset from the signal, thus making further signal processing simpler. A more detailed analysis and explanations will be given next.

### 2.2.1 Noise Analysis – Chopper Stabilization

It is interesting and necessary to analyze the behavior of noise in light of the chopper stabilization in order to minimize its effects and make the instrumentation amplifier and subsequently the entire AFE circuitry more sensitive for biosignal acquisition. A representation of the chopper modulation of noise is shown in Fig. 2.5, where  $V_N(t)$  is the noise, for an instrumentation amplifier it is the input referred noise of the amplifier and  $V_{CS}(t)$  is the chopper modulated output. The chopper modulation signal shown as  $m(t)$  has a frequency,  $f_{chop} = 1/T$ .

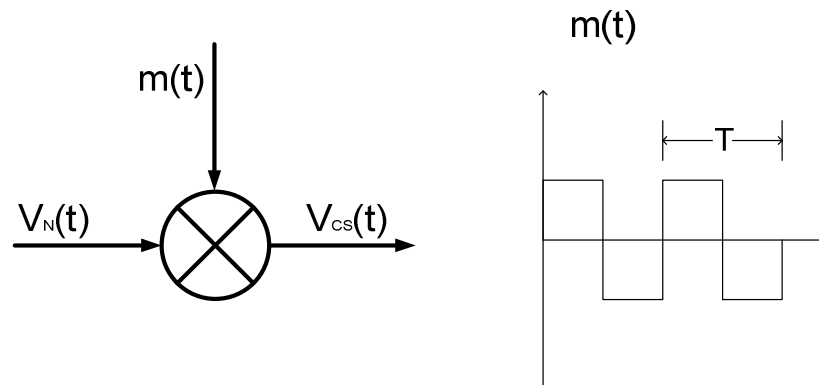


Fig. 2.5 Chopper modulation of noise [56].

The low-frequency input-referred noise power spectrum density (PSD) of an amplifier typically has white noise and flicker noise components, and can be expressed as [56],

$$S_N(f) = S_0 \left( 1 + \frac{f_{corner}}{f} \right) \quad (2.3)$$

Here  $S_0$  represents the white-noise power spectrum density (PSD) and  $f_{corner}$  is the amplifier noise corner frequency. The PSD of the chopper modulated signal,  $V_{CS}(t)$  is given as [56],

$$S_{CS}(f) = \left( \frac{2}{\pi} \right)^2 \sum_{\substack{n=-\infty \\ n \text{ odd}}}^{+\infty} \frac{1}{n^2} S_N \left( f - \frac{n}{T} \right) \quad (2.4)$$

At baseband, ( $f/f_{chop} \leq 0.5$ ) equation (2.4) can be approximated with a white-noise PSD expressed as [56],

$$S_{CS}(f) \approx S_0 \left[ 1 - \frac{\tanh \left( \frac{\pi f_{3dB}}{2 f_{chop}} \right)}{\frac{\pi f_{3dB}}{2 f_{chop}}} \right] \quad (2.5)$$

Here  $f_{3dB}$  is the amplifier 3-dB cutoff frequency. On further simplification for the condition,  $\frac{f_{3dB}}{f_{chop}} \gg 1$ , we get [56],

$$S_{CS}(f) \approx S_0 \quad (2.6)$$

Thus, it can be seen from equation (2.6) that at baseband, for an amplifier with its 3-dB cutoff frequency much faster than the chopper frequency, the noise after chopper modulation is almost equal to the white-noise or thermal noise of the amplifier. This phenomenon is due to the fact that in chopper stabilization technique, noise is neither sampled nor held, instead is periodically inverted without affecting the

time-domain properties of noise [56]. According to [56] there exists an asymptotic relationship between the chopper modulated noise and thermal noise and due to which it is observed that for  $\frac{f_{3dB}}{f_{chop}} > 6$  the chopper modulated noise becomes almost 90% of the original thermal noise,  $S_0$ .

The chopper modulated flicker noise ( $1/f$ ) noise of the amplifier which has a 3-dB cutoff frequency much larger than the chopper frequency,  $\frac{f_{3dB}}{f_{chop}} \gg 1$  can be expressed as [56],

$$S_{CS-flicker}(f) \cong 0.8525 S_0 \frac{f_{corner}}{f_{chop}} \quad (2.7)$$

Thus the total noise at baseband ( $f/f_{chop} \leq 0.5$ ) after chopper stabilization is given as [56],

$$S_{CS}(f) \cong S_0 \left[ 1 + 0.8525 \frac{f_{corner}}{f_{chop}} \right], \text{ for } \frac{f_{3dB}}{f_{chop}} \gg 1 \quad (2.8)$$

From the above analysis and equations it can be observed that the baseband noise after chopper stabilization depends on two ratios,  $\frac{f_{3dB}}{f_{chop}}$  and  $\frac{f_{corner}}{f_{chop}}$ . If the two ratios can be reduced then the baseband noise can be reduced and fortunately the ratios can be reduced by simply increasing the  $f_{chop}$ , that is the chopper frequency. But there is a trade-off as increasing the  $f_{chop}$  leads to higher residual offset due to clock-feedthrough and charge injection [56], as can be seen from equation (2.9)

$$V_{OS} \cong 2\tau f_{chop} V_{spike} \quad (2.9)$$

Here  $V_{OS}$  is the residual offset  $\tau$  is the time-constant and  $V_{spike}$  is the amplitude of the parasitic spikes, as shown in Fig. 2.6

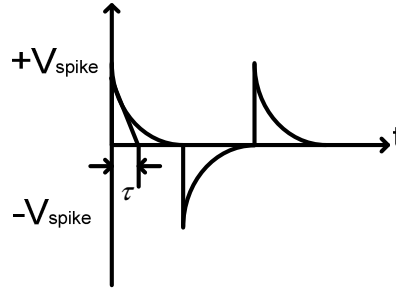


Fig. 2.6 Spikes due to chopper modulation [56].

To minimize the baseband noise,  $\frac{f_{3dB}}{f_{chop}}$  can be minimized by reducing the amplifier 3-dB cut-off frequency,  $f_{3dB}$ . But the amplifier cut-off frequency must be made larger than  $f_{chop}$  to provide stable gain without any distortion as after the first stage of chopper modulation the input signal would be translated to frequencies close to  $f_{chop}$ . Hence a reasonable compromise is to select  $f_{chop} = f_{corner}$  and to have  $f_{chop} \ll f_{3dB}$  [56], [59].

### 2.3 Differential Difference Amplifier based chopper stabilized INA

A chopper-stabilized INA based on Differential Difference Amplifier (DDA), as shown in Fig. 2.7, was implemented to meet the above mentioned characteristics shown in Table 2.2 [12], [55]. DDA topology enables high CMRR since the amplifier CMRR is only dependent on the input port mismatches [55], [60]. The mismatches in the resistors used for the feedback and gain setting only influence the closed-loop gain of the amplifier. A conventional three-op-amp instrumentation amplifier can also serve the purpose well, but high CMRR is achievable only if the resistors as well as the each of the amplifiers are precisely matched. Accurate laser-trimming can be used, but that raises the cost of the design [47], [55]. By adopting the DDA topology proposed here, the closed-loop gain of the amplifier can be accurately determined by the ratio of the on-chip resistors.

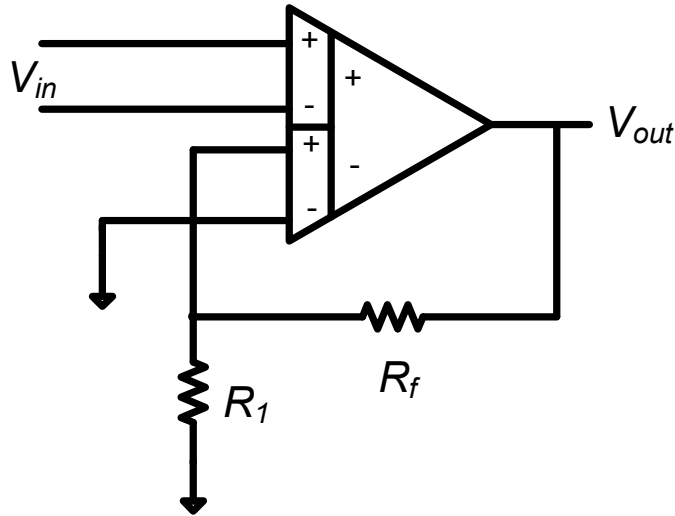


Fig. 2.7 DDA-based INA [55], [60].

### 2.3.1 Differential Difference Amplifier (DDA)

The Differential Difference Amplifier (DDA) as shown in Fig. 2.8, is an extension of the typical operational amplifier (op-amp) [60]. Analogous to the op-amp, the DDA also uses the principle of comparing the two input voltages, where the only difference being that the two input voltages are differential in nature. The comparing character is necessary in overcoming the variations caused by the process and temperature dependence of the device parameters. The DDA topology achieves high CMRR and exhibits high input impedance, these features are essential for bio-signal amplifier. When used as an INA, the CMRR performance is affected only by the mismatch at the input pair devices [60].

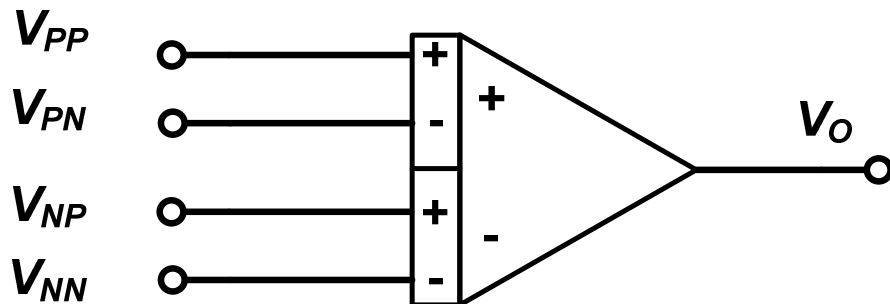


Fig. 2.8 DDA symbol [60].

The ideal DDA will amplify the small-signal input differential voltage  $v_D$ , by almost infinite amount and also provides an ideal common-mode rejection. The principle of operation of an ideal DDA can be expressed as [60],

$$v_O = \mu v_D = \mu [(v_{PP} - v_{PN}) - (v_{NP} - v_{NN})], \text{ where } \mu \rightarrow \infty \quad (2.10)$$

A more general and explicit expression for the DDA principle can be given as,

$$v_O = k [f_P (v_{PP} - v_{PN}) - f_N (v_{NP} - v_{NN})], \text{ where } k \rightarrow \infty \quad (2.11)$$

Equation (2.11) holds good if  $f_P(v) = f_N(v)$  and  $\frac{df(v)}{dv} \neq 0$ . The DDA principle is depicted in the Fig.2.8. The differential input voltage at each terminal is converted to respective differential current by the transconductor action, expressed as  $f_P(v)$  and  $f_N(v)$ . The subsequent subtraction of the differential currents,  $\Delta I_P$  and  $\Delta I_N$  is realized using the connection shown in Fig. 2.9. The resultant differential current  $\Delta I_D$  is amplified by a factor of  $k \rightarrow \infty$  to obtain the output voltage.

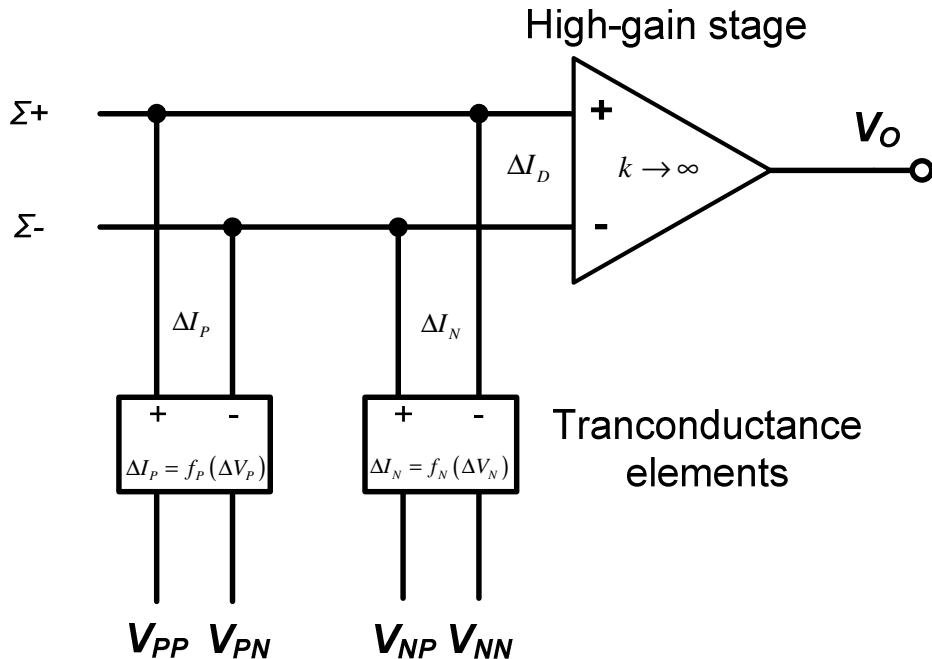


Fig. 2.9 The DDA operation principle [60].

### 2.3.2 Chopper Switches

The chopper switches were realized using complementary MOS devices, as shown in Fig. 2.10. Complementary switching scheme can relieve the charge injection and clock feed-through issues [59], [61]. In this proposed design, a chopper modulation frequency ( $f_{\text{chop}}$ ) of 5 kHz was supplied to a non-overlapping clock generator to generate two clocks, P1 and P2, and their complementary clocks P1' and P2' were obtained using subsequent inverter stages. Higher chopper frequency would require higher bandwidth for the amplifier as the intermediate modulated signal would be in the vicinity of the chopper frequency, so as to avoid signal attenuation. Higher bandwidth translates into higher power requirements.

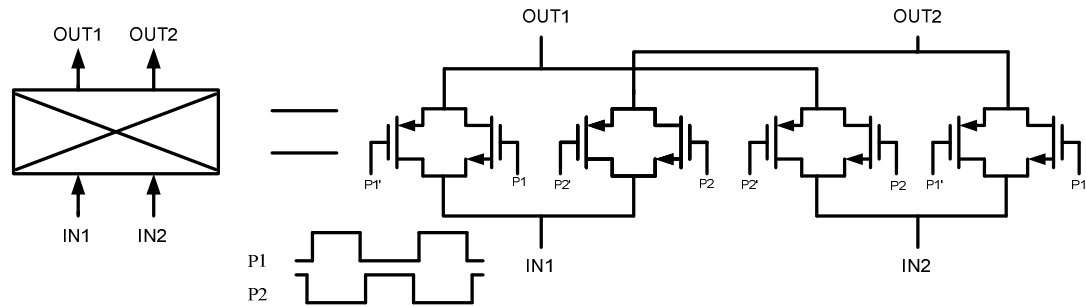


Fig. 2.10 The chopper switches design schematics

### 2.3.3 DDA-based chopper stabilized INA – Circuit and System Design

A block level diagram of the INA is shown in Fig. 2.11, where the design includes a selective feedback arrangement controlled using two control signals. This feedback arrangement makes it possible to use the INA for both the EEG signal (requiring a gain of 40 dB), and for the ECG signal (requiring a gain of 20 dB). The output chopper modulator is realized using two chopper switches. For the sake of simplicity, the block level representation in Fig. 2.11 shows the switches as one combined unit. The DDA-based chopper stabilized INA design was implemented in a proprietary Texas Instruments (TI) LBC7 0.35 $\mu\text{m}$  Bipolar-CMOS-DMOS (BCD) technology and was co-designed with Weibo Hu, who is a Ph.D student under Dr. Lie.

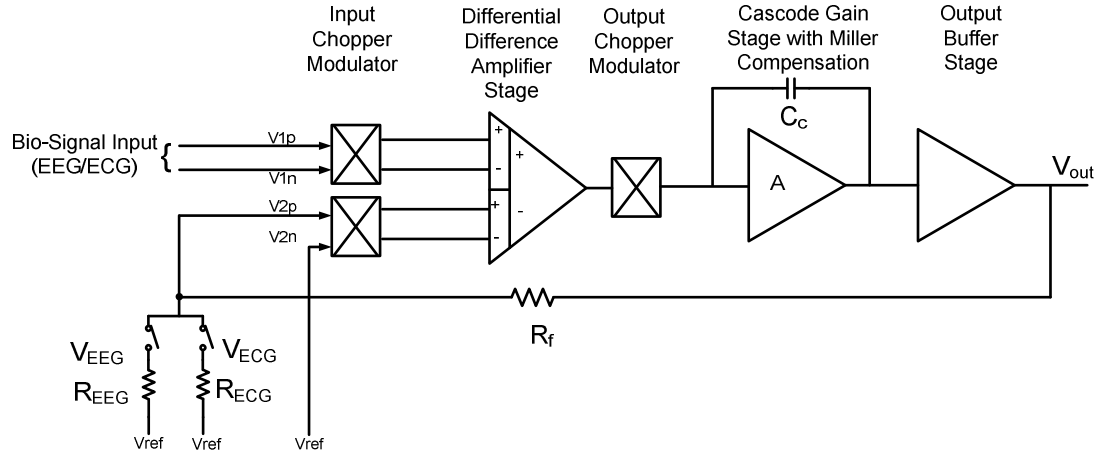


Fig. 2.11 A block diagram of the proposed chopper stabilized INA

The AFE INA is a three stage amplifier wherein the two input differential pairs constituting the first stage are the positive and negative inputs of the DDA. The detailed schematic level diagram is shown in Fig. 2.12. The first stage is the transconductance stage, where the chopper modulated input bio-signal voltages are converted to corresponding current signals. The input chopper stabilization is realized using two chopper switches. The current domain signals are added and then converted back to voltages by the active cascode loads ( $M_{17}$ - $M_{19}$  and  $M_{18}$ - $M_{20}$ ). This voltage signal is then demodulated by another pair of chopper switches placed in the output path [55]. One of the output choppers is placed between the cascode mirror circuit and the other output chopper is placed between the active PMOS loads. The dual chopping functionality embedded in the active loads periodically connects the output of each half-circuit of the differential pair to the subsequent single ended cascode amplifier. The cascode amplifier forms the second stage, which is also connected to the first stage by a Miller compensation capacitor for stabilization. The third stage is a source follower, which forms the buffer. The output signal of the instrumentation amplifier is single-ended and chopper stabilized. The proposed design uses low- $V_T$  devices as cascode device in realizing the current mirror biasing circuitry. Low- $V_T$  devices help in cascoding without the need for extra biasing, where cascoding of the current mirror

circuit provides more matching and better current replication. The low- $V_T$  devices have been highlighted in blue in Fig. 2.12.

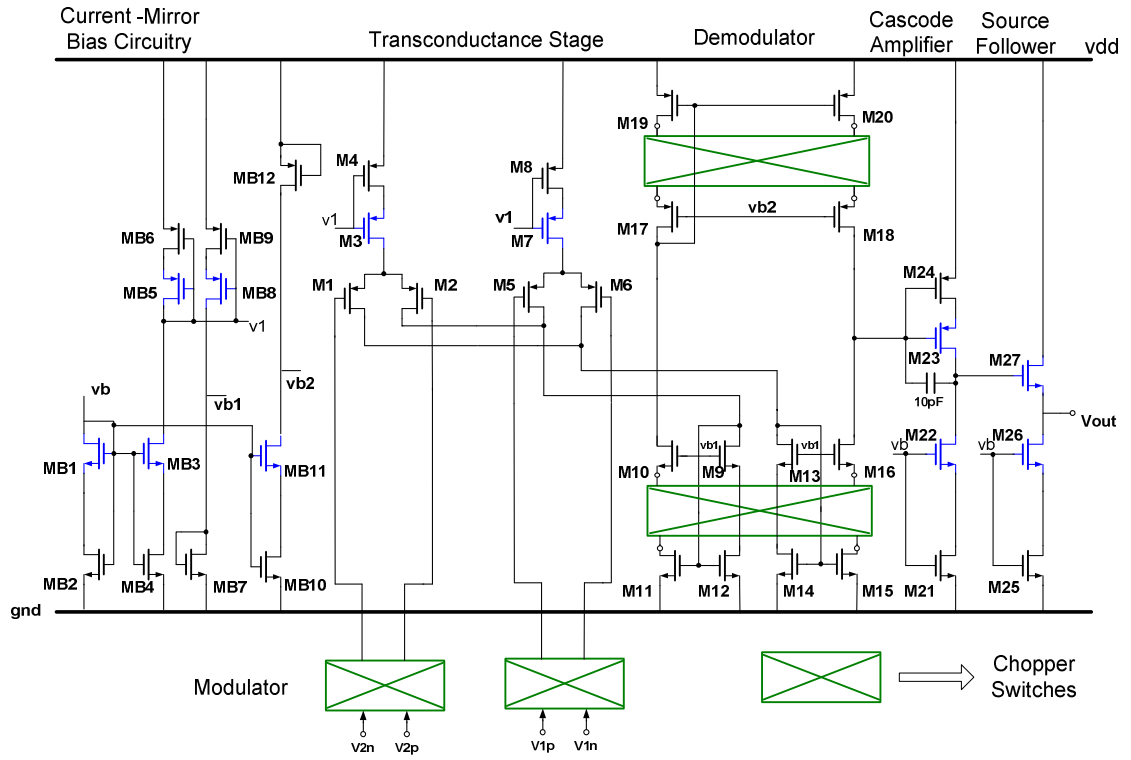


Fig. 2.12 The schematics of the chopper stabilized DDA-INA .

The commutative action of the output chopper pair for the case of clock P1 “High” and clock P2 “Low” can be understood from the diagram shown in Fig. 2.13. As can be seen, colored arrows have been used to represent the flow of the biasing currents through the demodulator and the active load configuration. The blue arrows represent  $I_2$  and the red arrows represent  $I_1$ . During clock P1 High and clock P2 Low, the chopper switches enable a direct connection between the transistors,  $M_1$ - $M_3$ ,  $M_5$ - $M_7$ ,  $M_9$ - $M_{11}$ , and  $M_{10}$ - $M_{12}$ , which allows for the mirroring of current  $I_2$ . A similar direct connection between transistors  $M_2$ - $M_6$ , and  $M_4$ - $M_8$  allows for the mirroring current  $I_1$ . The output is obtained at the high impedance node formed by transistors  $M_4$  and  $M_{10}$ . Transistors  $M_4$ - $M_8$  and  $M_{10}$ - $M_{12}$  form cascode pairs for NMOS and

PMOS devices, respectively. Since cascoding the node formed by the nodes of  $M_4$  and  $M_{10}$  is a high impedance node, thus it provides higher small-signal gain.

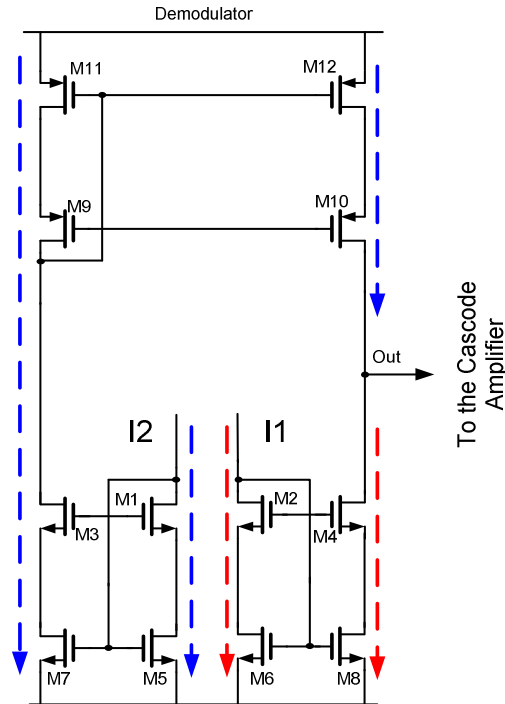


Fig. 2.13 The schematics of the chopper stabilized DDA-INA, for the clock P1 “High” and clock P2 “Low”.

Similarly the commutative action of chopper switches for the case of clock P1 “Low” and clock P2 “High” has been depicted in Fig. 2.14. Similar to Fig. 2.13, the blue arrows represent  $I_2$  and the red arrows represent  $I_1$ . Under the present clock condition the chopper switch enables a cross-coupled connection between the transistors,  $M_4$ - $M_7$ , which allows for a mirroring of  $I_2$  to  $M_4$ . The cross-coupling between the transistors  $M_3$ - $M_8$ ,  $M_9$ - $M_{12}$ , and  $M_{10}$ - $M_{11}$  allows for the mirroring of current  $I_1$  as shown in Fig. 2.14. Again in this case the output is obtained at the high impedance node formed by transistors  $M_4$  and  $M_{10}$ .

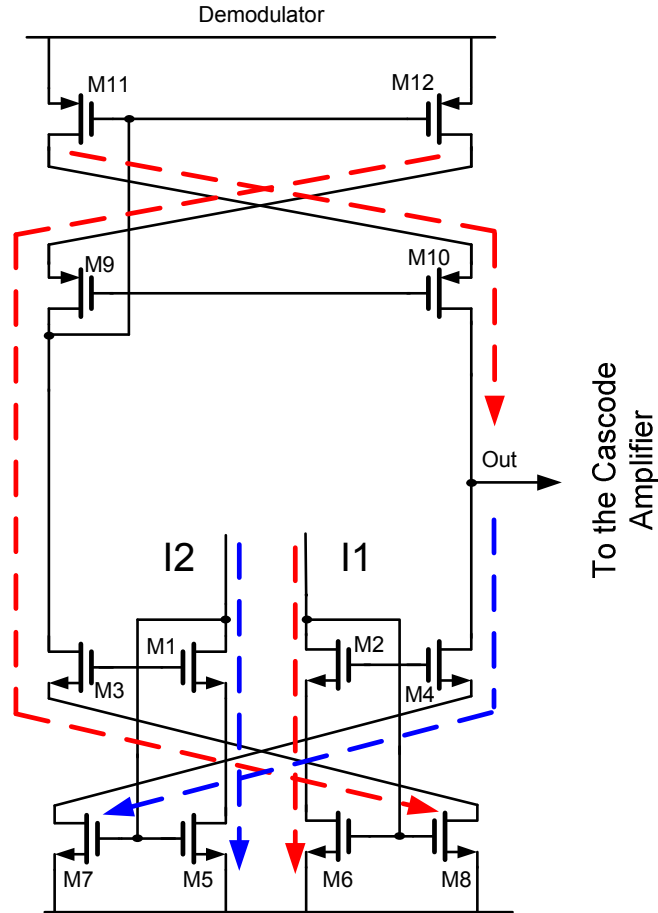


Fig. 2.14 The schematics of the chopper stabilized DDA-INA, for clock P1 “LOW” and clock P2 “High”.

The feedback design uses complementary MOS switches to realize a selective feedback network to tune the amplifier’s closed-loop gain. The switches are driven using a control signal corresponding to a particular bio-signal, thus enabling the circuit to achieve two different gains. As the switch is complementary, we use complementary control signals of 2V and 0V to turn on the NMOS switch and the PMOS switch, respectively. With the present configuration we can achieve amplifier gains of 40 dB (100 times) for the EEG signal and 20 dB (10 times) for the ECG signal. This is done by keeping in mind that the signal voltage range for the EEG signal is  $1\mu\text{V} - 100\mu\text{V}$ , and for the ECG signal is  $80\mu\text{V} - 8\text{mV}$  [47]. As resistors are prone to mismatches, the Differential Difference Amplifier (DDA) topology has been

used along with the feedback network to ensure that the amplifier gain is dependent only on the resistor ratio, thus reducing the effects of mismatches due to process variation. The selective feedback arrangement is shown in Fig. 2.15.

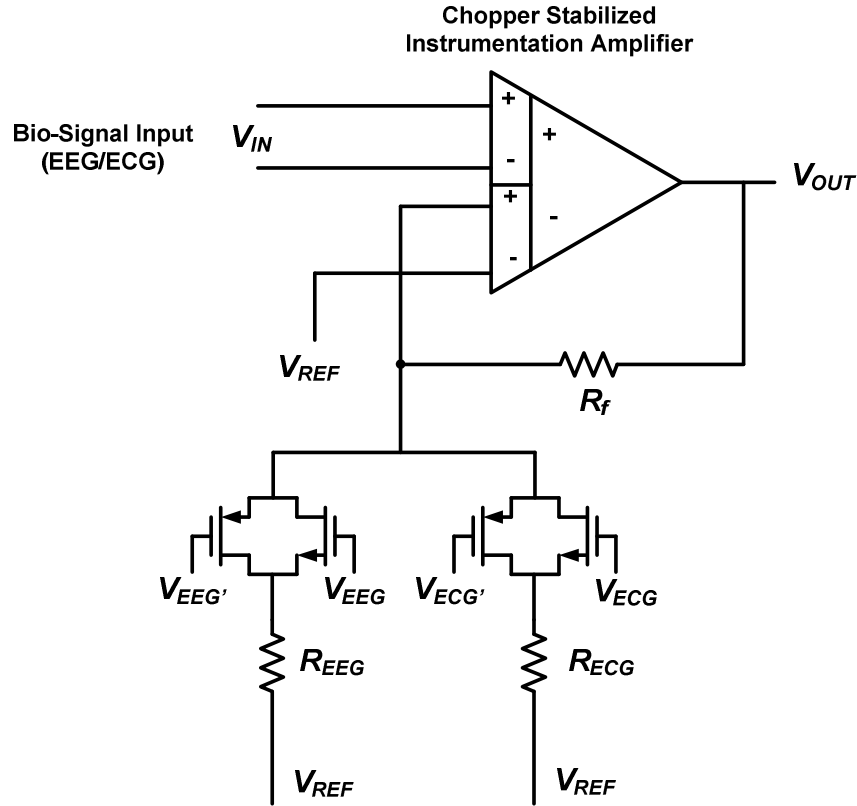


Fig. 2.15 Selective feedback arrangement used for gain selection.

When a high-low is applied as the control signals  $V_{EEG}-V_{EEG}'$ , the amplifier gain is given as:

$$Gain_{EEG} = 20\log\left[\frac{R_f + R_{EEG}}{R_{EEG}}\right] = 20\log\left[\frac{10M + 83.33k}{83.33k}\right] \approx 40dB$$

Similarly, when a low-high is applied as the control signals  $V_{EEG}-V_{EEG}'$ , the amplifier gain is given as:

$$Gain_{ECG} = 20\log\left[\frac{R_f + R_{ECG}}{R_{ECG}}\right] = 20\log\left[\frac{10M + 833.33k}{833.33k}\right] \approx 20dB.$$

For the chopper stabilization to be realized, one of the most essential blocks is the non-overlapping clock generator. This block utilizes a reference clock signal for generating the two non-overlapping clock signals shown before, P1 and P2. This essentially implies that the two clock signals are out of phase with respect to each other, and also may have unequal pulse widths. The non-overlapping clocks generated here should be of the same period, as this period is typically decided by the reference clock signal. An illustration of the non-overlapping clocks is shown in Fig. 2.16.

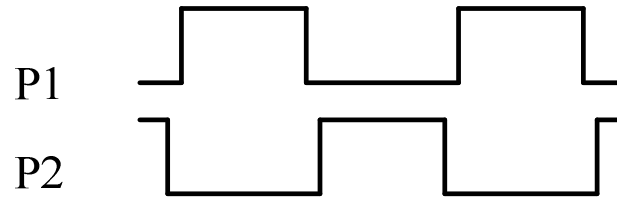


Fig. 2.16 An example of non-overlapping clock signals.

The clock generator is designed using 2 NOR gates that generate the non-overlapping clocks, as shown in Fig. 2.17 [62]. The reference clock is fed to one of the NOR gates directly, and inverted and fed to the other NOR gate. Inverters in the feedback loop act as delay blocks and add the delay between the non-overlapping clocks. The buffer stage at the output of the NOR gates are essentially made up of inverters and are used to drive the subsequent stages. Increasing the number of inverters in the feedback loop produces a larger non-overlapping delay. Non-overlapping delay is vital to ensure that all the switches of the chopper switch are not operational at all time. The delay of 40ns was realized by using 16 inverter stages. A ratio of 2 was maintained for the  $\left(\frac{W}{L}\right)_{PMOS}$  to  $\left(\frac{W}{L}\right)_{NMOS}$  ratio of each inverter stage.

The channel length of the devices is the most crucial factor for introducing delay, and for the present design a channel length of  $L = 4 \mu\text{m}$  was used.

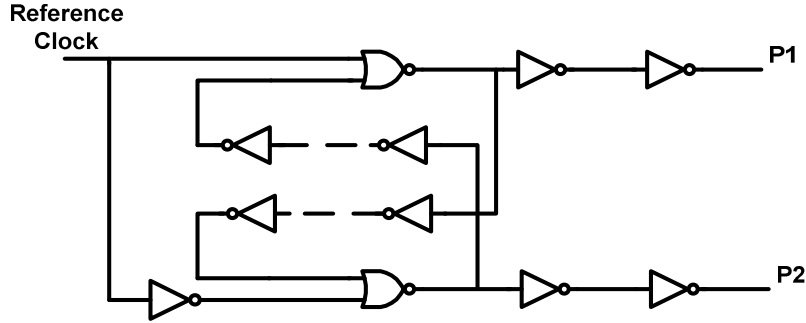


Fig. 2.17 The non-overlapping clock generator. [62]

### 2.3.4 DDA-based chopper stabilized INA – Simulation

The noise response (linear) of the DDA-based INA without chopper stabilization is shown in Fig. 2.18. The corner frequency was ascertained to be close to 12.5 kHz. The spot noise at 10Hz was recorded as  $4.62\mu\text{V}/\sqrt{\text{Hz}}$ .

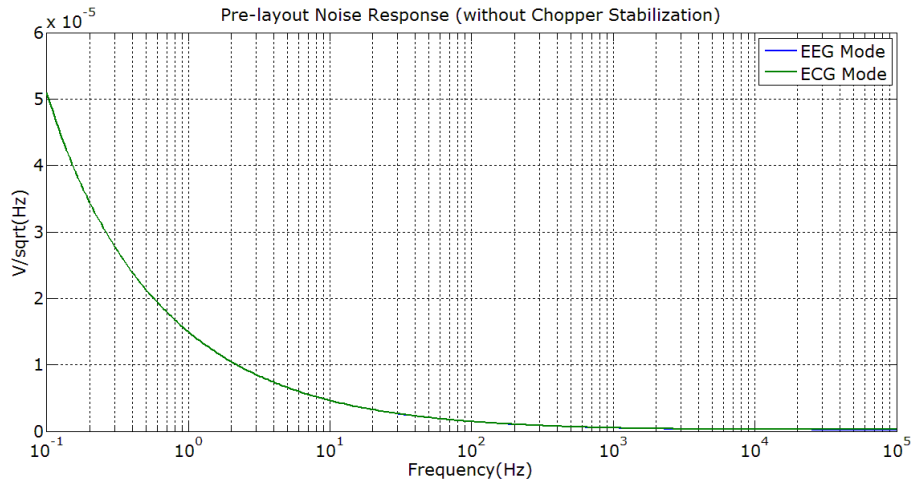


Fig. 2.18 Noise response for EEG and ECG mode without chopper stabilization.

Table.2.3 Noise Response (without chopper stabilization)

Mode	Corner Frequency	Noise Floor	Spot Noise @ 10 Hz
EEG	12.5 kHz	240 nV/ $\sqrt{\text{Hz}}$	$4.62\mu\text{V}/\sqrt{\text{Hz}}$
ECG	12.5 kHz	267 nV/ $\sqrt{\text{Hz}}$	$4.62\mu\text{V}/\sqrt{\text{Hz}}$

It is observed that the simulated noise floor of the INA operating in ECG mode is higher than that of EEG mode by almost  $25\text{nV}/\sqrt{\text{Hz}}$ .

Periodic Noise (PNoise) simulation was used to obtain the noise response of the instrumentation amplifier, where the simulation was set-up for sweep of a frequency range of 100 mHz to 100 kHz with 10points/decade resolution. The maximum sidebands to be analyzed were set as 1. It was observed that the flicker noise pole was transposed to the chopper frequency ( $f_{chop}$ ) of 5kHz. The plot is shown in Fig. 2.19.

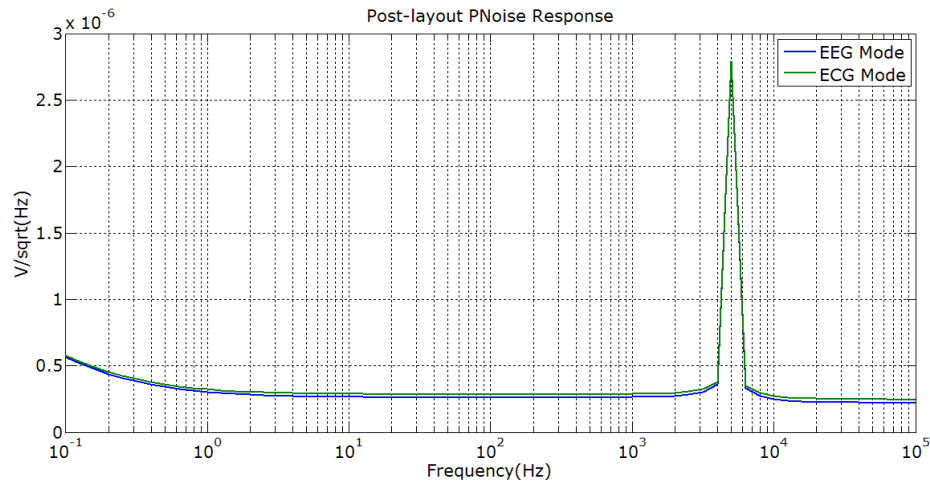


Fig. 2.19 Post-layout noise response for EEG and ECG mode.

#### 2.4 Noise Response (with chopper stabilization)

Mode	Spot Noise @ 10Hz	Integrated Input-referred Noise [0.1 Hz -300 Hz]
EEG	265 nV/ $\sqrt{\text{Hz}}$	4.53 $\mu\text{V}_{\text{rms}}$
ECG	288.5 nV/ $\sqrt{\text{Hz}}$	4.93 $\mu\text{V}_{\text{rms}}$

The frequency response plot obtained using PAC simulation is shown in Fig.2.20. The dc gain for the EEG mode was obtained as 40.8 dB and the amplifier cut-off frequency ( $f_c$ ) recorded as 451.2 Hz. Similarly the dc gain for ECG mode was

obtained as 21.6 dB and the cut-off frequency ( $f_c$ ) recorded as 4.96 kHz.

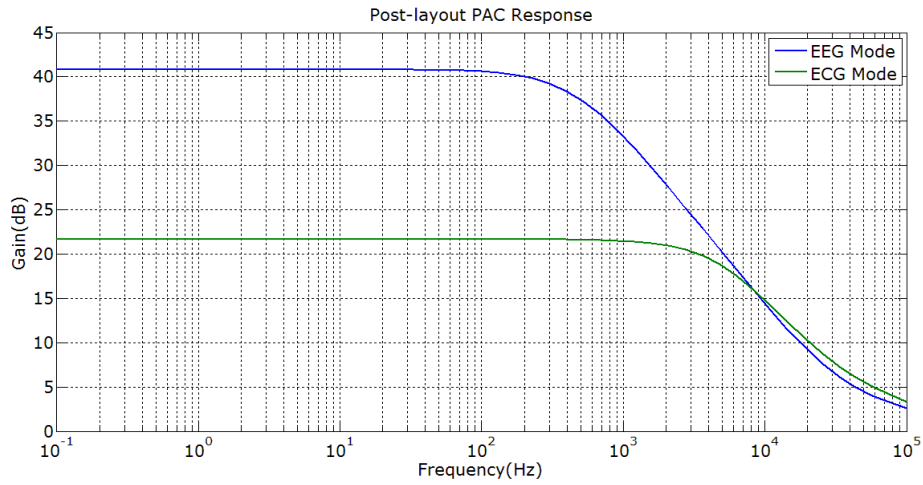


Fig. 2.20 Post-layout simulated INA frequency response for EEG and ECG mode.

Table.2.5 Simulated INA Frequency Response (with chopper stabilization)

Mode	dc Gain (100mHz – 150Hz)	3-dB Cut-off
EEG	40.8 dB	451.2 Hz
ECG	21.6 dB	4.96 kHz

Common centroid scheme was used for all differential pair stages and the connected active loads to ensure reduction of mismatches and enhance CMRR. All capacitors were provided guard-rings to improve noise isolation. Resistors are prone to mismatches and variations and hence it was ensured that the resistors of the feedback network were having proper symmetry. High degree of symmetry was maintained for all the differential signals and clock signals. Banks of decoupling capacitors were provided for *Vdd\_chopper*, *Vdd\_buffer* and *Vref* signals, and these capacitors help in bypassing the spurious high frequency signals of the supply rails and also help in providing the extra boost of current required during transition and switching. The connections to the bond-pads were provided with enough vias, ensuring adequate current handling characteristic. For testing the high pass filter with external resistances, two additional bond-pads were used. The chip-size with bond-pads was 1.26mm × 0.86 mm.

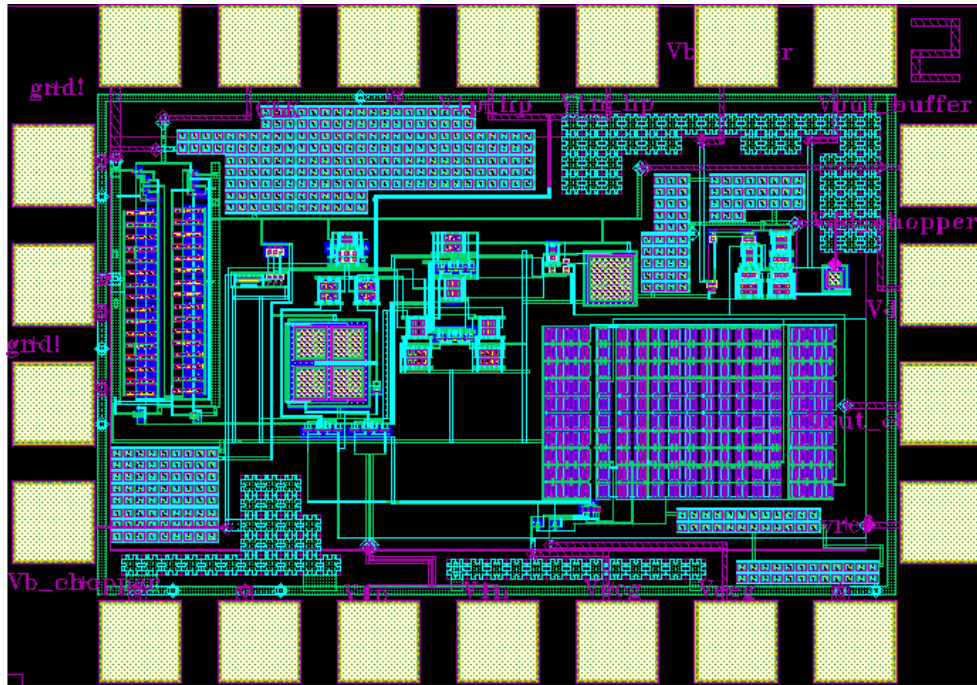


Fig. 2.21 Layout of the DDA-based INA

### 2.3.5 Achieved specifications by simulation

The design DDA-based chopper stabilized INA achieved an input referred noise of  $4.93 \mu\text{V}_{\text{rms}}$  for a bandwidth of 0.1Hz – 300Hz, with a supply voltage of 2V and current of  $1 \mu\text{A}$ . Since the voltage levels of ECG signals lie in the range of 0.5mV – 4 mV, this low-noise, low-power DDA-based INA should be able to sense the cardiac biosignals. But in order to realize an INA which can also sense EEG, better noise performance is required. Table 2.6 compares the achieved specifications with the targeted specifications.

Table.2.6 Achieved Specification by Simulation (with chopper stabilization)

Parameter	Targeted Specification	Achieved Specification
Supply Voltage	2 V	2 V
Supply Current	$< 2 \mu\text{A}$	$1 \mu\text{A}$
Open-loop dc Gain	$> 120 \text{ dB}$	$> 110 \text{ dB}$
Closed-loop dc Gain for EEG Mode	40 dB	40.8 dB
Closed-loop dc Gain for ECG Mode	20 dB	21.6 dB
CMRR	$> 80 \text{ dB}$	$> 110 \text{ dB}$
PSRR	$> 60 \text{ dB}$	$> 60 \text{ dB}$
Input Referred Noise (EEG)	$< 2 \mu\text{V}_{\text{rms}}$	$4.53 \mu\text{V}_{\text{rms}}$
Noise PSD (EEG)	$< 100 \text{ nV}/\sqrt{\text{Hz}} @ 10 \text{ Hz}$	$265 \text{ nV}/\sqrt{\text{Hz}} @ 10 \text{ Hz}$
Input Referred Noise (ECG)	$< 2 \mu\text{V}_{\text{rms}}$	$4.93 \mu\text{V}_{\text{rms}}$
Noise PSD (ECG)	$< 100 \text{ nV}/\sqrt{\text{Hz}} @ 10 \text{ Hz}$	$288.5 \text{ nV}/\sqrt{\text{Hz}} @ 10 \text{ Hz}$

### 2.3.6 Noise Efficiency Factor (NEF)

Achieving low-noise performance with strict power requirement is the primary goal for the chopper stabilized instrumentation amplifier designed for bio-signal acquisition. In this regard the trade-off between power consumed and noise exhibited has to be considered. A figure of merit known as Noise Efficiency Factor (NEF) evaluates this trade-off and provides insight into the performance of the design [50], [63]. The expression for NEF is given as, [63]

$$NEF = Vni_{rms} \left[ \frac{2I_{dc}}{\pi \times V_T \times 4kT \times BW} \right]^{0.5} \quad (2.12)$$

where  $Vni_{rms}$  is the integrated input-referred noise (IRN),  $I_{dc}$  is the quiescent current of the amplifier,  $V_T$  is the thermal voltage,  $BW$  is the 3-dB frequency bandwidth of the amplifier,  $k$  is the Boltzmann's constant and  $T$  is the absolute temperature. An amplifier using a single BJT has an NEF of unity and hence forms the reference for all other amplifier circuits [63]. The NEF for an amplifier followed by a low-pass filter, as is the case of chopper stabilized DDA discussed, is expressed as [50]:

$$NEF = Vni_{rms} \left[ \frac{I_{dc}}{1.22 \times V_T \times 4kT \times BW} \right]^{0.5} \quad (2.13)$$

Considering the ECG mode of operation, the simulated integrated noise for [0.1-300Hz] = 4.93  $\mu$ Vrms and the bias current of 1 $\mu$ A with a bandwidth of 250 Hz obtained after the subsequent filtering stage [50], using equation 2.13 we get an NEF of 13.6

$$NEF = 4.93 \mu V_{rms} \left[ \frac{1 \mu A}{1.22 \times 26 mV \times 4 \times 1.38 \times 10^{-23} \times 300 \times 250} \right]^{0.5} = 13.6 \quad (2.14)$$

### 2.3.7 State-of-the-art performance comparison

The performance of different low-noise and low-power instrumentation amplifier designs applied to different types of bio-signals are compared, as shown in Table 2.7.

Table 2.7 State-of-the-art performance comparison.

	W'panitch et.al [2007] [53]	Qian et.al [2011] [64]	Wu et.al [2009] [65]	Denison et.al [2007] [50]	Fan et.al [2011] [54]	Guo et.al [2012] [57]	This Work (Simulated)
<b>Current</b>	2.7 $\mu\text{A}$	0.872 $\mu\text{A}$	230 $\mu\text{A}$	1 $\mu\text{A}$	1 $\mu\text{A}$	22.4 $\mu\text{A}$	1 $\mu\text{A}$
<b>Power</b>	7.6 $\mu\text{W}$	2.4 $\mu\text{W}$	1 mW	2 $\mu\text{W}$	1.8 $\mu\text{W}$	73.9 $\mu\text{W}$	2 $\mu\text{W}$
<b>Gain</b>	40.85 dB	39.4 dB	40 dB	40 dB	40 dB	26 dB	41.4 dB / 22 dB
<b>Bandwidth</b>	45 Hz – 5.32 kHz	0.36 Hz – 1.3 kHz	800 kHz	1 kHz	-	30 kHz	5.5 kHz / 550 Hz
<b>IRN voltage</b>	3.06 $\mu\text{Vrms}$ [10 Hz -98 kHz]	3.07 $\mu\text{Vrms}$ [0.5 Hz - 30 kHz]	-	1.3 $\mu\text{Vrms}$ [0.05 Hz -4 kHz]	6.7 $\mu\text{Vrms}$ [0.5 Hz - 100Hz]	0.9 $\mu\text{Vrms}$ [1 Hz - 200Hz]	4.93 $\mu\text{Vrms}$ [0.1 Hz - 300Hz]
<b>1/f noise corner</b>	-	50 Hz	1 mHz	3 Hz	100 mHz	23 Hz	50 Hz
<b>Noise PSD</b>	31 nV/ $\sqrt{\text{Hz}}$	60 nV/ $\sqrt{\text{Hz}}$	15 nV/ $\sqrt{\text{Hz}}$	94 nV/ $\sqrt{\text{Hz}}$	60 nV/ $\sqrt{\text{Hz}}$	32.9 nV/ $\sqrt{\text{Hz}}$	288.5 nV/ $\sqrt{\text{Hz}}$
<b>NEF</b>	2.67	3.09	8.8	4.6	3.3	4.5	13.6
<b>CMRR</b>	> 66 dB	> 66 dB	> 120 dB	100 dB	134 dB	> 110 dB	>66 dB
<b>Chopping Frequency</b>	-	-	40 kHz, 510 Khz	4 kHz	5 kHz	10 kHz	5 kHz
<b>Process</b>	0.5 $\mu\text{m}$ CMOS	0.6 $\mu\text{m}$ CMOS	0.7 $\mu\text{m}$ CMOS	0.8 $\mu\text{m}$ CMOS	65 nm CMOS	0.35 $\mu\text{m}$ CMOS	0.35 $\mu\text{m}$ CMOS

As can be observed from Table 2.7, the present work does not exhibit a commendable NEF and in order to improve the NEF there are primarily only two parameters which can be manipulated, as the rest of the parameters are either scientific constants or system requirements. The two parameters which we can try to reduce are  $Vni_{rms}$  and  $I_{dc}$ . As for the present design  $I_{dc}$  used is  $1\mu A$ , which already is very low, it is only  $Vni_{rms}$  which can be reduced to achieve a better NEF.

Reduction of  $Vni_{rms}$  (which is the integrated input-referred noise) requires implementing specific low-noise strategies on the circuit level as well as system level. The significant noise contributors on the circuit level are the differential input pair and active loads. Source degeneration is an effective and recommended method of reducing the noise originating from the load devices [50], [53], [64]. As the transconductance of the amplifier is dominated by the transconductance of the input pair, therefore techniques for increasing it for the same bias condition should be tried. Additionally, using large PMOS device help reduce the flicker noise contribution [61]

As per the noise analysis in [56], there is a definite relation between the amplifier cut-off frequency, amplifier noise corner frequency and the chopper frequency which guarantees an optimum performance. To minimize the flicker noise contribution, ideally the chopper frequency must be larger than the amplifier corner frequency; but since a higher chopper frequency results in undesirable higher residual offset, a good compromise is obtained by opting for a chopper frequency to be equal to noise corner frequency [56], [59]. In the present design the corner frequency of the amplifier is 12.5 kHz, using such a high chopper frequency will result in residual offsets. If possible the noise corner frequency of the amplifier must be reduced, which in turn will entail the use of a lower chopper frequency. Lower chopper frequency not only implies lower residual offsets, but it also enables a lower-power design as the bandwidth requirement of the amplifier is relaxed.

## 2.4 Low-noise design paradigm

It was observed in the DDA-based INA design, the application of chopper stabilization technique translated the flicker noise pole to the chopping frequency, and thus suppressing flicker noise at low-frequency where most of the biosignal information resides. But as seen in Table 2.7, the IRN and NEF of the amplifier were not as good as other published works and would make sensing of low amplitude biosignals very difficult. In order to have a single biosignal amplifier capable of sensing ECG as well as low amplitude and sensitive signals like EEG, we at Dr. Lie's lab implemented another amplifier design equipped with dedicated low-noise strategy at the circuit-level in conjunction with chopper-stabilization technique at the system level. As mentioned before, to achieve better noise performance the integrated input referred noise has to be reduced. This noise is comprised of the thermal noise and flicker noise component and is predominantly contributed by the differential input pair and the active loads used in the output branch of the amplifier. The noise of single MOSFET device is described in terms of input-mean-square voltage noise and can be modeled as [61],

$$e_{ni}^2 = \left[ \frac{4kT\gamma(1+\eta)}{g_m} + \frac{K_f}{2WLC_{ox}f\beta} \right] \Delta f \quad (\text{V}^2) \quad (2.15)$$

where,  $\Delta f$  = a small bandwidth typically 1Hz

$g_m$  = small signal transconductance from gate-to-channel

$\eta$  =  $g_{mbs}/g_m$

$k$  = Boltzmann's constant

$\gamma$  = noise fitting constant

$T$  = temperature in Kelvin

$K_f$  = flicker noise coefficient

$\beta$  = device constant

Application of chopper stabilization moves the flicker noise component in equation (2.15), to the modulating frequency and what remains at baseband is the thermal noise. Low-noise circuit strategies are required to reduce this thermal noise, which can be expressed as ,

$$e_{ni\_thermal}^2 = \frac{4kT\gamma(1+\eta)}{g_m} \Delta f \quad (\text{V}^2) \quad (2.16)$$

The output noise contributed by the input differential pair of a typical amplifier can be given as,

$$e_{diff\_thermal}^2 = 2r_o^2 g_{m1}^2 e_{ni\_thermal}^2 \quad (\text{V}^2) \quad (2.17)$$

where the small-signal transconductance of the two devices of the input pair is considered to be equal to  $g_{m1}$ , the output resistance of the input pair is  $r_o$  and the thermal noise contribution of each of the devices is  $e_{ni\_thermal}$ . Similarly the noise contributed by the active-load devices of typical differential amplifier can be given as,

$$e_{load\_thermal}^2 = 2r_o^2 g_{m3}^2 e_{ni\_load\_thermal}^2 \quad (\text{V}^2) \quad (2.18)$$

where the small-signal transconductance of the active-load devices is considered to be equal to  $g_{m3}$ , the output resistance of the active load device is  $r_o$  and the thermal noise contribution of each of the devices is  $e_{ni\_load\_thermal}$ .

The total output noise of the typical amplifier can be expressed as,

$$e_{total\_thermal}^2 = e_{diff\_thermal}^2 + e_{load\_thermal}^2 \quad (2.19)$$

Therefore, the input-referred noise for the amplifier with a small-signal gain of  $g_{m1}r_o$  can be given as,

$$e_{input\_thermal}^2 = \frac{e_{total\_thermal}^2}{g_{m1}^2 r_o^2} = \frac{e_{diff\_thermal}^2 + e_{load\_thermal}^2}{g_{m1}^2 r_o^2} \quad (2.20)$$

$$e_{input\_thermal}^2 = \left[ 2e_{ni\_thermal}^2 + \frac{2g_{m3}^2 e_{ni\_load\_thermal}^2}{g_{m1}^2} \right] \quad (2.21)$$

It can be seen in equation (2.21), that to reduce the thermal noise component the small-signal transconductance,  $g_{m1}$ , of the input pair has to be increased, and the small signal transconductance,  $g_{m3}$ , of the active output loads has to be decreased. Higher transconductance is achieved by applying larger current which implies higher power consumption, and this is the trade-off and is not what is desired. To achieve higher transconductance for the same bias current and also satisfy low-power constraint, MOSFET devices operating in the subthreshold region are utilized [53], [64]. In subthreshold operation the output current and the input voltage of the MOSFET exhibit an exponential relationship similar to bipolar transistors, this exponential relationship results in higher transconductance efficiency [66].

## 2.5 Fully-differential folded-cascode based chopper stabilized INA

Considering the above discussed design paradigm, a chopper-stabilized capacitive feedback fully differential amplifier was implemented. Unlike the previous design, capacitive feedback was opted for this design, since realizing accurate capacitor ratios are relatively easier. Moreover using a capacitive feedback enables gain-setting using capacitor ratio thus reducing errors due to mismatches. The gain of a capacitive feedback amplifier with a finite open-loop gain  $A$  is given in equation (2.22).

$$\frac{V_{out}}{V_{in}} = \frac{C_{in}}{C_{fb} + \frac{C_{in} + C_{p,in} + C_{fb}}{A}} \quad (2.22)$$

where,  $C_{in}$  is the input capacitor of the feedback network,  $C_{fb}$  is the feedback capacitance and  $C_{p,in}$  is the parasitic gate capacitance of the input MOSFET device. For the present design two chopper switches were used with one placed at the input and the other place at the output of the fully differential amplifier. The fully-differential chopper stabilized system was designed using TSMC CMOS 0.18  $\mu\text{m}$  process and was co-designed with Mr. Yen-Ting Liu, who is a Ph.D student under Dr. Lie. The system-level implementation is shown in the Fig. 2.22

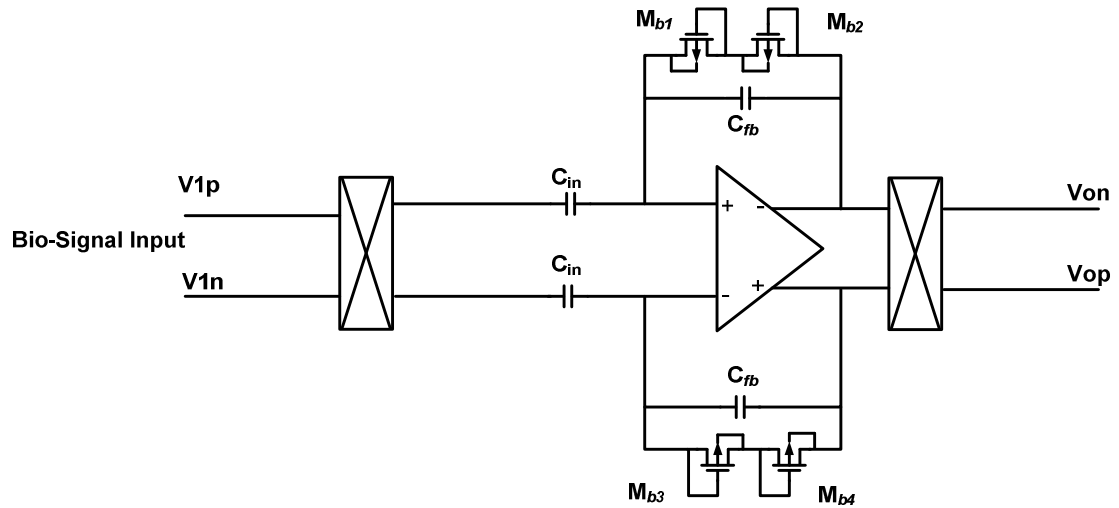


Fig. 2.22 Fully-differential capacitive feedback chopper stabilized INA. [53], [54], [64]

The capacitive feedback system was used for our design shown Fig. 2.22, and was designed to achieve a closed-loop gain of 32 dB. This was realized by using an input capacitor,  $C_{in} = 8\text{pF}$  and a feedback capacitor  $C_{fb} = 0.2\text{pF}$ . Higher gain would require a higher input capacitor or a lower feedback capacitor. Higher input capacitance may lower the input impedance of the OTA due to switch-capacitor effect caused by the input chopper [50]. Furthermore lowering the feedback capacitor may lead to process feasibility issues. Moreover our bio-sensor AFE IC would be equipped with variable gain amplifier (VGA) which can boost the signal whenever required. To provide the feedback dc-point, a high-resistance ( $> 10^{12} \Omega$ ) is required in the feedback

path so as not to load the OTA. This high resistance is realized by using MOS-based pseudo-resistors, as shown in Fig. 2.22 [50], [53], [64].

### **2.5.1 Folded-cascode OTA with current scaling technique**

In this design, the standard folded-cascode topology with the current scaling technique described in [53] was used to implement the operational transconductance amplifier (OTA). The standard folded-cascode topology aids in the application of current-scaling technique and also provides adequate gain in a single-stage to implement a feedback network with minimal gain error, thus making the use of a second-stage unnecessary [53], [64]. Reduction of an amplification stage also helps the power budget. The current-scaling technique requires the devices in the output (folded) branch of the OTA to be biased such that the quiescent current is a fraction of the quiescent current used to bias the input differential pair. Since the quiescent current in the output branch does not contribute to the overall transconductance, reducing them will not affect the amplifier gain. Application of current scaling reduces the quiescent current in the output branch which in turn increases the output resistance of each device. This increase in resistance helps in realizing higher gain using just one amplification stage, thus helping a low-power implementation. The noise contributed by the active devices in the output branch is directly proportional to their respective transconductance, hence reducing the quiescent current through them also helps the low-noise technique. The current scaling technique proposed in [53], [64] reinforces the low-noise and low-power strategy required to realize a robust and sensitive bio-signal amplifier, and has been used in our second design.

The most important component of the design is the folded cascode OTA, Fig.2.23 depicts the circuit implementation of the same. The designs shown in [53] and [64] achieved a current ratio of 1:16 between the quiescent current in the output branch and the input pair device, but as a conservative approach in our design a current ratio of 1:7 was maintained. Higher ratios can provide better noise performance, but also make the nodes ‘X’ and ‘Y’, (in Fig.2.23) a bit more critical, as

the resistance looking into the source of  $M_7$  ( $M_8$ ) and the drains of  $M_1$  ( $M_2$ ) (if cascode device  $M_3$  ( $M_4$ ) is not present) and  $M_5$  ( $M_6$ ) become comparable, inhibiting the flow of small signal current to the output branch. The reduced flow of small-signal current results in lower effective transconductance ( $G_m$ ) of the OTA, which makes the design non-functional. This is overcome by increasing the resistance looking into the drains of input pair by using  $M_3$  and  $M_4$  cascode devices and increasing the resistance looking into the current sink devices,  $M_5$  and  $M_6$  by using source degeneration resistor  $R_1$ . Furthermore importantly, the source degeneration also helps suppress the transconductance of the noise contributing  $M_5$  and  $M_6$ , resulting in lesser noise.

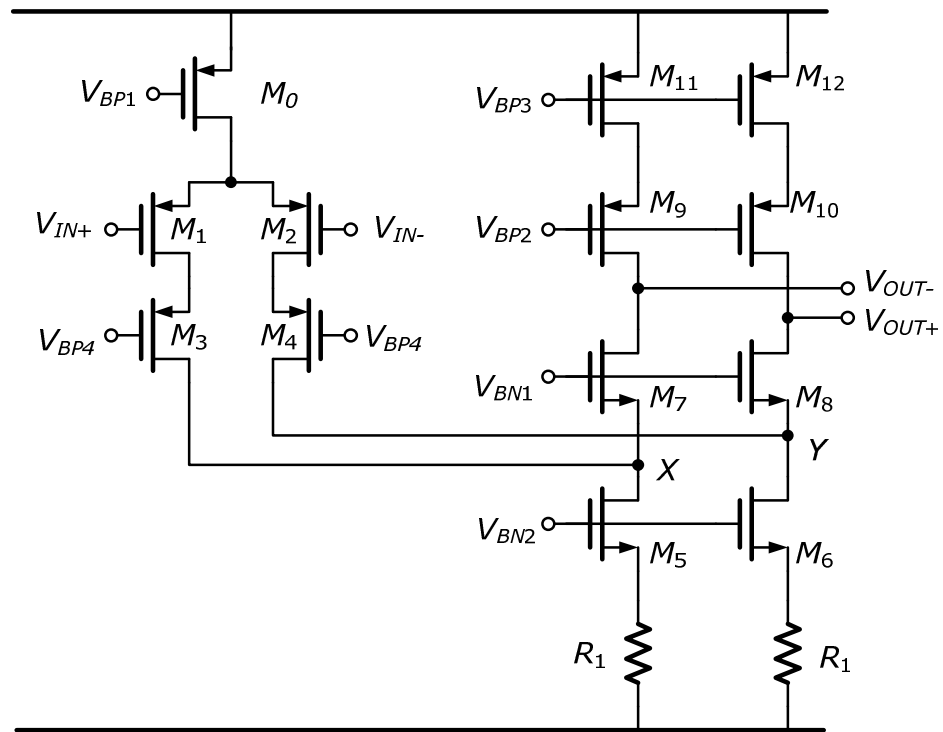


Fig. 2.23 Circuit implementation of the folded-cascode OTA [53].

In order to minimize noise, the other most important requirement is to maximize the effective transconductance ( $G_m$ ) of the amplifier, which typically is the transconductance ( $g_m$ ) of the input pair. For low-power design, a high transconductance can be achieved by capitalizing on the higher transconductance efficiency of MOS devices in weak-inversion region, as shown in Fig. 2.24.

Considering the active load devices, there is a trade-off between low-power and low-noise implementation, as using devices in sub-threshold region requires less power but it enhances transconductance thus increasing noise. For low-noise strategy, we require a high transconductance ( $g_m$ ) of the input pair only, thus as a balancing act, the devices  $M_{11}$  and  $M_{12}$  are operated marginally above threshold region to reduce their noise contribution. Apparently, the current scaling technique has a dominating effect on the transconductance of the output branch devices and thus enabling the design to achieve both low-power as well as low-noise.

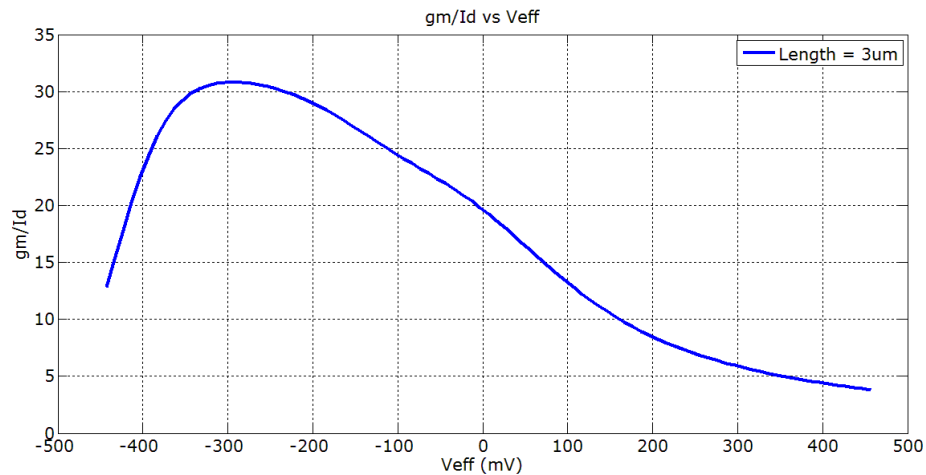


Fig. 2.24 Transconductance efficiency for different operating regions of a typical TSMC n-channel MOSFET of length =  $3 \mu\text{m}$ .

### 2.5.2 Design considerations for current scaling technique

The most critical requirement of the current scaling technique is to be able to maintain the effective transconductance ( $G_m$ ) of the OTA to be equal to the small-signal transconductance of the input differential pair ( $g_m$ ). As mentioned earlier, the current scaling technique results in the attenuation of  $G_m$ , which is detrimental to the functionality of the OTA. Apart from using the cascode devices ( $M_3$  and  $M_4$ ) and source degeneration resistor ( $R_1$ ) to increase the impedance at nodes X and Y, the sizing of the devices connected at nodes X and Y are also critical. Considering the

circuit shown in Fig. 2.23, the effective transconductance ( $G_m$ ) of the OTA can be expressed as [53],

$$G_m = g_m \left( \frac{G_{s7}}{G_{s7} + G_{d5}} \right) \left( \frac{G_{s3} r_{o1}}{1 + G_{s3} r_{o1}} \right) \quad (2.23)$$

where,  $G_{s3}$  is the admittance looking into the source of  $M_3$ ,  $G_{d5}$  is the admittance looking into the drain of  $M_5$  and  $G_{s7}$  is the admittance looking into the source of  $M_7$ .

$\frac{G_{s3} r_{o1}}{1 + G_{s3} r_{o1}}$  is the incremental gain from the input differential pair to the drain of  $M_3$  and

$\frac{G_{s7}}{G_{s7} + G_{d5}}$  is the incremental gain from  $M_3$  and  $M_4$  to the output. The generic

expression for the admittance looking into the source can be derived using the Fig. 2.25 (A) and is expressed as,

$$G_s = \frac{g_{si} + 1/r_{oi}}{1 + Z_L/r_{oi}} \quad (2.24)$$

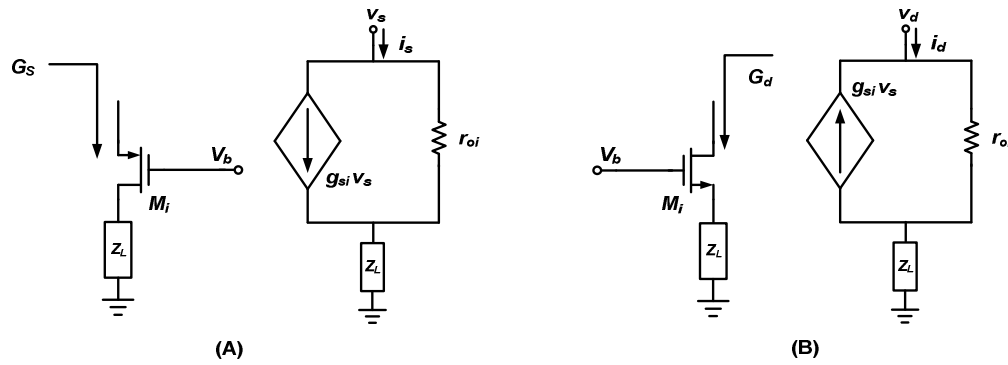


Fig. 2.25 (A) The circuit schematic for source admittance. (B) The circuit schematic for drain admittance. [53]

Similarly, the generic expression for the admittance looking into the drain can be derived using the Fig. 2.25 (B) and is expressed as,

$$G_d = \frac{1}{r_{oi}} \left( \frac{1}{1 + g_{si} Z_L + Z_L / r_{oi}} \right) \quad (2.25)$$

where,  $g_{si}$  is the incremental source admittance and  $r_{oi}$  is the output resistance of  $M_i$ .

Using equation (2.24) and (2.25),  $G_{s3}$ ,  $G_{d5}$  and  $G_{s7}$  can be expressed as [53],

$$G_{s3} = \frac{g_{s3} + 1/r_{o3}}{1 + 1/(r_{o3}(G_{s7} + G_{d5}))} \approx \frac{g_{s3}}{1 + 1/(r_{o3}(G_{s7} + G_{d5}))} \quad (2.26)$$

$$G_{d5} = \frac{1}{r_{o5}} \left( \frac{1}{1 + R_1/r_{o5} + g_{s5} R_1} \right) \quad (2.27)$$

$$G_{s7} = \frac{g_{s7} + 1/r_{o7}}{1 + g_{m9} r_{o9} r_{o11} / g_{s7}} \approx \frac{g_{s7}}{1 + g_{m9} r_{o9} r_{o11} / g_{s7}} \quad (2.28)$$

From equation (2.23) it can be observed that to achieve maximum effective transconductance ( $G_m$ ), the ratio  $G_{s7}/(G_{s7} + G_{d5})$  must be maximized, which can be achieved by making  $G_{d5} \ll G_{s7}$ . To minimize  $G_{d5}$ , as seen in equation (2.27),  $r_{o5}$  was maximized by using longer channel lengths for the  $M_5$  and  $M_6$  devices. Additionally, devices with large  $W/L$  ratio were used for the  $M_5$  and  $M_6$  devices to maximize  $g_{s5}$  thereby reducing  $G_{d5}$ . Also  $g_{s5} R_1 \gg 1$  criterion was applied to minimize  $G_{d5}$  and achieve a value for  $R_1 = 100 \text{ k}\Omega$ . Current scaling is achieved by the proper selection of the  $R_M/R_1$  ratio, where  $R_M$  is the source-degeneration resistor of the current-mirror, shown in Fig. 2.26.

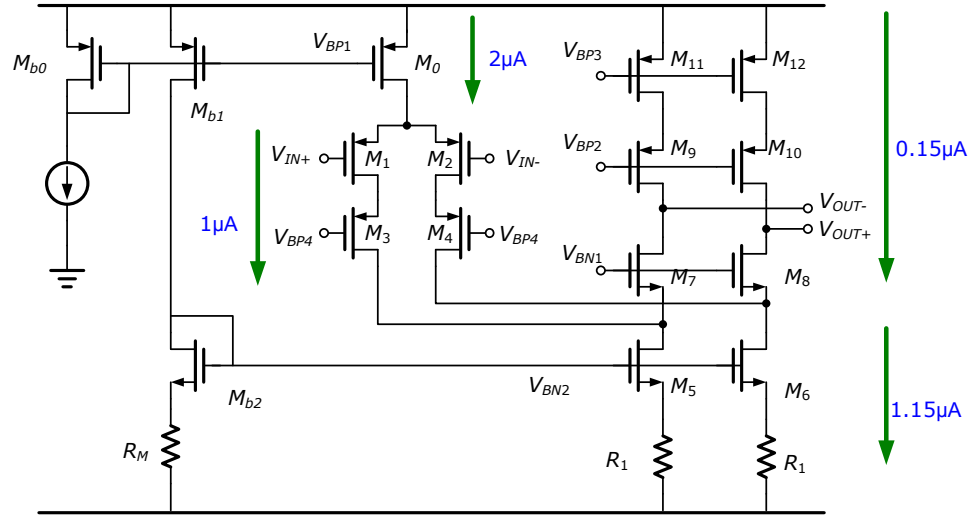


Fig. 2.26 The circuit schematic of the OTA with the current-scaling technique.

### 2.5.3 Device sizing using $g_m/I_D$ method

The discussed design idea and constraints were used together with the  $g_m/I_D$  method to determine the optimum device sizes. The  $g_m/I_D$  method as proposed in [66] is a unified synthesis technique for all regions of operation of the MOSFET. This method is a convenient tool which enables device sizing considering the different operating regions of the device. The look-up tables generated with details regarding  $g_m/I_D$  (transconductance efficiency),  $I_D/W$  (current density) for various over-drive voltages ( $V_{eff}$ ) and various  $V_{DS}$  provide insight into the device operation and also make device sizing very intuitive. All the devices, except M11 and M12 are operating in sub-threshold region, and this was done to achieve a balance between low-noise and low-power implementation. The device sizes are shown in Table 2.8.

Table.2.8 Device sizing

Devices	W/L ( $\mu\text{m}$ )	Operation Region	$g_m/I_D$
M1/M2	156/3	Sub-threshold	21.88
M3/M4	83/3	Sub-threshold	20.38
M5/M6	204/5	Sub-threshold	23.54
M7/M8	4/2	Sub-threshold	22.9
M9/M10	7/1	Sub-threshold	22.35
M11/M12	2.8/2	Above-threshold	15.5



asymptotically for values of  $f_{3dB} \gg f_{chop}$ , and results in the chopper modulated white noise to be almost equal to the original white noise [56]. A higher value of  $f_{3dB}$  compared to  $f_{chop}$  also ensures that the amplifier provides stable gain for the signal in the intermediate stage which as a result of chopping will be at a much higher frequency than the original input signal. The chopper stabilization has been implemented as per the topology presented in [59], wherein we have provided an input chopper and an output chopper at the input and output of the OTA.

### 2.5.5 Switch-capacitor-based common-mode feedback circuit

For a fully-differential OTA design it is mandatory to have a common-mode feedback (CMFB) circuit. This circuit ensures that output DC point is stable and is properly set to bias all the transistors in active region. CMFB circuit also aids in maximizing the output swing by maintaining the desired output DC point. In our present design a switch-capacitor based CMFB circuit was used [67]. This circuit was designed by Mr. Yen-Ting Liu. The main reasons for opting for such an implementation were simplicity, higher linearity, and negligible effect on the output swing. The switch-capacitor based CMFB circuit, as shown in Fig. 2.28, is made up of six MOSFET switches ( $S_1$ - $S_6$ ) and four capacitors. The switches are controlled by non-overlapping clocks  $\Phi_1$  and  $\Phi_2$ .

As seen in Fig. 2.28, the network of the capacitors  $C_1$  and  $C_2$  along with the switches senses the common-mode signal ( $V_{oc}$ ) of the OTA, and subtracts it from the desired common-mode voltage ( $V_{cm}$ ). Voltage  $V_{bp3}$  is the reference gate bias voltage (1.35V) applied to the PMOS loads  $M_{11}$  and  $M_{12}$ , as seen in Fig. 2.25. If the output common mode voltage is steady at 0.9V,  $V_{bp3}$  is set to 1.35V.  $V_{cmfb}$  is the corrected bias voltage that is applied when there is a change in  $V_{oc}$ . When  $\Phi_1$  is high (on),  $C_1$  charges to  $V_{cm} - V_{bp3}$ . When  $\Phi_2$  is high (on),  $C_2$  senses this difference and adjusts  $V_{cmfb}$  accordingly.

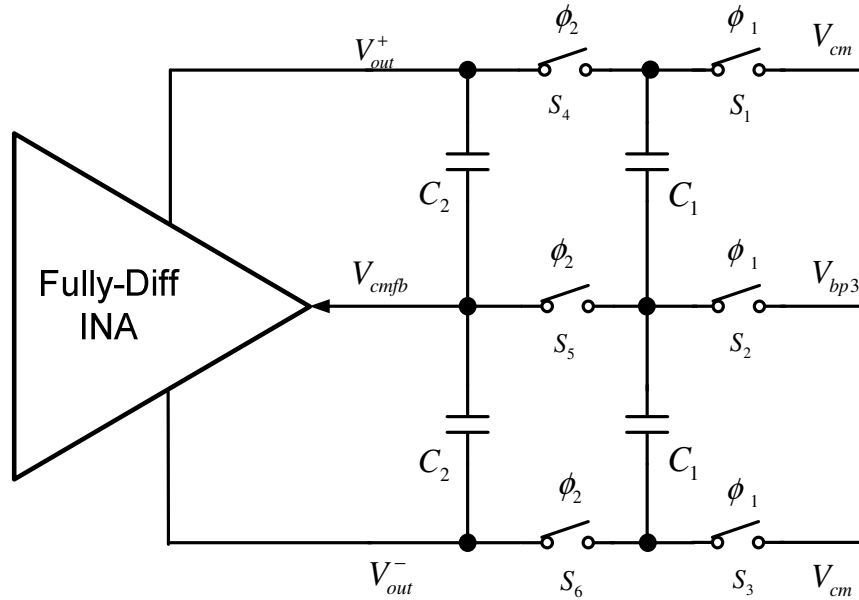


Fig. 2.28 Switch-capacitor based CMFB [67]

The switch-capacitor based CMFB can be analyzed using the state of the switch-capacitive network for the two exclusive clock phases shown in Fig. 2.29. Considering the half circuit of the CMFB, and assuming  $\Delta V = V_{cm} - V_{bp3}$ , and  $\Delta V + \Delta x = V_{out} - V_{cmfb}$ , where  $\Delta x$  is the deviation from the desired common-mode voltage, the charge across  $C_1$  and  $C_2$  for the clock phase  $\phi_1$  can be expressed as,

$$Q(\phi_1) = C_1 \Delta V + C_2 (\Delta V + \Delta x) \tag{2.29}$$

Similarly, for the clock phase  $\phi_2$ , the charge across  $C_1$  and  $C_2$  can be expressed as

$$Q(\phi_2) = (C_1 + C_2) V_x \tag{2.30}$$

Where  $V_x = V_{out} - V_{cmfb}$  for  $\phi_2$ , and since  $V_{cmfb}$  is floating  $V_x$  is unknown. Applying conservation of charges to equation (2.29) and (2.30) we get,

$$V_x = \Delta V + \frac{C_2}{C_1 + C_2} \Delta x \tag{2.31}$$

As can be seen from equation (2.31), for every clock cycle the switch-capacitor based CMFB brings output dc point closer to the common-mode voltage, thus stabilizing the fully-differential OTA's output dc-point.

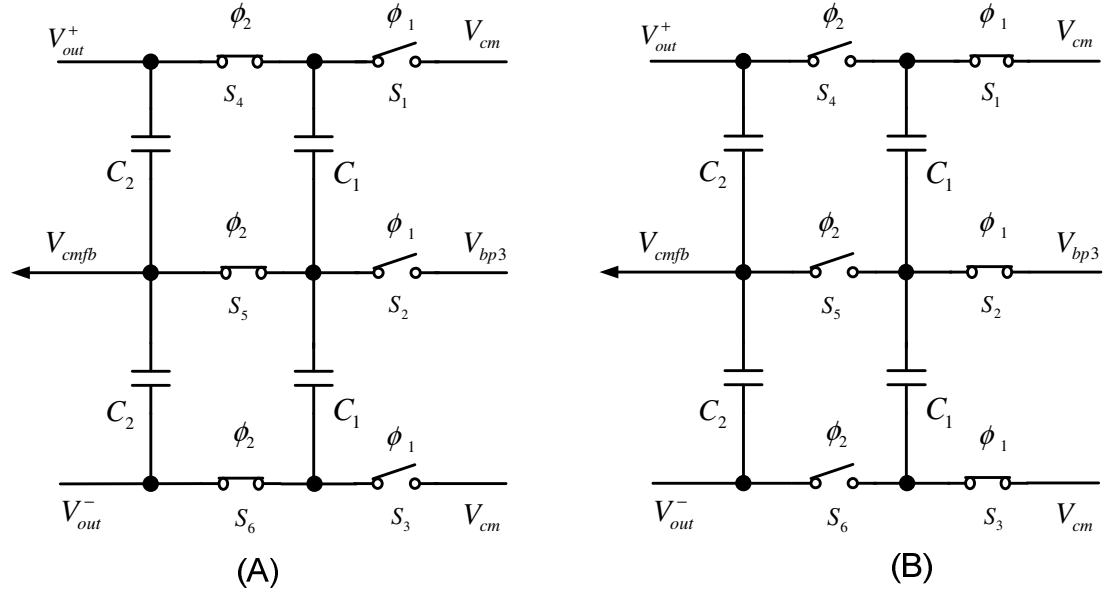


Fig. 2.29 (A) For clock phase  $\phi_2$ . (B) For clock phase  $\phi_1$

### 2.5.6 Fully-differential chopper-stabilized INA - simulation

The fully-differential folded-cascode OTA, which is the core of the chopper-stabilized INA, was simulated to verify the open-loop dc-gain, the phase-margin, the CMRR and the PSRR. The simulated dc-gain and phase response is shown in Fig. 2.30 and the simulated CMRR response of the folded-cascode OTA with a 5% length mismatch in the input pair devices is shown in Fig. 2.31.

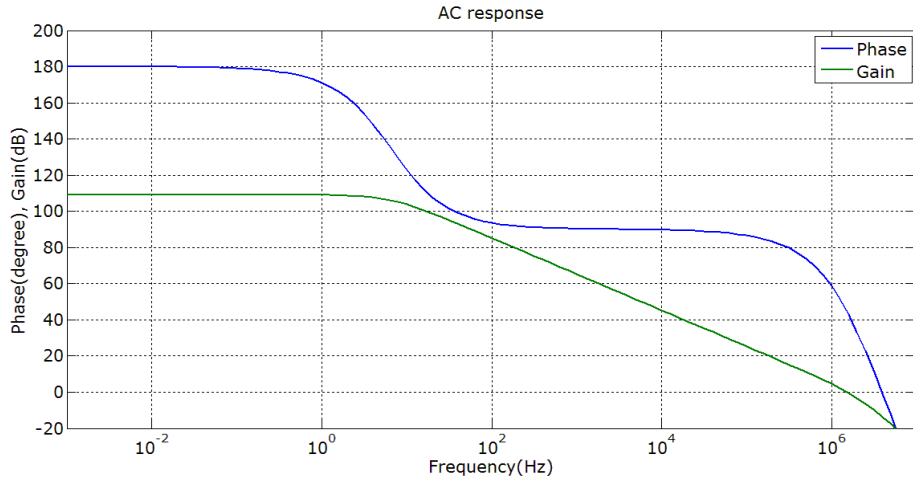


Fig. 2.30 Open-loop dc-gain and phase-response of the folded-cascode OTA.

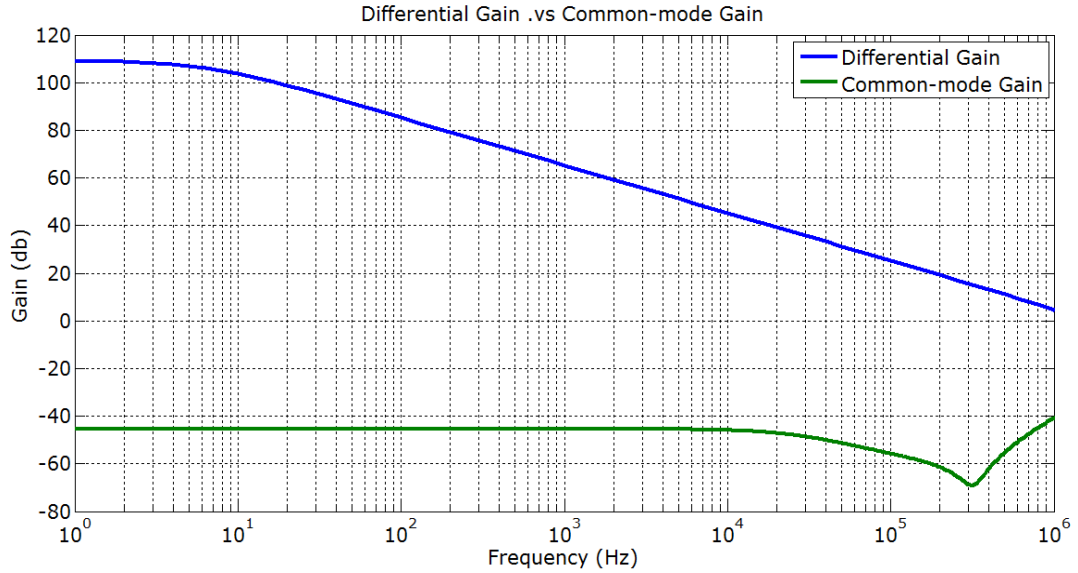


Fig. 2.31 CMRR response simulation of the OTA with input pair length mismatches

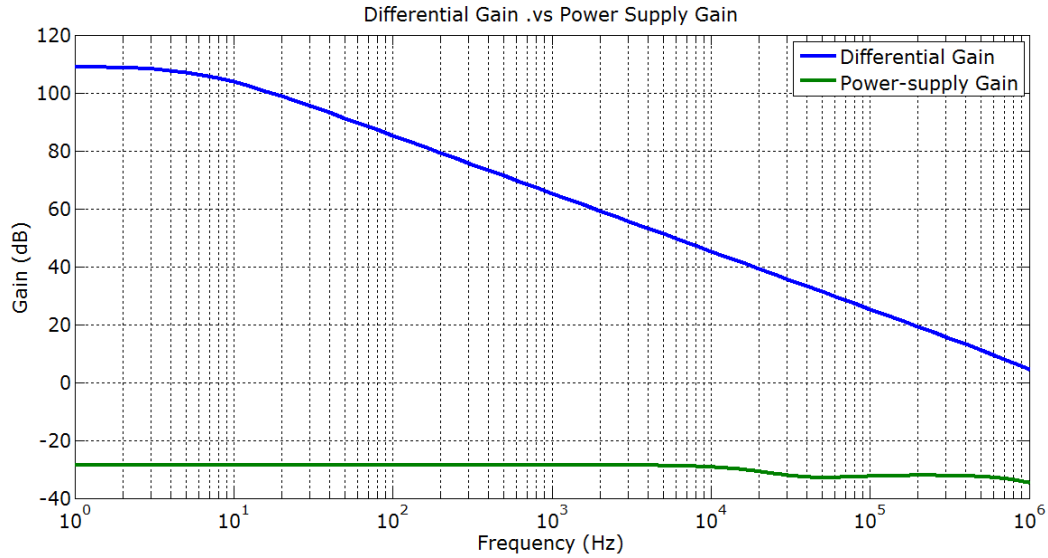


Fig. 2.32 PSRR response simulation of the OTA with input pair length mismatches

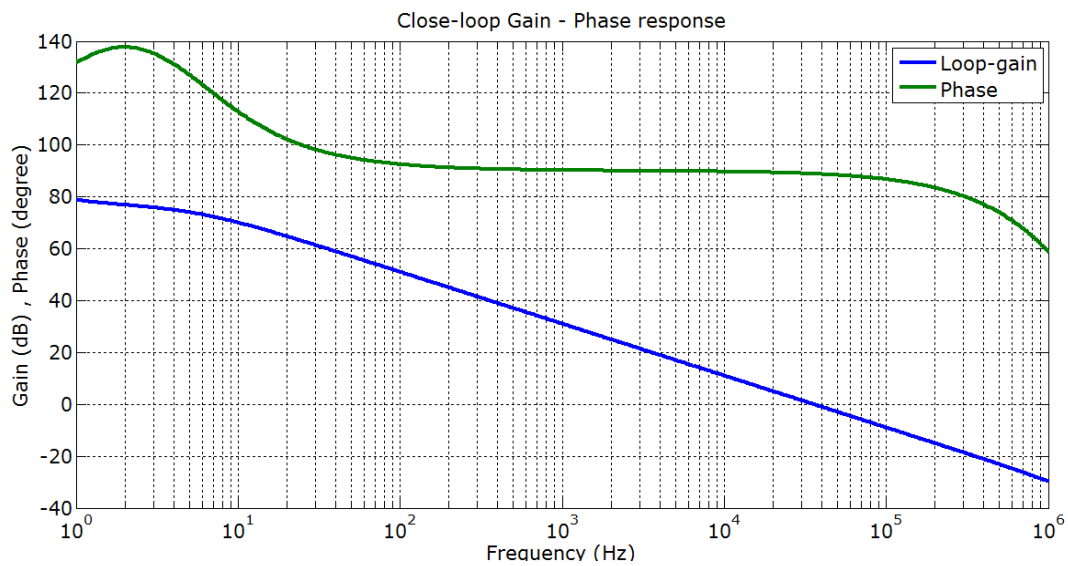


Fig. 2.33 Loop Stability response for the capacitive feedback OTA.

As is observed from Fig. 2.30, the open-loop dc-gain of close to 110 dB is obtained, and this is from a single-stage of OTA. Such a high gain was realized due to the application of current-scaling technique and this makes the circuit suitable for feedback configuration as it helps in reduction of gain error. Furthermore, a single-

stage implementation ensures low-power consumption. A CMRR of  $> 120$  dB was obtained for simulation with channel length mismatch of the input pair devices.

Noise simulation of the instrumentation amplifier without the use of chopper stabilization is also shown to highlight the effectiveness of chopper stabilization as an elegant method of noise reduction. The post-layout simulations shown here are only for the case of capacitive (C-only) extraction. The noise simulation response of the INA without chopper stabilization has been shown in Fig. 2.34 and Fig. 2.35, both in linear and logarithmic scales. The logarithmic scale helps in ascertaining the  $1/f$  noise corner frequency, which is around 1 kHz for the present design. The periodic noise simulation was used to verify the chopper stabilized INA and the response is shown in Fig. 2.36. The flicker noise pole can be seen to be transposed to the chopper frequency, which for the present system is 1 kHz. The noise response has been summarized in Table 2.9.

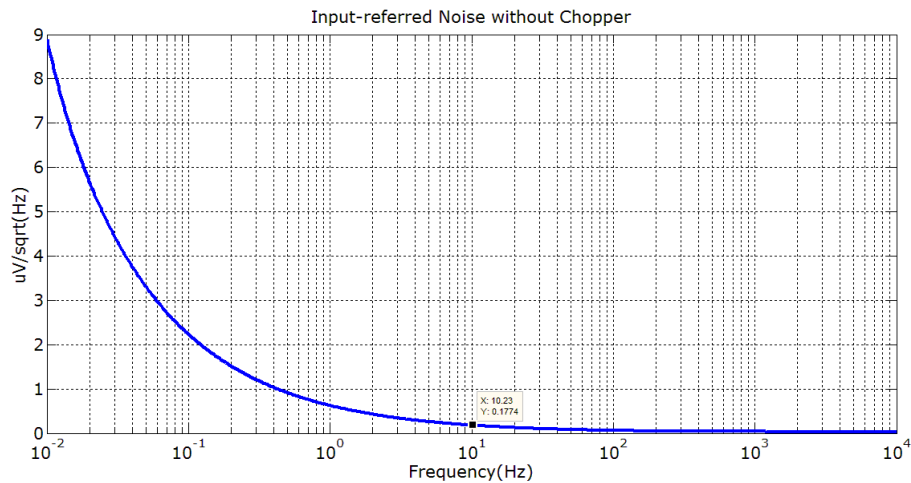


Fig. 2.34 Noise simulation response without chopper showing the spot noise @ 10Hz

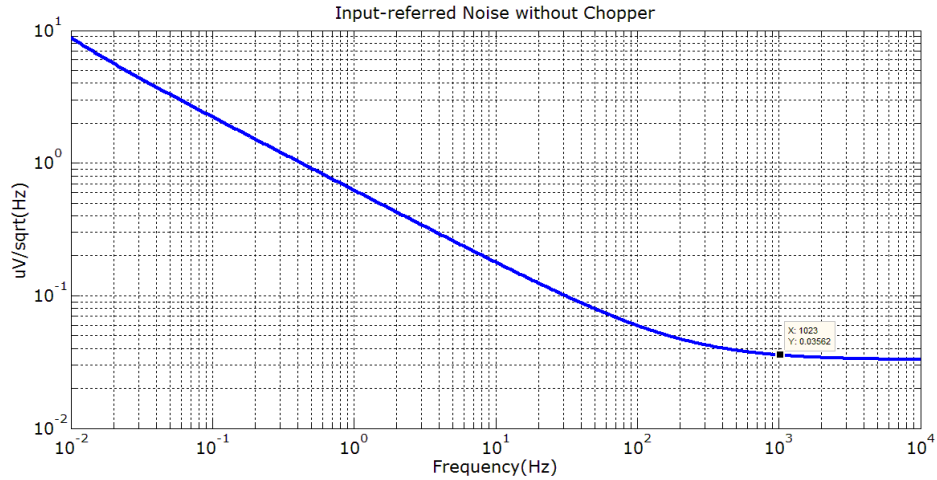


Fig. 2.35 Noise simulation response (log) without chopper showing the  $1/f$  noise corner @ 1 kHz.

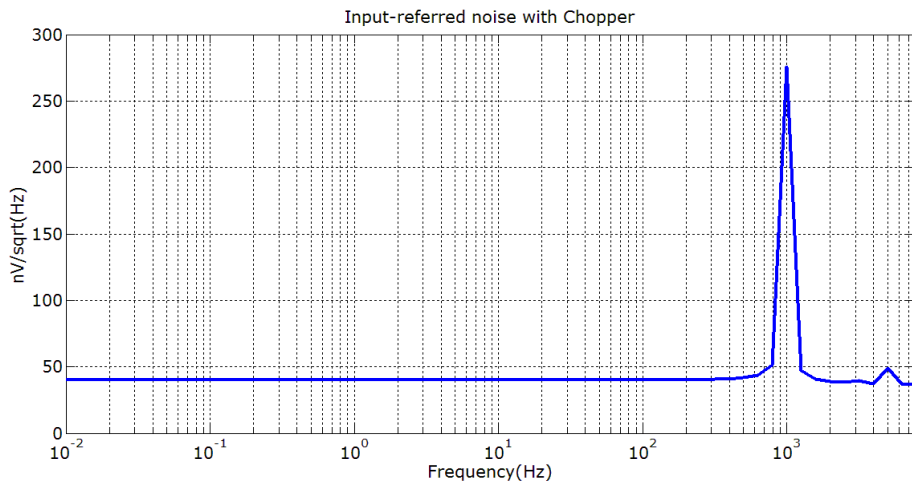


Fig. 2.36 Noise simulation response with chopper showing the transposition of the flicker noise pole to 1 kHz.

### 2.9 Noise Simulation Comparison

Parameter	Without Chopper	With Chopper
Input-referred Noise (0.01Hz -300Hz)	2.1 $\mu$ Vrms	0.69 $\mu$ Vrms
Spot Noise @ 10Hz	180 nV/ $\sqrt$ Hz	39.89 nV/ $\sqrt$ Hz
Corner frequency	1 kHz	< 10mHz

The frequency response of the chopper-stabilized INA is shown in Fig. 2.37 and a dc-gain of 32.65 dB was achieved. A sudden dip was observed in the vicinity of the chopping frequency of 1 kHz, but this dip will not affect the performance as our range of operation would be from 0.01Hz- 300Hz.

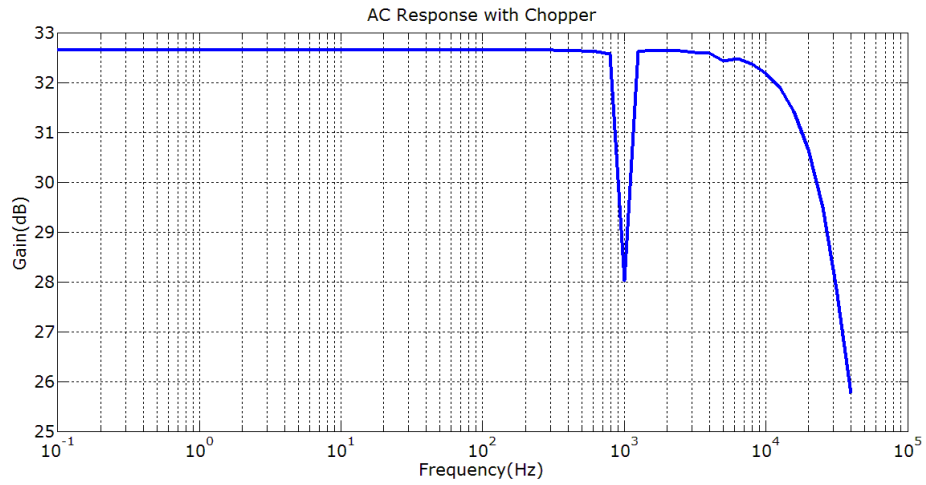


Fig. 2.37 Frequency response simulation with chopper

Similar techniques as used for the DDA-based INA design were used to for the layout of the fully-differential chopper-stabilized INA. Special care was taken to maintain symmetry for the input and output signal paths. Common centroid scheme was used to ensure reduction of mismatches and enhance CMRR. The chip-size without bond-pads was  $0.68\text{mm} \times 0.48\text{ mm}$ . The layout of the fully-differential chopper-stabilized INA with various blocks is shown in Fig. 2.38. The layout of the switch-capacitor CMFB circuit and the non-overlapping clock generator was done by Mr. Yen-Ting Liu. The OTA layout was done by me.

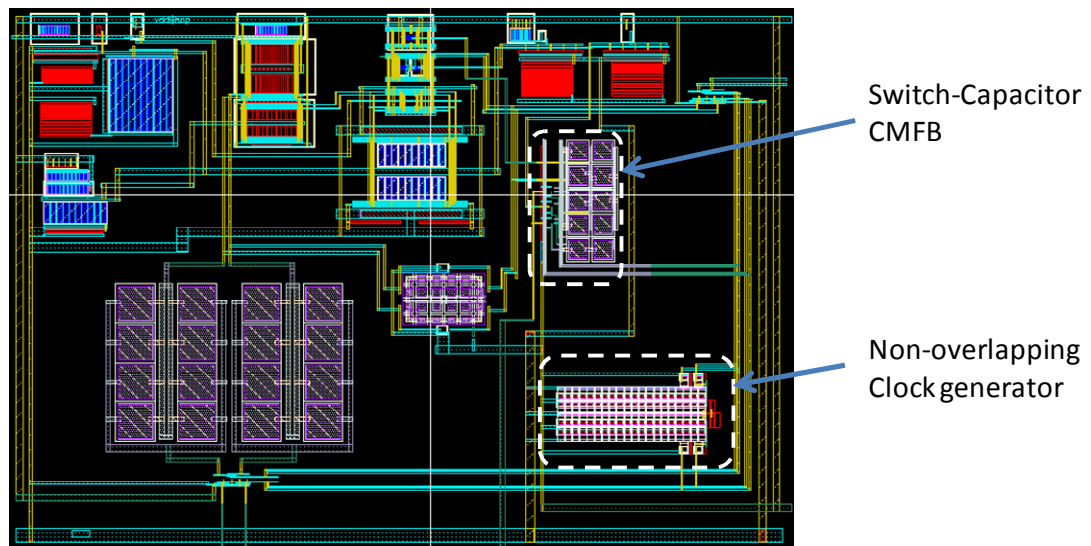


Fig. 2.38 Layout of the fully differential capacitive feedback chopper stabilized INA in TSMC CMOS  $0.18\ \mu\text{m}$  process.

### 2.5.7 Simulated performance comparison

The fully differential capacitive feedback chopper stabilized INA is compared with the DDA-based chopper stabilized INA in terms of the topology and the performance. The comparison is shown in Table.2.10 and Table.2.11 respectively.

Table.2.10 Topological Comparison (post-layout simulation)

Parameter	LBC7 0.35 $\mu\text{m}$ , Nov 2011	TSMC 0.18 $\mu\text{m}$ , March 2012
Topology	DDA-based Single Ended	Folded Cascode-based Fully Differential
Stage	3-Stage	Single Stage
Feedback	Resistive	Capacitive
Chopper Frequency	5 kHz	1 kHz
Corner Frequency	12.5 kHz	1 kHz

Table.2.11 Performance Comparison (post-layout simulation)

Parameter	LBC7 0.35 $\mu\text{m}$ , Nov 2011	TSMC 0.18 $\mu\text{m}$ , March 2012
Supply Voltage	2 V	1.8 V
Supply Current	<1.5 $\mu\text{A}$	<2.5 $\mu\text{A}$
Open-loop dc Gain	>120 dB	110 dB
Closed-loop dc Gain	40.8 dB	32.7 dB
CMRR	> 110 dB	105 dB
Spot Noise	265 nV// $\sqrt{\text{Hz}}$ @ 10 Hz	39.89 nV// $\sqrt{\text{Hz}}$ @ 10 Hz

As can be observed from Table.2.11, the folded-cascode based fully-differential capacitive feedback INA shows an improvement in the noise performance. This improvement can be attributed to the current scaling technique and the various other noise suppressing techniques discussed and implemented. Additionally, the reduction in the number of noise-contributing devices also results in a lower input-referred noise.

### 2.5.8 State-of-the-art-performance comparison

The performance of different low-noise and low-power instrumentation amplifier designs applied to different types of bio-signals are compared with the present design, as shown in Table.2.12,

Table.2.12 State-of-the-art performance comparison

	W'panitch et.al [2007] [53]	Qian et.al [2011] [64]	Wu et.al [2009] [65]	Denison et.al [2007] [50]	Fan et.al [2011] [54]	Guo et.al [2012] [57]	This Work (post-layout simulation)
<b>Current</b>	2.7 $\mu\text{A}$	0.872 $\mu\text{A}$	230 $\mu\text{A}$	1 $\mu\text{A}$	1 $\mu\text{A}$	22.4 $\mu\text{A}$	2 $\mu\text{A}$
<b>Power</b>	7.6 $\mu\text{W}$	2.4 $\mu\text{W}$	1 mW	2 $\mu\text{W}$	1.8 $\mu\text{W}$	73.9 $\mu\text{W}$	4 $\mu\text{W}$
<b>Gain</b>	40.85 dB	39.4 dB	40 dB	40 dB	40 dB	26 dB	32.65 dB
<b>Bandwidth</b>	45 Hz – 5.32 kHz	0.36 Hz – 1.3 kHz	800 kHz	1 kHz	-	30 kHz	25.1 kHz
<b>IRN voltage</b>	3.06 $\mu\text{V}_{\text{rms}}$ [10 Hz -98 kHz]	3.07 $\mu\text{V}_{\text{rms}}$ [0.5 Hz - 30 kHz]	-	1.3 $\mu\text{V}_{\text{rms}}$ [0.05 Hz -4 kHz]	6.7 $\mu\text{V}_{\text{rms}}$ [0.5 Hz - 100Hz]	0.9 $\mu\text{V}_{\text{rms}}$ [1 Hz - 200Hz]	0.69 $\mu\text{V}_{\text{rms}}$ [0.05 Hz - 300Hz]
<b>1/f noise corner</b>	-	50 Hz	1 mHz	3 Hz	100 mHz	23 Hz	< 1 Hz
<b>Noise PSD</b>	31 nV/ $\sqrt{\text{Hz}}$	60 nV/ $\sqrt{\text{Hz}}$	15 nV/ $\sqrt{\text{Hz}}$	94 nV/ $\sqrt{\text{Hz}}$	60 nV/ $\sqrt{\text{Hz}}$	32.9 nV/ $\sqrt{\text{Hz}}$	39.89 nV/ $\sqrt{\text{Hz}}$
<b>NEF</b>	2.67	3.09	8.8	4.6	3.3	4.5	2.8
<b>CMRR</b>	> 66 dB	> 66 dB	> 120 dB	100 dB	134 dB	> 110 dB	>66 dB
<b>Chopping Frequency</b>	-	-	40 kHz, 510 kHz	4 kHz	5 kHz	10 kHz	1 kHz
<b>Process</b>	0.5 $\mu\text{m}$ CMOS	0.6 $\mu\text{m}$ CMOS	0.7 $\mu\text{m}$ CMOS	0.8 $\mu\text{m}$ CMOS	65 nm CMOS	0.35 $\mu\text{m}$ CMOS	0.18 $\mu\text{m}$ CMOS

## CHAPTER 3

### ANALOG FRONT-END CIRCUITS AND SYSTEM CHARACTERIZATION AND TESTING OF BIO-SENSOR: ECG AND ICD/PACEMAKER

The chopper stabilized bio-signal instrumentation amplifiers (INA) for the analog front-end (AFE) IC were designed and fabricated. The DDA-based chopper stabilized INA was fabricated using Texas Instruments (TI) proprietary LBC7 0.35 $\mu$ m BCD process and the fully-differential folded cascode based chopper stabilized INA was fabricated in a TSMC 0.18 $\mu$ m CMOS process. The unpackaged dies obtained were wire bonded with the help of our Lab mate Mr. Cliff Schecht, using the Kulicke-Soffa bonding machine at Dr. Lie's lab. For the characterization of the fabricated dies, custom printed-circuit boards (PCBs) were designed and fabricated to mount the dies for testing. Proper electrostatic discharge (ESD) protection practice was observed during the testing and measurements to safeguard the unpackaged dies.

#### 3.1 Setup for die characterization

The test-setup used for the transient response and frequency response characterization of the chopper stabilized INA is shown in Fig. 3.1. A sinusoidal signal was provided as an input to the chopper stabilized INA using the HP33120A signal generator. Since both of our INAs need differential inputs, the single-ended input signal from the signal generator was converted into a differential signal, using Analog Devices AD8476, before applying it to the chopper stabilized INA. The PCB used for the testing was powered by 2-AA batteries. The clock signal used to generate the non-overlapping clock was provided using a square wave signal of required frequency from the HP33120A signal generator. The output of the chopper stabilized INA was connected to a unity-gain buffer in order to drive external equipments. This buffer was realized using a Micrel MCP6v26 op-amp. A high-precision, low-noise amplifier, SR560 (by Stanford Research), was used as a low-pass filter to discard the undesired high-frequency content such as the signal harmonics and the translated noise

and dc-offsets, etc. For verifying the transient responses, the output of the low-pass filter was connected to the Tektronix oscilloscope; whereas for the frequency response characterization, the HP3562A dynamic signal analyzer was connected to the low-pass filter in Fig. 3.1.

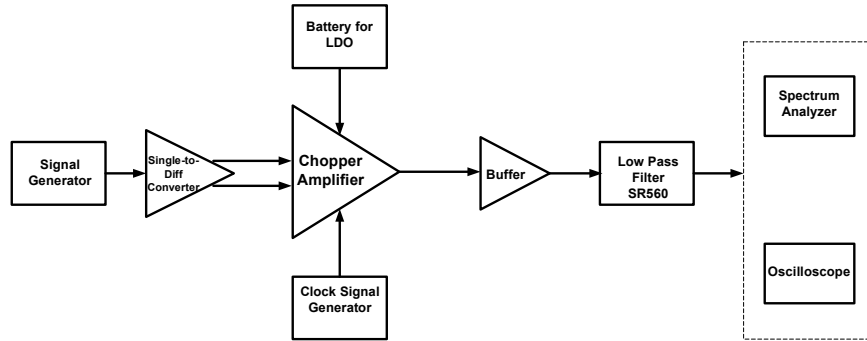


Fig. 3.1 Measurement setup for chopper-stabilized INA transient and frequency response characterization.

The setup for measuring the noise performance of the designed chopper-stabilized INAs is shown in Fig. 3.2. The setup is similar to the one used for frequency response characterization, except for the inclusion of an additional gain stage in place of the low-pass filter. The additional gain stage was required as the noise of the HP3562A dynamic signal analyzer would otherwise overwhelmed the noise of the circuit, thus making its noise performance difficult to be measured. This gain stage was realized using a low-noise amplifier INA826 from Texas Instruments (TI), which was configured to provide a gain of 100 times (40 dB).

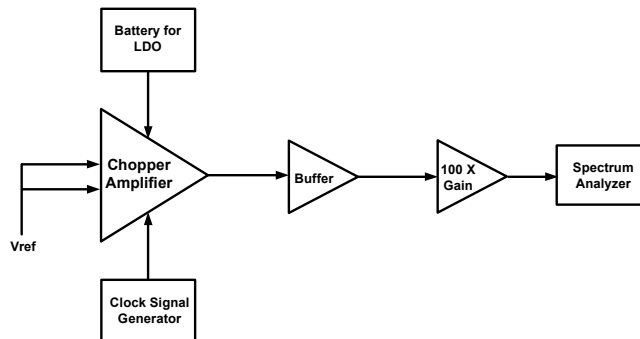


Fig. 3.2 Measurement setup for the chopper-stabilized INA noise characterization

### 3.2 Measurement results for the DDA-based chopper stabilized INA

The transient response of the DDA-based chopper stabilized INA was measured using the setup shown in Fig. 3.1. The INA output before and after filtering has been shown in Fig. 3.3. The channel 1 denoted as ‘OUT\_FIL’ represents the output as measured after passing through SR560 low-pass filter with a cutoff frequency of 300Hz, whereas channel 2 denoted as ‘OUT’ represents the output as measured after the external buffer. Chopper frequency of 5 kHz was used in the DDA-based chopper stabilized INA.

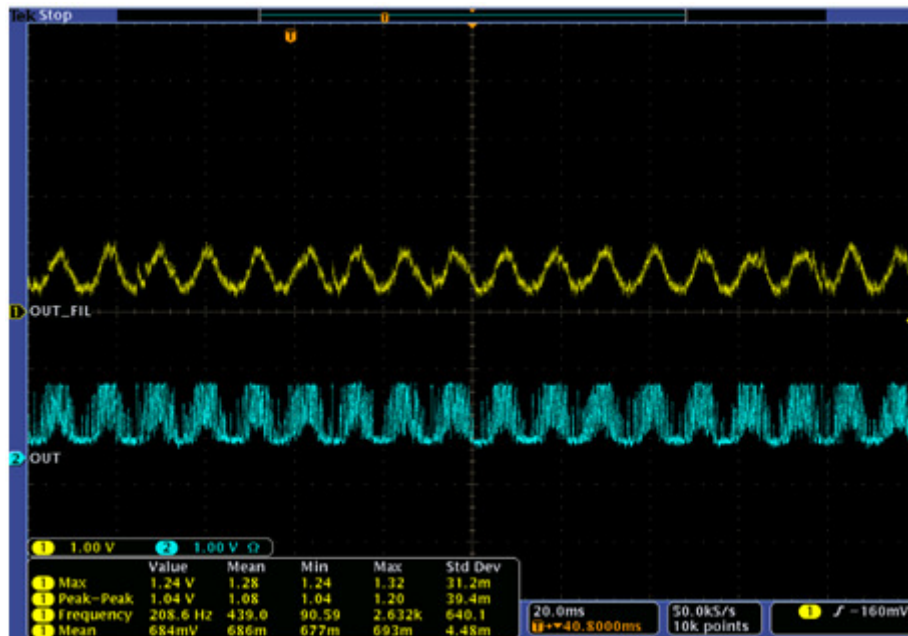


Fig. 3.3 Measured transient response for our chopper-stabilized INA before (lower) and after (top) the low-pass filter.

The noise of the chopper stabilized INA was measured using the setup shown in Fig. 3.2. As can be seen in Fig. 3.4, a measured spot noise of 240 nV/ $\sqrt{\text{Hz}}$  at 10 Hz was recorded; also the noise pole was translated to 5 kHz as designed. The corresponding simulation response can be seen in Fig. 3.5 where a spot noise of 256 nV/ $\sqrt{\text{Hz}}$  at 10 Hz was observed; also the noise pole was translated to 5 kHz by design.

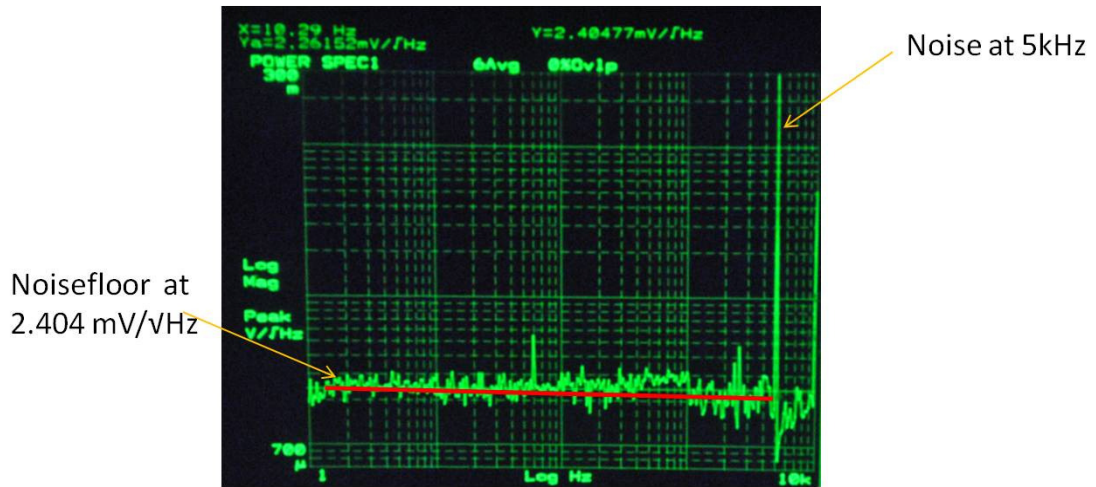


Fig. 3.4 Measurement result for noise response of our chopper stabilized amplifier

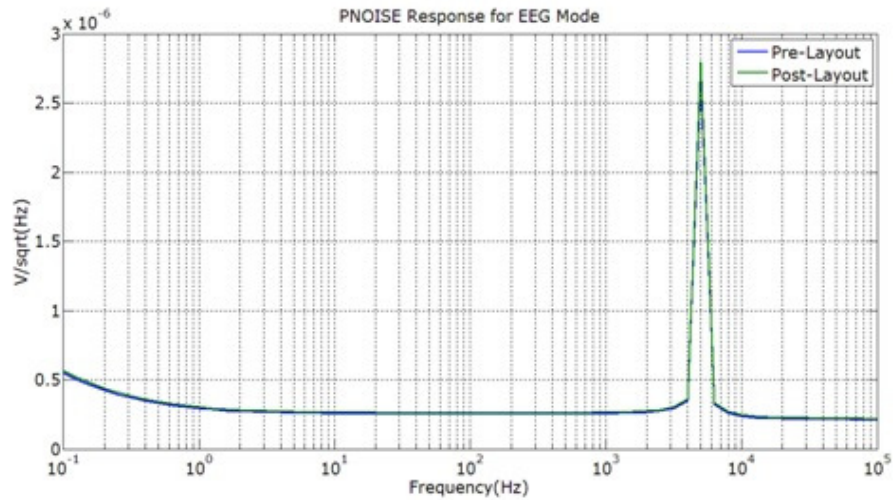


Fig. 3.5 SPICE simulation result for noise response of our chopper stabilized INA

The noise of the INA without chopper stabilization was measured using the setup shown in Fig. 3.2. For disabling chopper stabilization the clock for the chopper switches was pulled to  $V_{dd}$ . A spot noise of  $4.4 \mu\text{V}/\sqrt{\text{Hz}}$  at 10 Hz was observed as can be seen in Fig. 3.6. The corresponding simulation response can be seen in Fig. 3.5 where a spot noise of  $4.6 \mu\text{V}/\sqrt{\text{Hz}}$  at 10 Hz was observed.

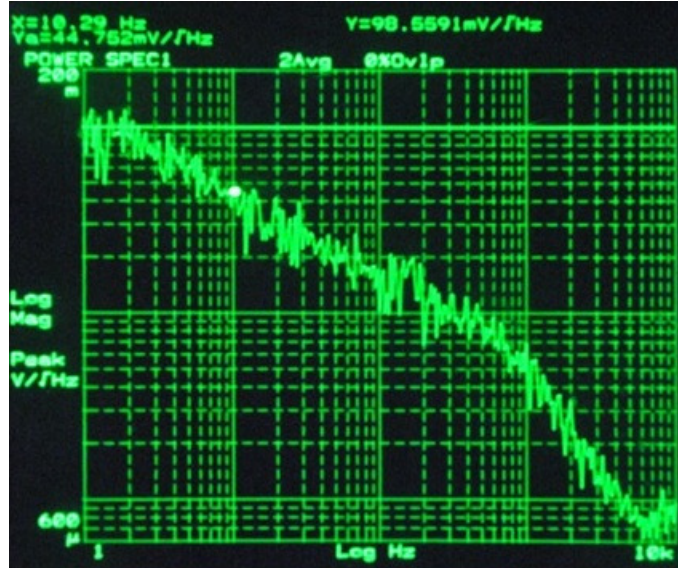


Fig. 3.6 Measurement result for noise response without chopper stabilization.

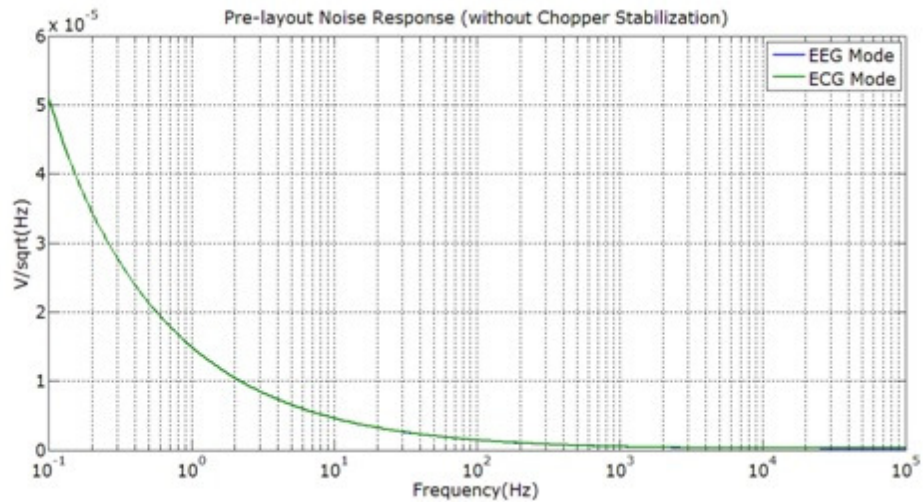


Fig. 3.7 SPICE simulation result for noise response without chopper stabilization

The frequency response of the chopper stabilized INA for the ECG mode was measured using the setup shown in Fig. 3.1. A dc-gain of 19.47 dB was recorded and can be seen in Fig. 3.8. Table.3.1 shows the good agreement between the simulated vs. the measured data for our CMOS INA.

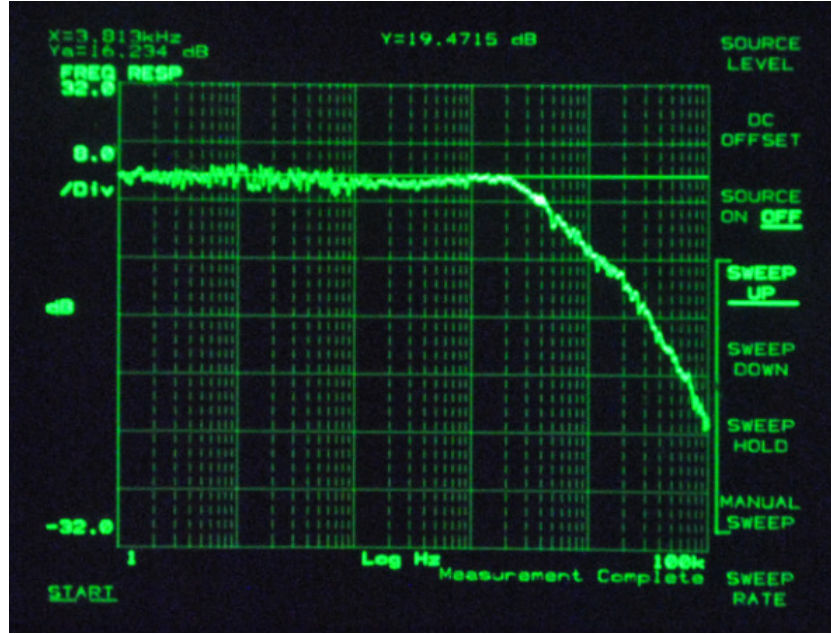


Fig. 3.8 Measured frequency response with our chopper amplifier for the ECG mode

Table.3.1 Summary of our 0.35 $\mu$ m CMOS INA performance in TI LBC7.

Parameters	Measurement	Simulation
Power Supply	2 V	2 V
INA current consumption	2.8 $\mu$ A ( can be lower)	2.8 $\mu$ A ( can be lower)
INA gain	19.5 dB	21.6 dB
INA bandwidth (with chopper)	[dc - 3.9 kHz] @ 20 dB	[dc - 4.7 kHz] @ 20 dB
INA bandwidth (without chopper)	[151.8 Hz, 3.5 kHz]	
Noise (with Chopper) @ 10Hz	240 nV/ $\sqrt$ Hz	256 nV/ $\sqrt$ Hz
Noise (without Chopper) @ 10Hz	4.45 $\mu$ V/ $\sqrt$ Hz	4.6 $\mu$ V/ $\sqrt$ Hz

### 3.3 Measurement results for the fully differential folded cascode-based chopper stabilized INA

The TSMC chopper-stabilized 0.18  $\mu$ m INA was bonded onto the dedicated PCB for testing. Preliminary testing results have not been encouraging, with the unsuccessful recording of its transient responses. The test set-up is shown in Fig. 3.9

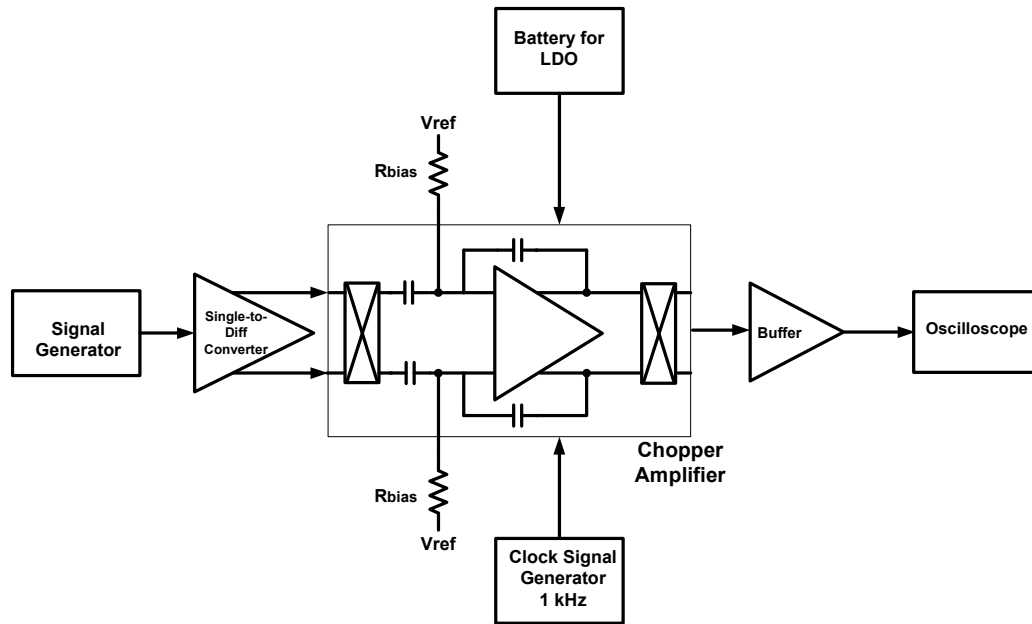


Fig. 3.9 Measurement setup for our chopper-stabilized INA transient response

The following observations were made during the INA testing:

1. The differential input signal provided at the input terminals before the chopper switches was not able to reach the input terminals of the OTA.
2. The dc bias points at the gate of the input pair MOSFET were not properly set to the desired 0.9V when high value resistors like 5G $\Omega$  were used for providing dc-bias. With 5G $\Omega$  resistor a dc value of close to 0V was measured. But it was seen that when a smaller value resistor like 1.5M $\Omega$  was used, 0.9V was measured at the OTA input terminal. Since the OTA input terminal is the gate terminal of the MOSFET, it typically exhibits very high impedance, hence such a behavior was not expected.
3. On the application of a large signal (few hundred mV), the transient response at the output was observed, but it was not commensurate with the desired amplification. This signal was applied directly at the OTA input. The transient response is shown in Fig. 3.10. The signal was also observed on the spectrum display, Fig. 3.11 shows a screen capture.

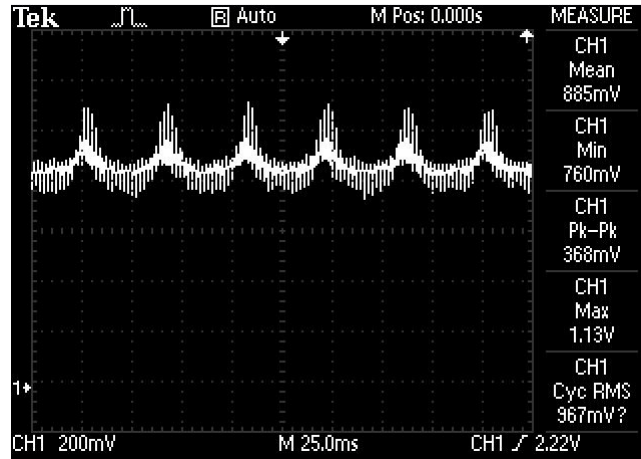


Fig. 3.10 Single-ended transient response of the fully-differential folded-cascode based INA.

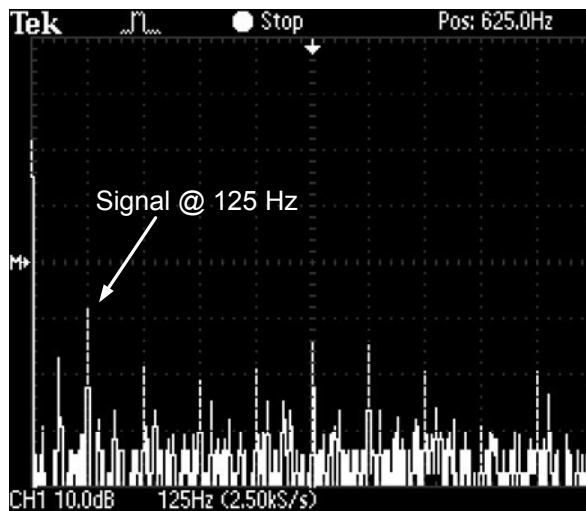


Fig. 3.11 FFT response of the output for 125 Hz input signal of the fully-differential chopper INA.

- 4 Clock signal has been observed to dominate the output signal most of the times. Though clock spikes are expected in the unfiltered output, in testing it was observed that clock would overwhelm the intended signal.
- 5 The die was provided with supply voltage before connecting the bias voltage to check for the input pair dc bias points, and during this process the chopper switches were not connected. It was observed that the dc points

were stable then. But after enabling the chopper switches, a sudden drop in the dc points was observed.

Current was measured using a Keithley Picoammeter 6485 as shown in Fig. 3.12, and the bias current was measured as  $1.2 \mu\text{A}$ . On further testing the die was seen to have an abrupt breakdown, which was evident due to the sudden drop in the output dc points as well unexpected supply current (jumped into the range of 2 - 4 mA).

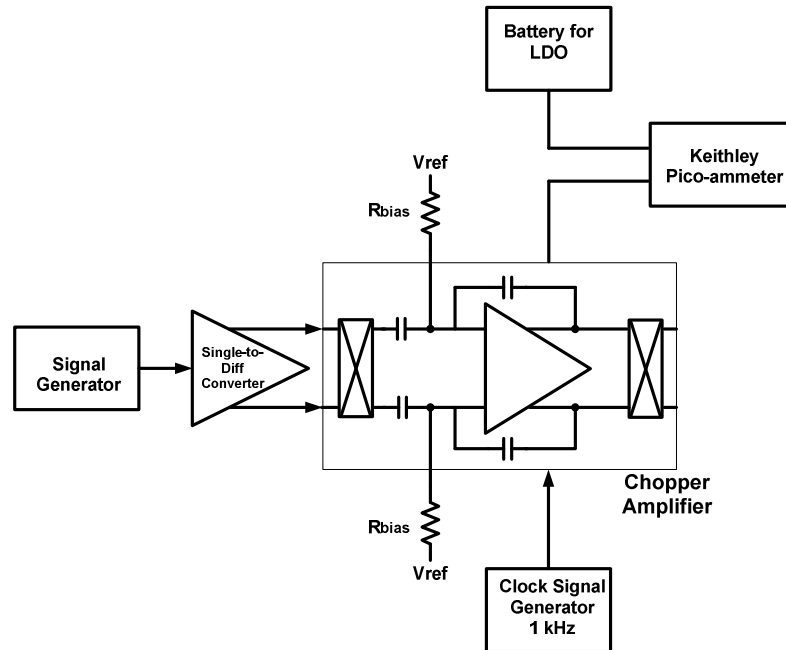


Fig. 3.12 Current measurement setup using a Keithley Pico-ammeter

### 3.4 Electrocardiogram (ECG or EKG) measurement

The diastolic-systolic cardiac activity generates electrical signal which can be sensed from the body surface and used for subsequent diagnosis and monitoring of the conditions of the heart. The electrical activity of the heart can be modeled as a vector quantity [3]. In a simplistic model, the heart is considered to be consisting of an electrical dipole situated in a partially conducting medium of the thorax. As shown in Fig. 3.13, the dipole comprises of points of equal positive and negative charges separated from one another and denoted by the dipole moment vector  $\mathbf{M}$  [3].

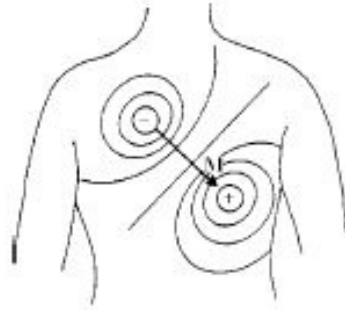


Fig. 3.13 Dipole moment vector showing heart's electrical nature.

The instantaneous cardiac activity is represented by the aforementioned dipole and the electric field associated with the dipole. The changes in the magnitude and orientation of the dipole due to cardiac activities will lead to changes in the associated electric field. This time-varying behaviors of the cardiac dipole can be understood by using the dipole moment vector  $\mathbf{M}$ , also known as the *cardiac vector* [3]. With the cardiac motions, the magnitude and direction of this cardiac vector will vary accordingly, thus providing information regarding the heart.

The electrical signals due to the cardiac activities can be tapped on the body surface using biopotential electrodes, and for this usually the potential *difference* between the electrodes is measured. Assuming two electrodes to be placed on equal-potential lines of the electric field of the heart, a non-zero potential difference is detected [3]. This potential difference is related to positions of the electrodes, which if the electrodes are placed arbitrarily on the body can lead to signal randomness. For this reason a standard is desired which specifies the placement of the biopotential electrodes.

By utilizing the dipole model of the heart, it is possible to ascertain the instantaneous voltage for a particular set of electrodes. Considering the arrangement shown in Fig.3.14, the two electrodes can be defined using a lead vector. Lead vector is a unit vector which defines the direction a constant-magnitude cardiac vector must have to generate maximal voltage in a particular pair of electrodes [3]. Typically a pair of electrodes and sometimes a network of electrodes form a lead. As can be seen in

Fig. 3.10, the voltage induced by the cardiac vector  $\mathbf{M}$  in the lead vector  $\mathbf{a}_1$  can be determined by the component of  $\mathbf{M}$  projected unto the direction of  $\mathbf{a}_1$ . Using the dot product from vector algebra, we have [3],

$$v_{a_1} = \mathbf{M} \cdot \mathbf{a}_1 \Rightarrow M \cos \theta \quad (3.1)$$

Considering the second lead vector  $\mathbf{a}_2$  as shown in Fig. 3.14, this lead vector is oriented perpendicular to the cardiac vector  $\mathbf{M}$ . This implies that the component of  $\mathbf{M}$  along the direction of  $\mathbf{a}_2$  is zero. ( $\because \cos 90^\circ = 0$ ). To uniquely define the cardiac vector  $\mathbf{M}$ , at least two lead vectors are necessary [3].

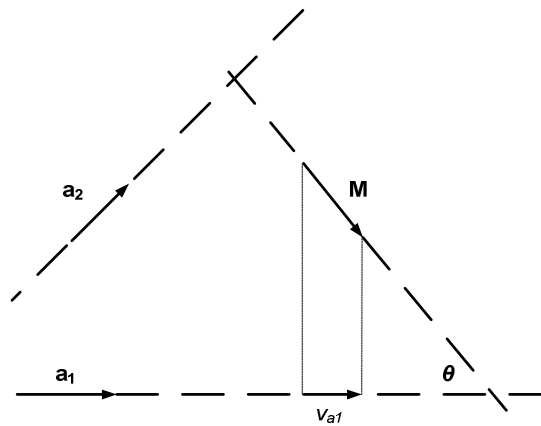


Fig. 3.14 Estimation of cardiac vector using lead vectors

For clinical electrocardiogram (ECG), a 3-lead frontal plane arrangement is a typical minimum requirement to record high quality reliable data in terms of the minimum number of leads. In this standardized arrangement, one electrode each is placed at the right arm (RA), the left arm (LA) and the left leg (LL) [3]. The three leads formed are lead I, LA to RA; lead II, LL to RA; and lead III, LL to LA. The resulting lead vectors can be approximated as an equilateral triangle known as the *Einthoven's triangle*, as shown in Fig. 3.15 [3], [68]. Einthoven's triangle is named after its discoverer Willem Einthoven who received the Nobel Prize in Medicine in 1924 for this work. It was Einthoven who also named the various deflections of the cardiac activity or a typical ECG waveform using the alphabets P, Q, R, S and T.

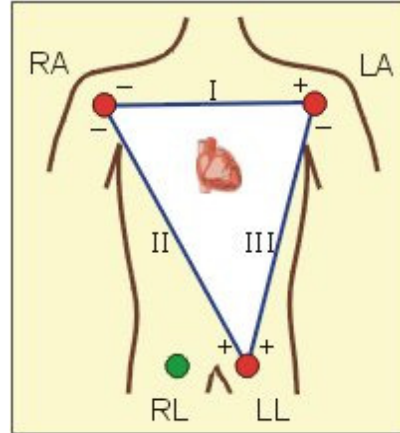


Fig. 3.15 Einthoven's triangle for ECG [68]

To understand the 3-lead ECG measurement, we at Dr. Lie's lab used a custom built printed circuit board (PCB), as well as a commercially available ECG simulator for measuring the ECG signals on human subjects. The fully-differential PCB was originally designed using low-noise commercial-of-the-shelf (COTS) parts by Mr. Cliff Schecht in our group. This PCB was first designed for very low-noise ECoChG (electrocochleography) measurements, but was later on re-designed for surface ECG measurements by changing the overall gain and the band-pass filter settings on the board, etc. To accommodate the relatively weaker ECoChG signal the original board was set for a high gain of 130 dB with the low-pass cut off in few kilo-Hz. For ECG measurements, the gain was set at around 46 dB with the band-pass filter cutoffs at 0.05 Hz and 150 Hz, respectively. ECG measurements on human subjects were recorded using snap electrodes. The block diagram of the PCB-based AFE circuits for the ECG measurement is shown in Fig. 3.16.

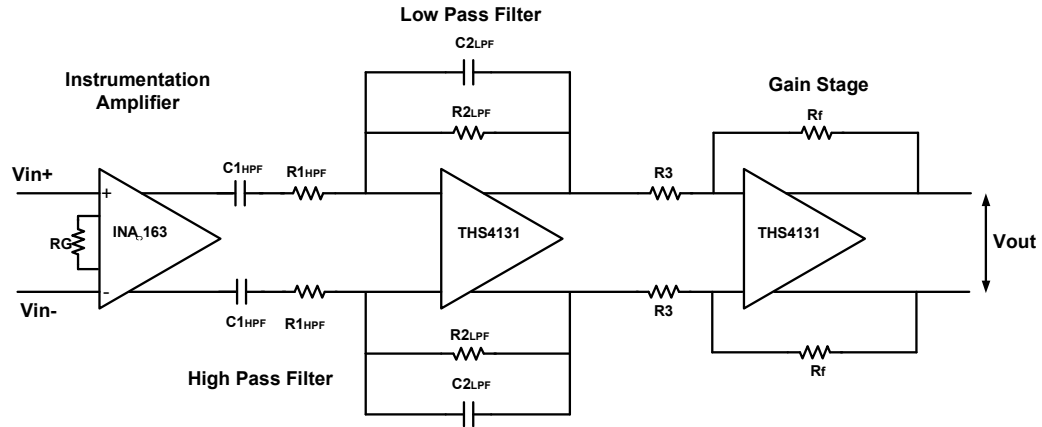


Fig. 3.16 Fully differential PCB-based AFE.

The frequency response of the differential board was acquired using the low-frequency spectrum analyzer, as shown in Fig. 3.17. A high-pass 3-dB cut-off at 870 mHz was observed and a low-pass 3-dB cut-off at 157 Hz was observed. A mid-band gain of 45.3 dB was achieved. The fully-differential PCB-based AFE circuits was tested for ECG signals from a commercially available Simulaids™ ECG simulator, and later recorded from human subjects as well.

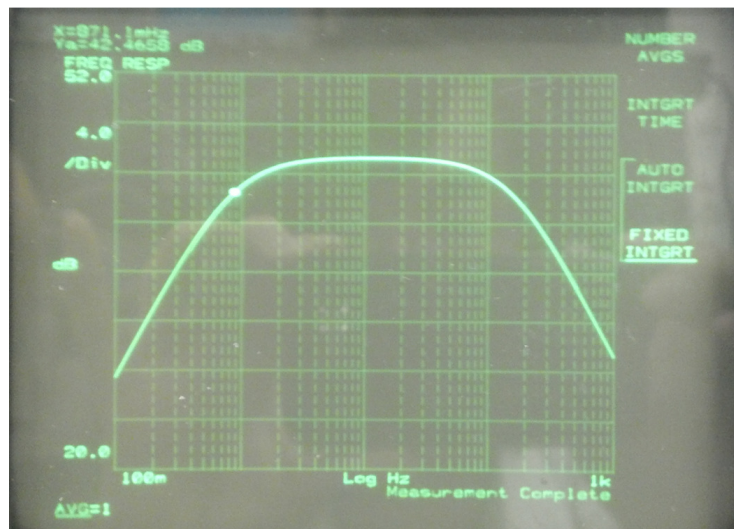


Fig. 3.17 Frequency response of the fully differential PCB-based AFE circuits.

The PCB-based AFE circuits was tested using a Simulaids™ ECG simulator and shown in Fig. 3.18 is the output waveform capture of the board for a normal sinus

rhythm (NSR) input of 72 bpm. This is a differential output obtained using MATH operation (CH1-CH2) on the oscilloscope. We can also see the frequency of 1.218 Hz, which corresponds to 72 bpm as specified in the Simulaid's specification sheet for NSR ECG.

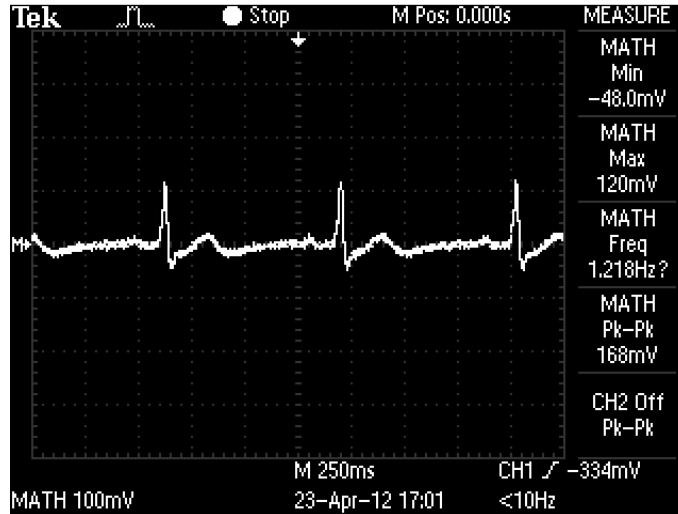


Fig. 3.18 Measured transient response of the fully differential PCB-based AFE circuits using inputs from a Simulaid's™ ECG simulator

The ECG recording using our PCB-based AFE circuits from a Simulaid's™ NSR ECG input was recorded at a sampling frequency of 300Hz, and has been plotted after being filtered (low-pass filter with a cut-off of 50Hz), as shown in Fig. 3.19, with the clear showing of the typical P, Q, R, S, T waves. Just to double-check, the Simulaid's™ NSR ECG recording shown in Fig. 3.19 is compared with Physionet sample ECG signal as shown in Fig. 3.20 [69]. One can see the two recordings appear to be very similar, except for the periodicity, which suggests the recording quality of our PCB-based AFE circuits is rather good.

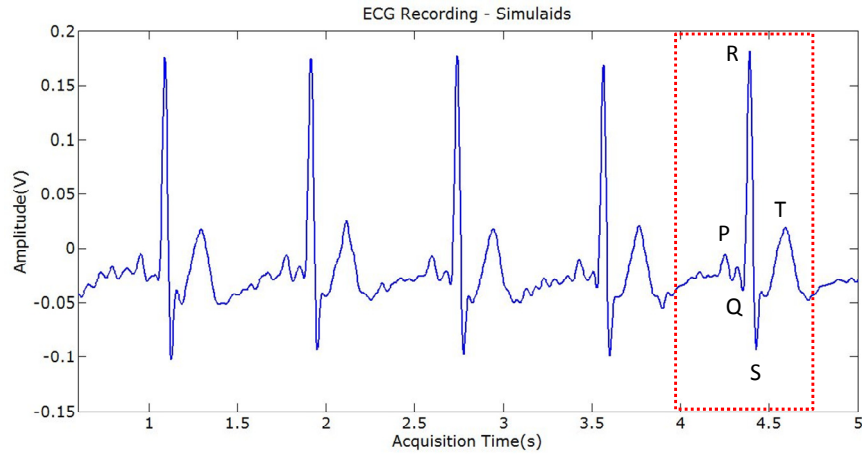


Fig. 3.19 Simulaid<sup>TM</sup> NSR ECG waveform recorded using the fully differential PCB-based AFE circuits

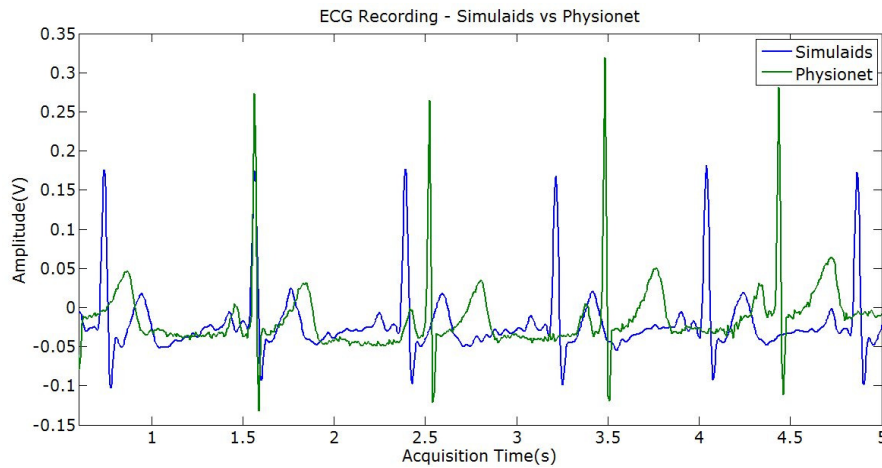


Fig. 3.20 Simulaid<sup>TM</sup> NSR ECG overlaid with Physionet data.

Additionally, an ECG was recorded on a human subject (a student volunteer) at a sampling frequency of 300Hz using our PCB-based AFE circuits, and has been plotted after being filtered (low-pass filtered with a cut-off of 50Hz) as shown in Fig. 3.21. The human ECG recording is also compared with a Physionet sample ECG signal as shown in Fig. 3.22 [69]. Again, the human ECG recording distinctly exhibits all the components of the typical ECG waveform of the P, Q, R, S, T waves.

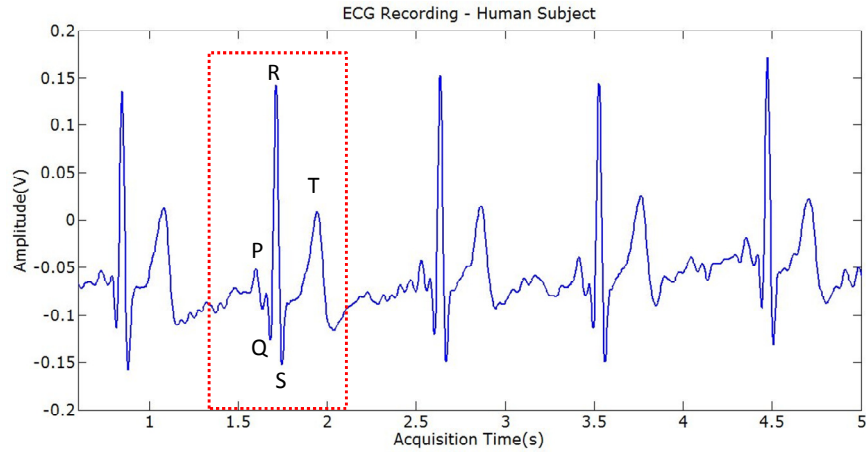


Fig. 3.21 Human subject ECG recorded using the fully differential PCB-based AFE circuits

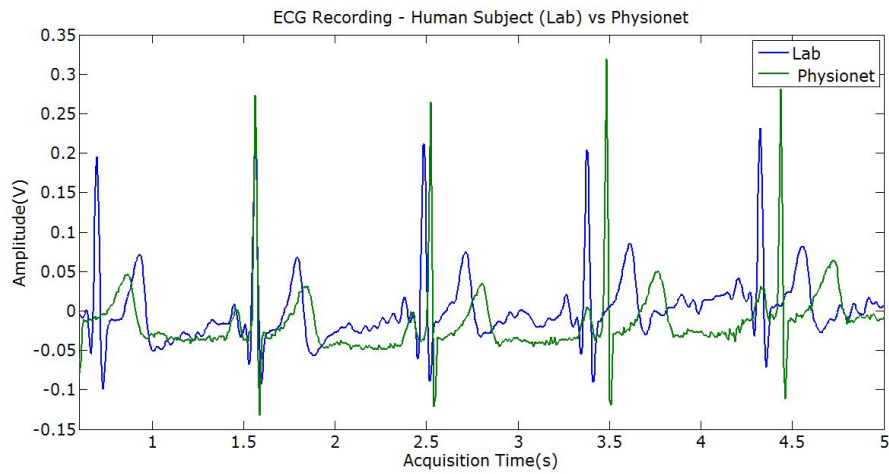


Fig. 3.22 A human subject ECG waveform recording using our PCB-based AFE circuits overlaid with a Physionet ECG data (the same one shown in Fig. 3.19).

## CHAPTER 4

### **ANTENNA EVALUATION OF A NON-CONTACT VITAL SIGNS (NCVS) SENSOR FOR CONTINUOUS HEART AND RESPIRATION RATES MONITORING**

Non-contact monitoring of human physiological parameters using a Doppler radar has been proposed for many decades, with initial applications in apnea and respiration monitoring [1], [26], [70]. Later, wireless heart monitoring was also demonstrated [27]. More recently, arctangent quadrature demodulation has been used to achieve high frequency operation and with large system sensitivity to small displacements [30], [31]. High sensor sensitivity to small displacements is a key feature for successful NCVS monitoring systems, which also requires robust detection and demodulation of both heart and pulmonary movements simultaneously. Such NCVS sensor systems capable of continuous wireless monitoring can be of great value for both clinical applications and home healthcare (e.g., for wireless-assisted living and wireless acute-care). For the design of a NCVS monitoring system using a Doppler radar, the signal penetration depth is dictated by the microwave attenuation in human tissues and clothing/blanket, and this factor must be carefully considered [45], [71]. Systems operating at the X-band have a penetration depth of close to 3 mm in human tissue, and therefore will mostly detect the body surface motion rather than the direct movement from the heart [72] (note the heartbeat signal can still be detected from small heart movement on top of the pulmonary movement at the surface of the chest). On the other hand, systems operating closer to the L-band can achieve penetration depths of close to 5 cm in human tissue, which can be useful for more direct heart movement detection, and go through the clothing and blanket of the subject being monitored [30], [71]. However, the sensitivity of a Doppler radar system to small displacements is inversely proportional to the wavelength selected, and thus sensor systems using higher operating frequencies such as X-band will be more sensitive than a system using frequencies closer to L-band. An obvious trade-off between effective signal penetration and signal sensitivity is observed here, but we

chose L-band 2.4GHz for its better penetration depth to prevent the EM wave being completely blocked by the clothing or blanket. Furthermore, for successful clinical applications it is wise to have the Doppler radar system adhere to an ISM frequency band, and must not violate the transmission emission standards set by the regulating bodies (say FCC or FDA, for example).

#### **4.1 NCVS system for the antenna evaluation at Dr. Lie's lab**

Since the nature of the antenna is an important factor in the sensitivity of the NCVS sensor system, hardware performance evaluation with different types of antennas for the portable NCVS monitoring system was carried out at Dr. Lie's lab. Experimental data for continuous heart and respiration rate monitoring was recorded in the anechoic chamber using the portable fourth generation NCVS sensor system developed at Dr. Lie's lab. The NCVS sensor system operates at the 2.4 GHz ISM band using a CW Doppler radar, where periodic chest motions of the monitored subject cause phase modulation that can be demodulated to detect the heart and respiration rates separately [29], [30], [31]. As discussed in chapter 1, the subject is illuminated with separate Tx and Rx antennas to avoid the use of bulky and expensive circulators. The Rx signal which is a phase-modulated and time-delayed version of the Tx signal, is downconverted using the same local oscillator (LO) signal as used for the Tx signal. This allows for the benefits of range correlation to reduce degradation caused by phase noise [29], [32]. After down-conversion, full quadrature arctangent demodulation is carried out to extract the time-varying phase information for subsequent cardio-pulmonary rate estimation [30].

The block-level diagram of our NCVS sensor system is shown in Fig. 4.1, where the Rx section consists of a 2-way  $0^\circ$  balun that splits the received signal and provides the RF input into the quadrature I/Q mixers. The custom built NCVS sensor uses passive mixers for their superior linearity and better noise performance when compared to active mixer [73]. A circulator was not used since it may cause self-mixing to generate dc offset errors at baseband [44]. Also, using a circulator adds an

extra bulky and expensive component, making it very difficult for the sensor to be integrated as a System-on-a-Chip (SoC) in the future. The Tx CW signal for this 4<sup>th</sup> generation sensor is generated by a frequency synthesizer with an external Pierce oscillator based 10.24 MHz reference to ensure excellent phase noise and thermal stability.

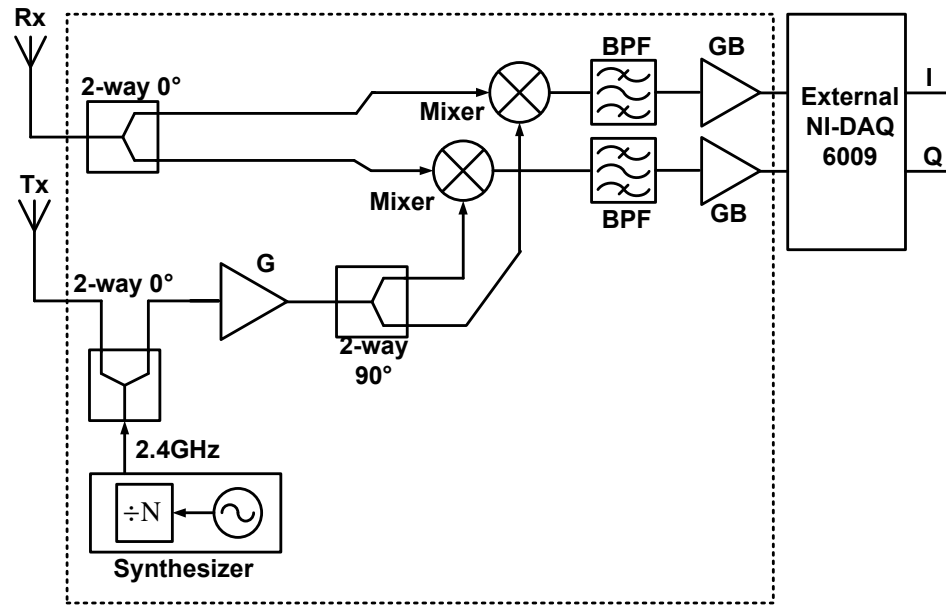


Fig. 4.1 Fourth generation NCVS sensor hardware.

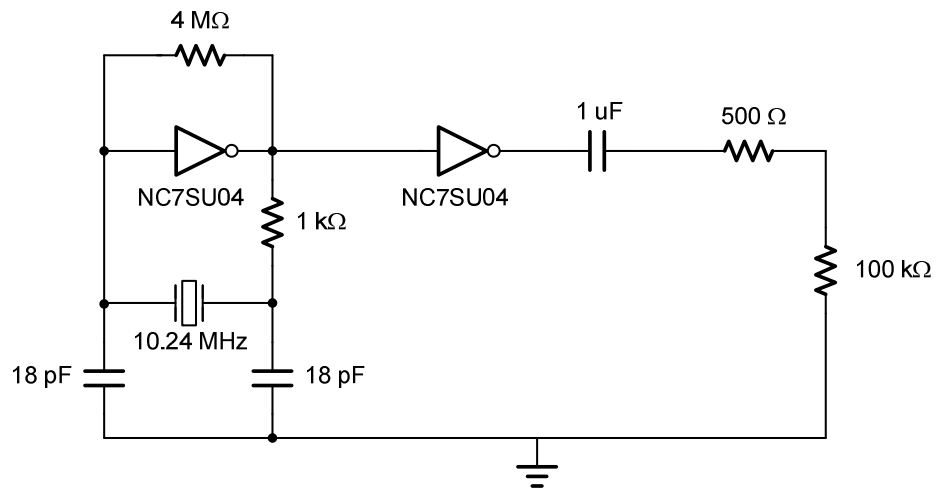


Fig. 4.2 The CMOS inverter based 10.24 MHz reference oscillator

The synthesizer output on our NCVS hardware is split by a 2-way  $0^\circ$  balun to feed the Tx antenna, and a 2-way  $90^\circ$  degree splitter to create the  $0^\circ/90^\circ$  LO signal for the I/Q mixers, as shown in Fig.4.1. The excellent phase noise of the LO has been characterized and shown in Fig. 4.3 (e.g., -111 dBc/Hz at 10kHz offset), which should be more than adequate for Doppler radar NCVS system [29].

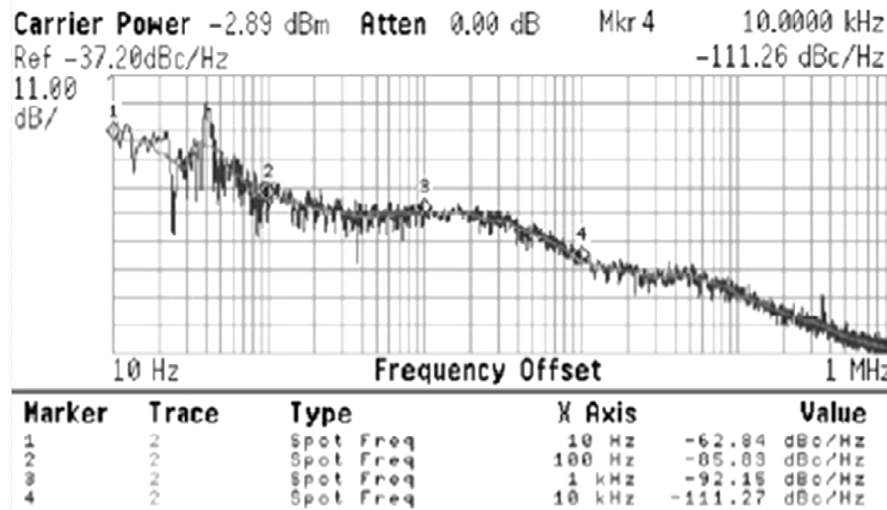


Fig. 4.3 Measured phase noise of the synthesizer used in our fourth generation NCVS sensor hardware.

After the I/Q mixers stage, the signal is further conditioned with the Sallen-Key 2<sup>nd</sup> order low-pass and high-pass filters with cutoff frequencies at 10 and 0.1 Hz, respectively, using non-inverting op-amps with a voltage gain of 60 dB [34]. This allows us to eliminate a bulky LNA stage typically used in some other systems [30]. The baseband signal is digitized at a sampling rate of 200 Hz with a National Instruments (NI) USB-6009 Multifunction Data Acquisition Unit (DAQ), which uses a 14-bit ADC with a maximum sampling rate of 48 kS/s, adequate for vital signs detection resolution after baseband filtering [31].

## 4.2 Phase noise and Range Correlation

The mixer LO port and the transmitted signal utilize the same source to take advantage of range correlation, which harnesses the existing correlation between the

reflected physiologically phase-modulated signal and the local oscillator (LO) signal of the down-converting mixers to minimize the baseband phase noise. The two orthonormal baseband signals obtained after mixing are given as [29],

$$B_I(t) = \cos \left[ \theta + \frac{4\pi x(t)}{\lambda} + \Delta\phi(t) \right] \quad (4.1)$$

and

$$B_Q(t) = \sin \left[ \theta + \frac{4\pi x(t)}{\lambda} + \Delta\phi(t) \right] \quad (4.2)$$

Here  $B_I$  denotes the in-phase baseband signal channel,  $B_Q$  denotes the 90° out-of-phase or quadrature baseband signal channel,  $\theta$  is phase term dependent on the position of the subject with respect to the NCVS sensor and  $\Delta\phi(t)$  is the residual phase noise after range-correlation. As can be seen in equations (4.1) and (4.2), the only time-varying term apart from the cardio-pulmonary data is the residual phase noise and hence is a cause for the degradation of sensitivity of the NCVS sensor system (assuming no clutters). As per the elaborate study in [40], this baseband phase noise,  $S_{\Delta\phi}(f_o)$  at the offset frequency of  $f_o$  can be expressed as,

$$S_{\Delta\phi}(f_o) = S_{\phi}(f_o) \left[ 4 \sin^2 \left( 2\pi \frac{Rf_o}{c} \right) \right] \quad (4.3)$$

Here  $S_{\phi}(f_o)$  denotes the phase-noise of the RF or LO signal,  $c$  is the velocity of propagation of the electromagnetic RF wave and  $R$  is the range of the target. The term  $\frac{Rf_o}{c}$  in equation (4.3) for NCVS systems will be on the order of  $10^{-9}$ , thus allowing for small-angle approximation [32]. Simplifying equation (4.3) using the small-angle approximation, the residual baseband phase-noise can be expressed as [29],

$$S_{\Delta\phi}(f_o) \approx S_{\phi}(f_o) \left[ 16\pi^2 \frac{R^2 f_o^2}{c^2} \right] \quad (4.4)$$

From equation (4.4), it can be observed that the baseband residual phase noise increases with the increase in target range  $R$  as well as with the increase in the oscillator phase noise  $S_{\phi}(f_o)$ , thus making it a critical system constraint. Importantly, it can be seen that to maintain a constant baseband residual phase noise for higher target ranges, it is imperative to lower the oscillator phase noise [29]. Additionally, for any range, a lower oscillator phase noise will improve the sensitivity and robustness of the NCVS sensor system, which is critical for physiological monitoring. In this regard, a frequency synthesizer was used instead of a VCO as one of the improvements in the 4<sup>th</sup> generation hardware developed at Dr. Lie's lab. A frequency synthesizer uses the phase-locked loop mechanism to achieve a stable oscillation frequency in comparison to the free-running VCO [74]. A phase-noise performance comparison (based on the manufacturer's datasheet) between the free-running VCO (Minicircuits JTOS-2700+) used in our 3<sup>rd</sup> generation hardware and the 2.4GHz frequency synthesizer (Minicircuits KSN-2457A-1C19+) used in the 4<sup>th</sup> generation hardware is presented in Table.4.1. It can be seen that the frequency synthesizer, as expected exhibits a phase-noise performance, which is almost ten times (20 dB) better at every offset frequency. As per equation (4.4), this improvement should proportionally translate to lower baseband residual phase noise, resulting in more sensitive and robust NCVS sensors.

Table.4.1 Phase noise performance comparison

Oscillator	SSB Phase Noise			
	@ 1 kHz offset	@ 10 kHz offset	@ 100 kHz offset	@ 1 MHz offset
JTOS-2700+	-72 dBc/Hz	-94 dBc/Hz	-114 dBc/Hz	-134 dBc/Hz
KSN-2457A-1C19+	-92 dBc/Hz	-110 dBc/Hz	-135 dBc/Hz	-154 dBc/Hz

### 4.3 Antenna characterization - Directivity and Radiation patterns

Directivity of an antenna is the ratio of the radiation intensity in a given direction from the antenna to the radiation intensity average over all directions [75]. It can also be understood as the power density in a particular direction relative to the total power radiated in all directions [76]. The directivity of antenna is a figure of

merit which specifies how focused the antenna is for both transmitting and receiving signals. NCVS sensor systems are required to sense cardio-pulmonary movements, which include heavily attenuated cardiac movements at the surface of the chest, thereby making the directivity of the antenna a factor in deciding the sensitivity of the sensor. Patch antennas have been popular and have been used for several Doppler-based NCVS systems [29], [30]. Typically this type of antennas offers a gain close to 7 dBi with a half –power beamwidth (HPBW) greater than 80°. It is expected that the low directivity of the antennas, however, can be responsible for clutter and noise pickup. Anything apart from the physiologically phase modulated cardio-pulmonary signal can be understood as clutter or noise, therefore at least qualitatively it is expected that a NCVS sensor system using a narrower HPBW antenna may achieve a better SNIR (signal-to-noise-plus-interference-ratio) performance than an identical sensor system with a larger HPBW antenna. To verify this effect, our NCVS sensor was tested utilizing two antennas, one for Tx and one for Rx, where each antenna was characterized and tested for continuous heart and respiration rates monitoring. The different types of antennas used include Yagi, log-periodic, patch and helical [43], where no combination of antennas was used for the experiment. Except for the helical antenna, which was custom built in Dr. Lie’s lab by Mr. Alex Boothby and Dr. Jerry Lopez [43], all other antennas are commercial-off-the-shelf (COTS) items.

Table.4.2 Basic antenna characteristics based on the radiation patterns.

Antenna	Gain	Frequency	E-H plane
Helical	9.8 dB°	2.4-2.5 GHz	Symmetric
Yagi	7 dB	2.4-2.48 GHz	Asymmetric
Log-Periodic	7 dB	2.4-2.6 GHz	Asymmetric
Patch	7.5 dB	2.4-2.6 GHz	Symmetric

The antenna radiation pattern is defined as a graphical representation of the radiation properties of the antenna as a function of space co-ordinates. The radiation properties include power flux density, radiation intensity, field strength, directivity phase or polarization, etc. [75]. As shown in Fig. 4.4, the radiation patterns are made up of radiation lobes which depict the radiation intensity with respect to different

angular direction [75]. The major lobe is the radiation lobe containing the maximum radiation, whereas the side-lobes are the radiation lobes in any direction other than the intended lobe [75]. In a plane containing the direction of the maximum of a beam, the angle between the two directions in which the radiation intensity is one-half the maximum value of the beam is defined as the half-power beamwidth (HPBW) or beamwidth of the antenna [75]. This HPBW is used to ascertain the directional nature of the antenna.

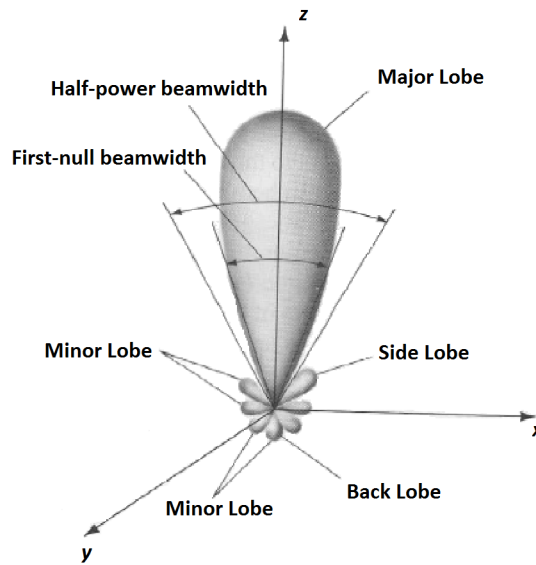


Fig. 4.4 Typical radiation pattern of an antenna. [75]

The antenna radiation patterns were measured and are shown in Fig. 4.5 to Fig.4.8 below, where also shown are the corresponding antennas. The results include individual radiation patterns and the antenna radiation patterns with a parasitic antenna 24 cm apart for both the Tx and Rx cases, respectively. The Tx antenna is the parasitic antenna for the Rx antenna and vice versa, and these two cases are expected to be reciprocal and the same. The results show that the antenna radiation patterns are seemingly unperturbed by the parasitic antennas when used in this system at 24 cm apart (measured from the center feed to center feed).

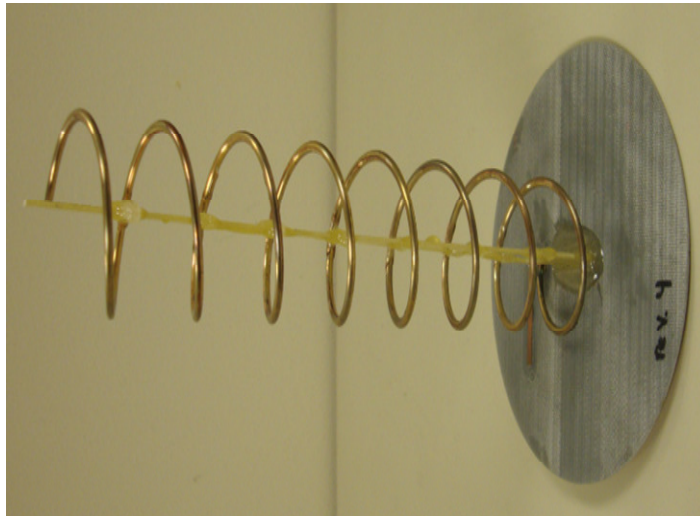
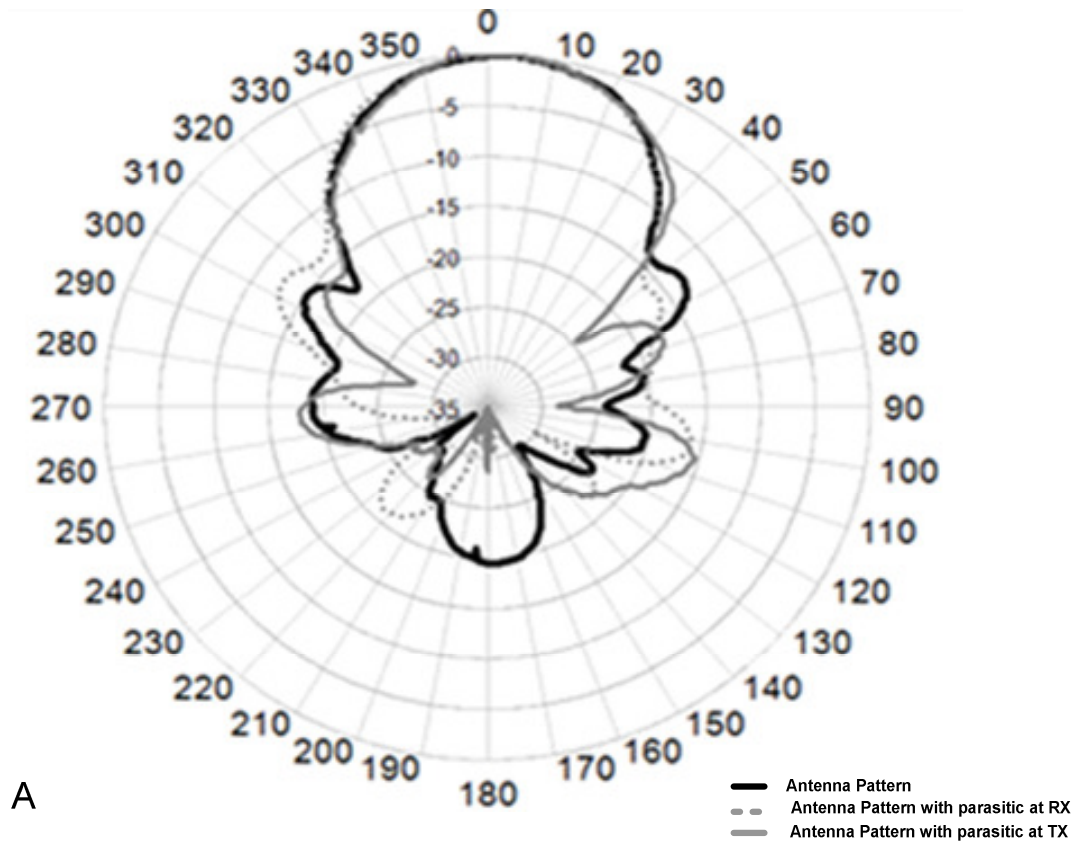


Fig. 4.5 (A) Measured radiation patterns of the custom built helical antenna. (B) The custom built helical antenna

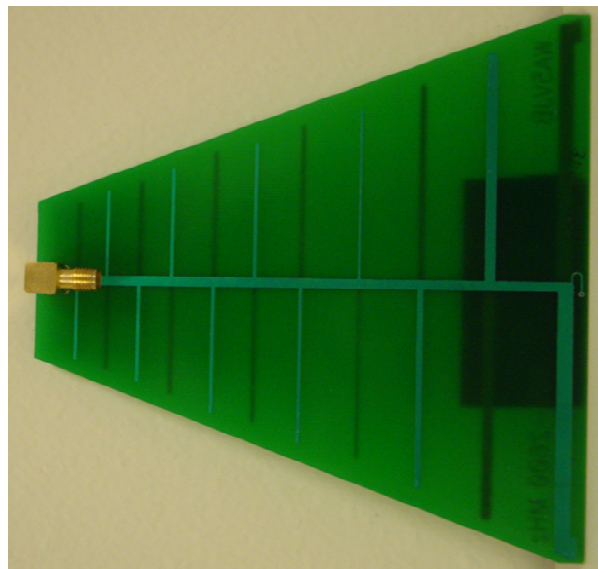
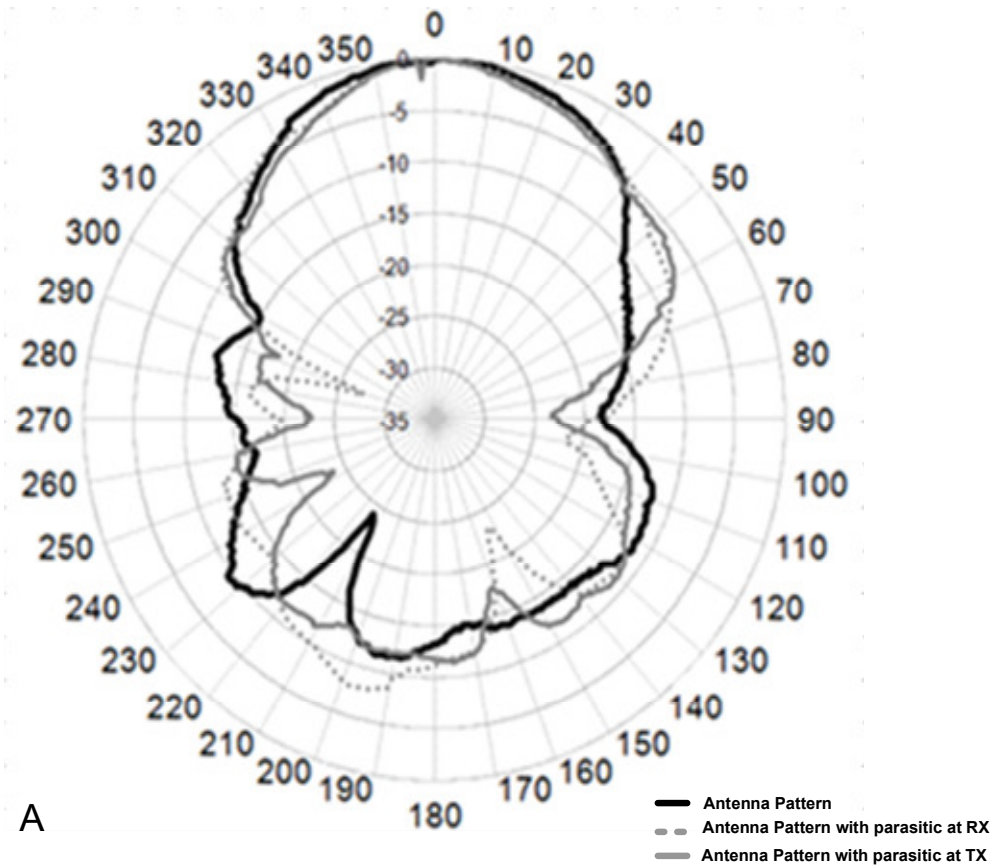


Fig. 4.6 (A) Measured radiation patterns of the Log-periodic antenna. (B) The Log-periodic antenna.

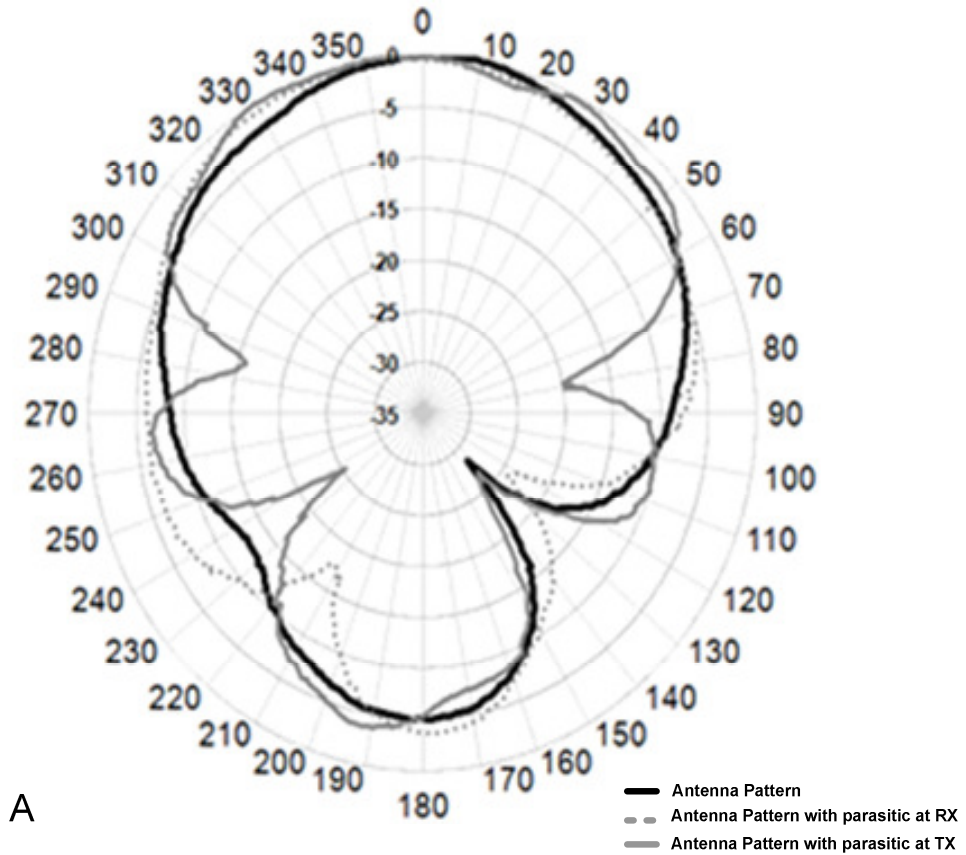


Fig. 4.7 (A) Measured radiation patterns of the patch antenna. (B) The patch antenna.

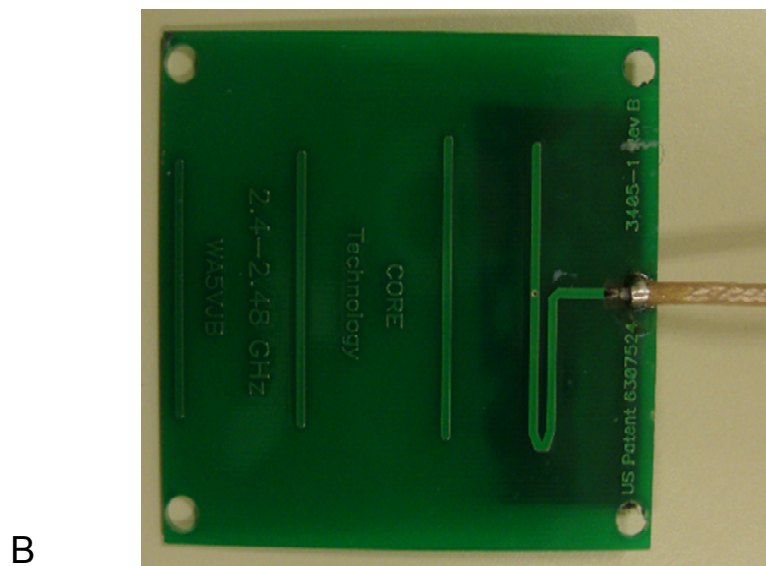
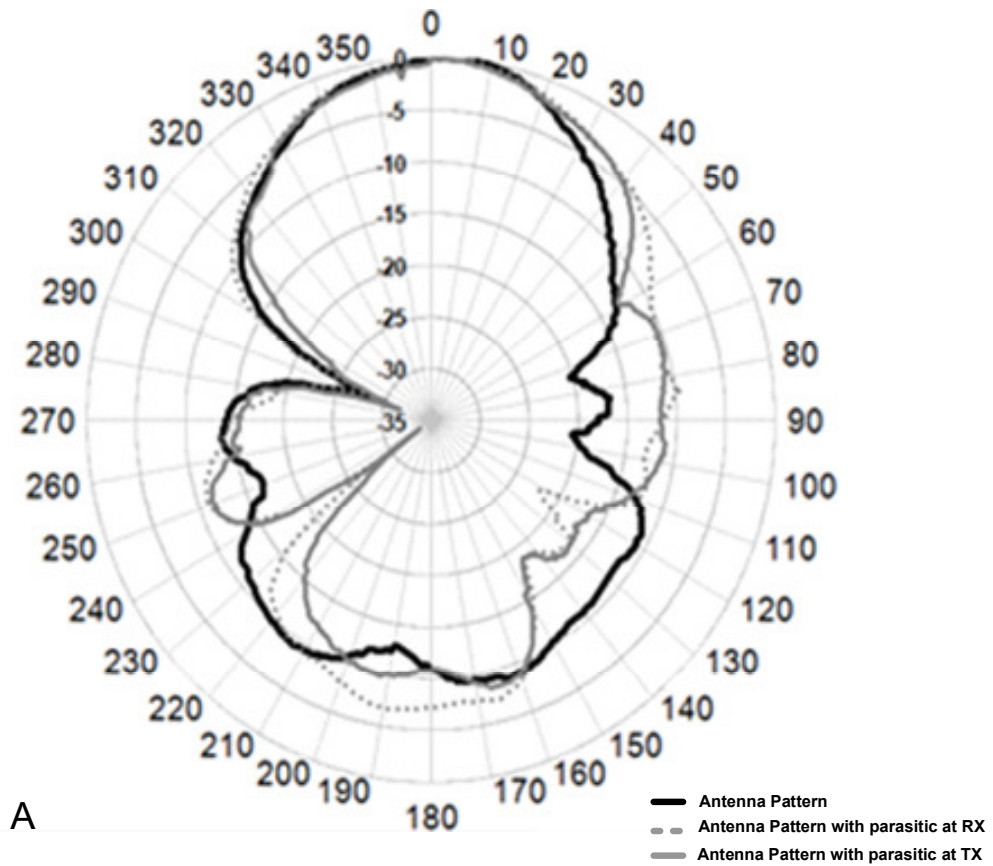


Fig. 4.8 (A) Measured radiation patterns of the Yagi antenna. (B) The Yagi antenna.

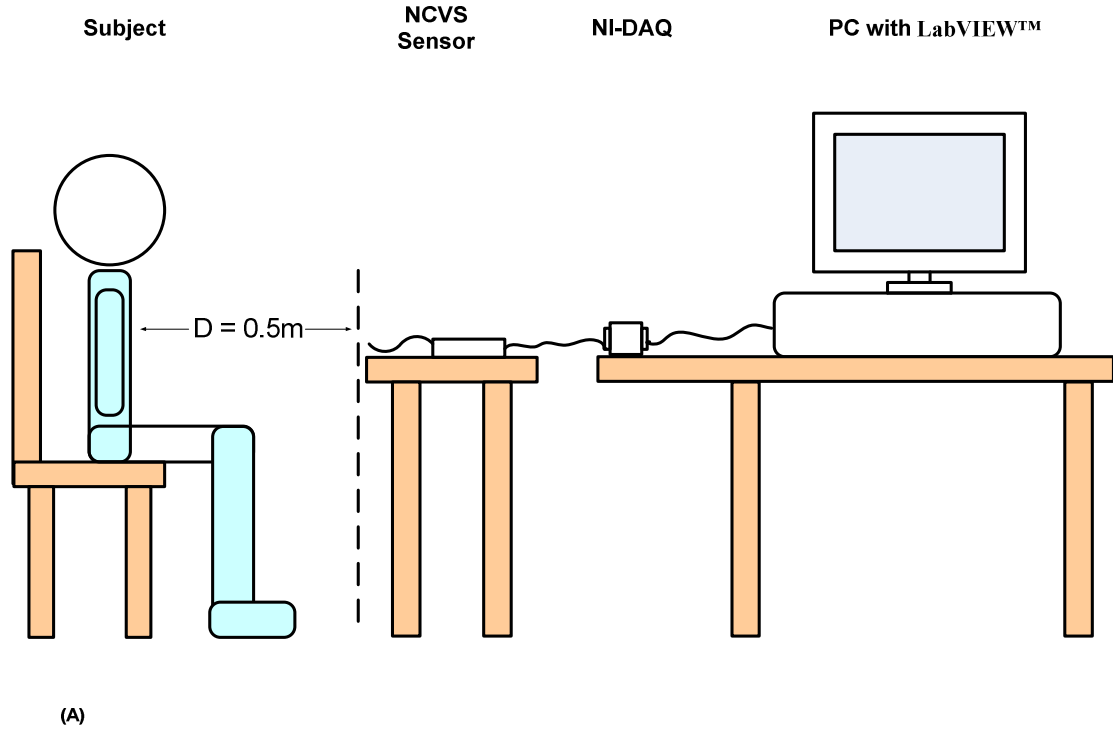
Measured 3-dB beam-width or the half-power beamwidth (HPBW) and the side-lobe level (SLL) for the 4 types of antennas used summarized in Table.4.3. It is clear that the custom helical and Yagi antennas are more directional with better side-lobe rejection.

Table.4.3 Antenna characteristics based on the radiation patterns.

Antenna	Half-power Beamwidth (HPBW)	Side-lobe Level (SLL)
Helical	44.6°	13.1 dB
Yagi	47°	14.2 dB
Log-Periodic	62°	9.4 dB
Patch	92°	5.4 dB

#### 4.4 NCVS system based antenna evaluation setup

Each antenna was tested with the sensor system on three different subjects (student volunteers) for 5 readings on each subject, in the anechoic chamber. The experimental setup is shown in Fig. 4.9, with the subject sitting 50 cm from the antenna radiation plane. Even though the 50 cm distance was fixed, an I/Q based CW Doppler NCVS system will still see a nulling issue that occurs periodically every  $\lambda/4$  distance which, for a 2.4 GHz system is almost equal to 3 cm. This nulling issue happens when the target is placed at 0°, 90°, 180° or 270° from the radiation plane, and results in a large amplitude drop in either the I or Q channel response. Rather than being a problem, this nulling can be considered as a typical characteristic of Doppler-based NCVS systems. The conventional solutions to overcome nulling are to use quadrature receivers with good demodulation algorithms insensitive to nulling, and to improve the system's dc offset and SNR (using good matching with low-noise amplifiers). Since our main goal is to clearly compare and quantify the antenna performance for optimizing our sensor system, we have placed the subjects in a non-nulling plane of reference for each antenna for the front vital signs readings only. This allows us to attribute any performance improvements/issues to the antenna selection, rather than the positioning of the subject. Matlab™ and LabVIEW™ were used to process the data for antenna performance analysis.



Helical, Yagi, Log-periodic and Patch antennas were replaced at this Tx/Rx port

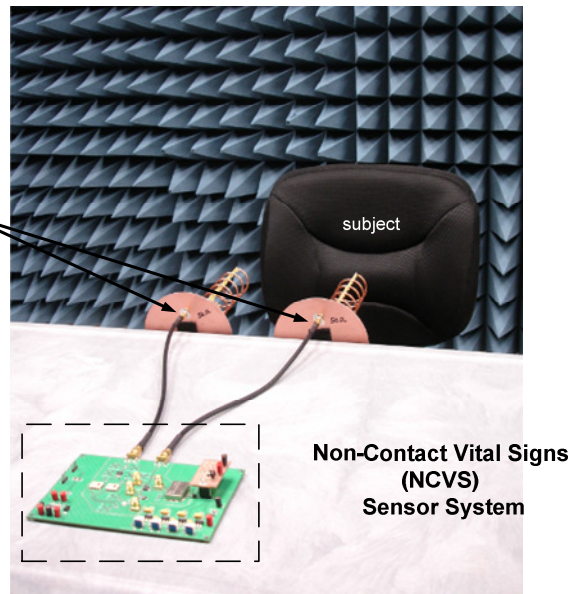


Fig. 4.9 (A) Diagrammatic representation of the NCVS sensor measurement set up; (B) The test setup in the anechoic chamber at Dr. Lie's lab.

To verify the performance of the system shown in Fig. 4.1, different subjects' vital signs were measured from the front, left, right and back sides using our portable NCVS system. The data was taken continuously for 4 minutes on each subject for each sitting, including a 30 sec filter settling time (this long time was because we used large number of taps for the filters to achieve better stop-band attenuation). The subjects were asked to keep as motionless as possible during the measurement to prevent motion artifacts and to breathe normally. The results were initially filtered in parallel with a low-pass filter having a cut-off of 0.66 Hz for respiration rate and a band-pass filter for heart rate having a passband from 0.9 Hz to 3 Hz. The filters were implemented in LabVIEW™ with real time processing blocks. A transducer sensor (UFI-1010) attached to the subject's finger was used as the reference for heart rate measurement. The extraction of the heart rate was done by taking a time domain autocorrelation, followed by FFT of the output and finally with frequency domain peak detection to find the frequency of the heart and respiration signals [34]. This signal processing approach has been shown to be very effective with our system. A flow diagram depicting the various steps of the signal processing algorithm used for the antenna evaluation is shown in Fig. 4.10. The results are plotted using box-whisker plots in Fig. 4.11, showing 45,000 data points for each antenna orientation. The error readings are extracted from the middle 120s of each 240s data set. The first 60s was removed to avoid disruptions from filter settling, and the last 60s was removed to avoid possible false data due to the subjects' restlessness at the end of the readings [29]. Heart rate error is calculated at a rate of 25 Hz, leading to a total data set of 3,000 points per 120s reading. Five readings each are taken on three subjects for every orientation, for a total of fifteen per side, which was concatenated leading to a total data set of 45,000 points per orientation.

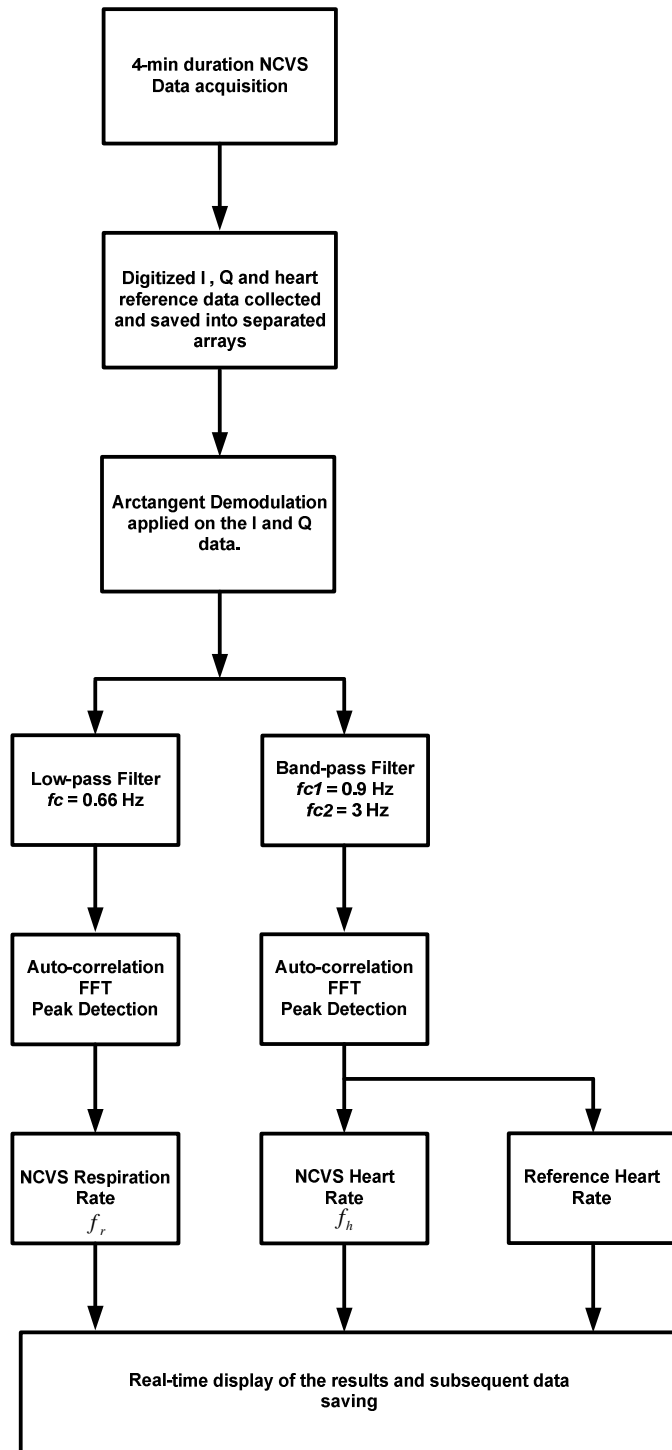


Fig. 4.10 The flow chart for the LabVIEW™ code used in antenna evaluation using NCVS system at Dr. Lie's lab.

#### **4.5 Experimental results and analysis**

The helical antenna achieves a tighter error rate than the Yagi, patch and log periodic antennas, as this can be seen in Fig. 4.11. The inter-quartile range for the error rates of different antennas is summarized in Table 4.4. The plot shows the values for Rate Error in Beats per Minute (bpm). The data can be best used to directly compare antenna performance without nulling effects. The reason for this performance can be directly attributed to the amount of directivity found in the antenna and its symmetry in the magnetic (H) and electric (E) planes. For example, the 3dB BW of the custom designed helical antenna was measured as  $44.6^\circ$ , versus  $62^\circ$  and  $92^\circ$  for the log-periodic and patch antennas, respectively. The Yagi antenna's 3dB BW is similar to that of the helical antenna, but its pattern is not symmetrical across the E and H planes (about  $60^\circ$  BW in the H plane). This antenna performance data reflects a raw system without the use of baseband DC error or subject movement compensation. The rest of the readings from the back, left and right sides were taken only as a performance merit of the system and cannot be directly correlated to compare the antenna performance as they were not adjusted for nulling positions.

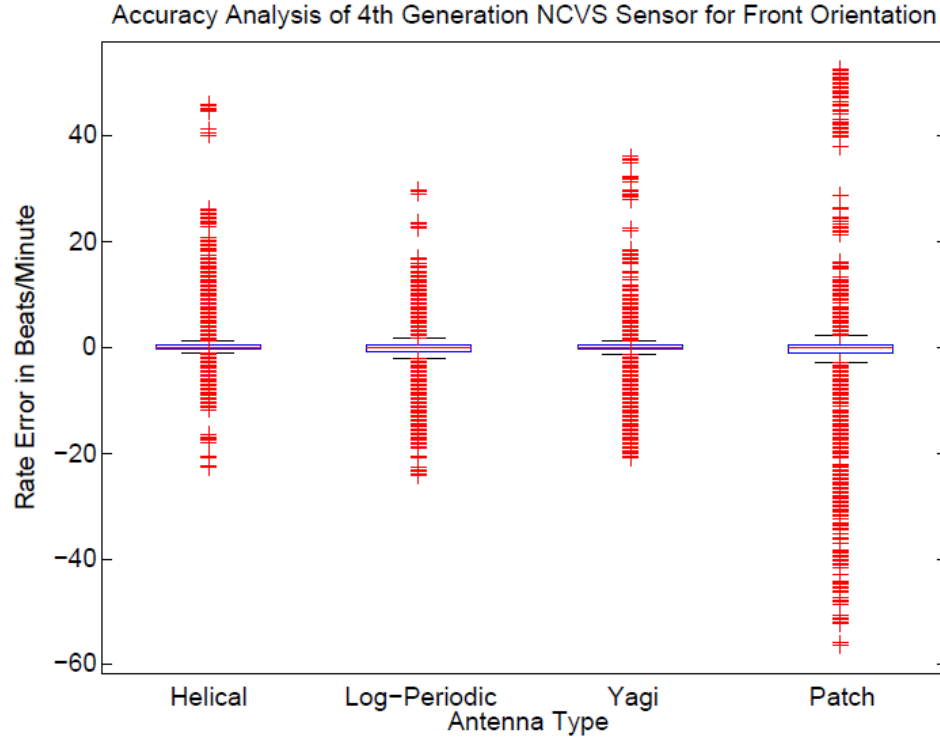


Fig. 4.11 Box-Whisker plots for different antennas for *front* readings only.

Table.4.4 Inter-quartile Range (IQR) for different antennas based on Fig. 4.11

Antenna	Inter-quartile Range
Helical	0.53
Yagi	0.65
Log-Periodic	0.98
Patch	1.34

The sensor accuracy and statistics achieved in these experiments for heart rates are summarized in Table 4.5 for front readings of the subjects, which show that the helical antenna outperforms the rest.

Table.4.5 Measured accuracy table for the non-contact vital signs system based on different antennas (for front readings only)

Antenna	Error < 1bpm	Error < 2 bpm	Error < 5 bpm
Helical	74.53	77.91	84.53
Yagi	70.64	77.25	83.33
Log-Periodic	65.04	70.61	76.07
Patch	62.64	67.91	72.73

The time based signal obtained after arctangent demodulation was also extracted from the measurement, as shown in Fig. 4.12. The largest detected signal was obtained by using the helical antenna, which exceeded those from the Yagi and log periodic antennas by close to a factor of 2, indicating a higher gain for the helical antenna.

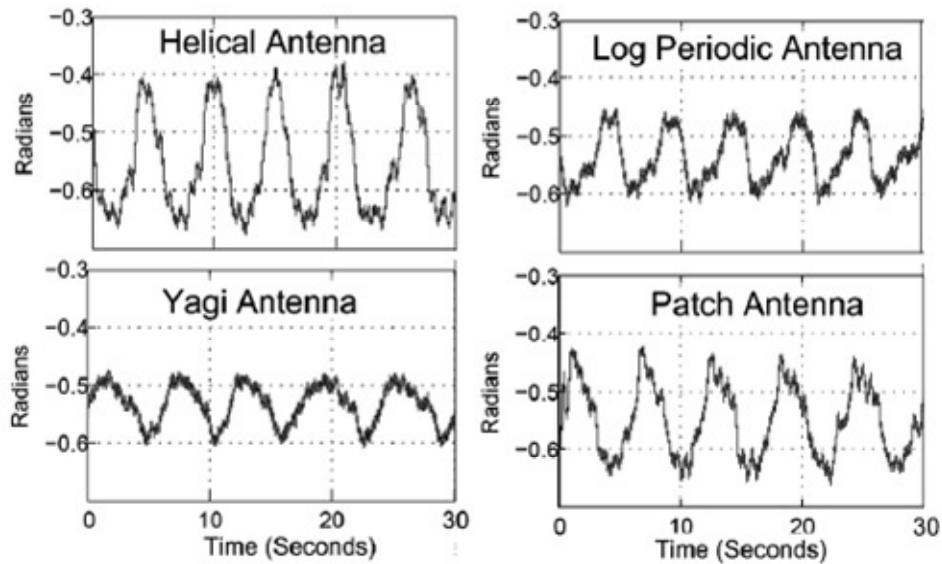


Fig. 4.12 Time based arctangent demodulated signal for heart rate extraction (front readings).

An additional test was performed with equalized antenna gains for all 4 types of antennas, to verify significance of directivity vis-à-vis gain for sensitive systems like our NCVS sensor. As was seen in Fig. 4.12, helical antennas exhibited higher gain, hence 3-dB attenuators were used in both the transmit and receive paths of the setup to offset this additional gain. The box-whisker plot for this experiment is shown in Fig. 4.13, where the performance pattern is similar to the one shown in Fig. 4.11. It was then clearly observed that for signals above the noise floor, the higher directivity of the antenna, rather than the higher gain of the antenna, is mainly responsible for the improved sensor accuracy and increased SNIR. The inter-quartile range for the error rates obtained for the different antennas are shown in Table 4.6

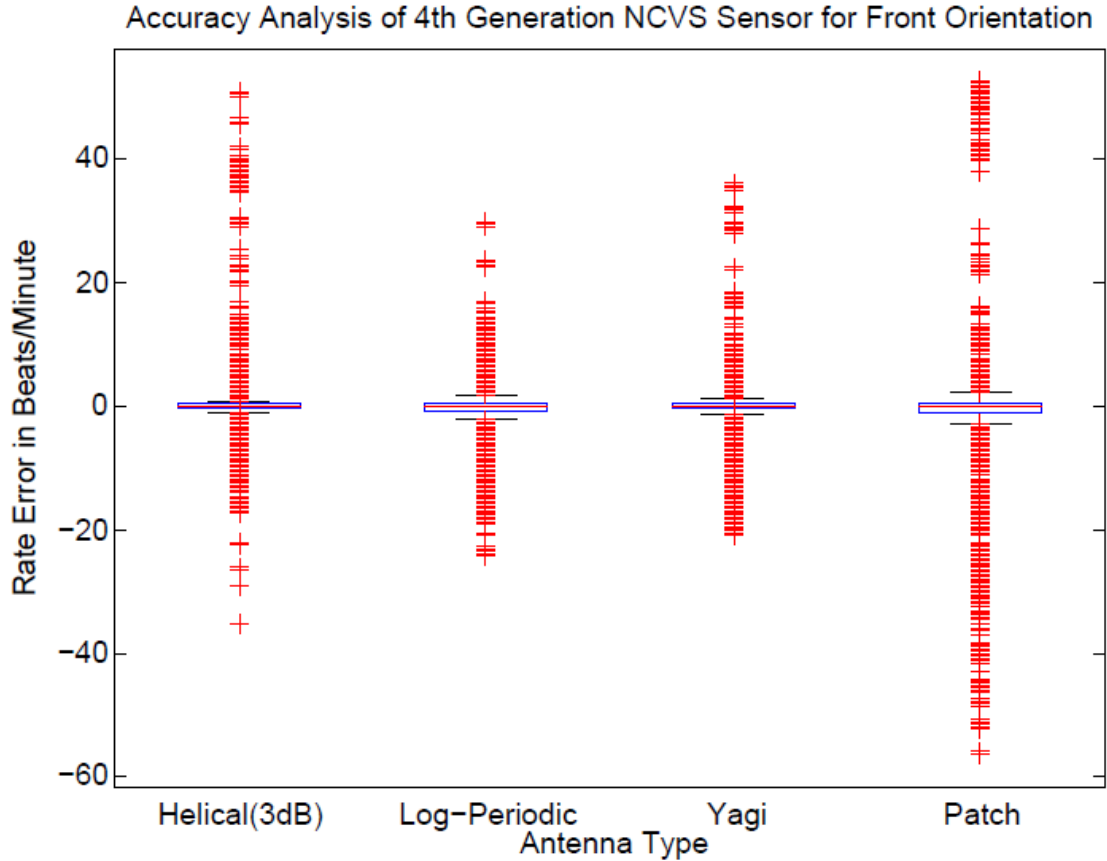


Fig. 4.13 Box-Whisker plots for different antennas for *front* readings only with equalized gains.

Table.4.6 Inter-quartile Range (IQR) for different antennas based on Fig. 4.13

Antenna	Inter-quartile Range
Helical	0.46
Yagi	0.65
Log-Periodic	0.98
Patch	1.34

The sensor accuracy and statistics achieved in the gain-equalization experiment for heart rates are summarized in Table 4.7 for front readings of the subjects. Similar to the previous case, here again the helical antenna outperforms the other participating antennas. The accuracy numbers for helical antenna show a marginal increase but are

in the same ballpark. This increase can probably be attributed to fact that the attenuator in the receive path attenuates the clutter and noise pickup.

Table.4.7 Measured accuracy table of NCVS system for the gain-equalization experiment (for front readings only)

Antenna	Error < 1bpm	Error < 2 bpm	Error < 5 bpm
Helical	78.16	81.83	85.59
Yagi	70.64	77.25	83.33
Log-Periodic	65.04	70.61	76.07
Patch	62.64	67.91	72.73

Moreover, respiration rate was also measured during these experiments with excellent  $\pm 1$  breaths/minute accuracy over 95% of the time. Since the cardiac signal is orders of magnitude smaller than the respiration signal and presents the largest challenges for robust continuous NCVS monitoring, the error of heart rate is expected to be higher compared to the respiration rate [30], [35], [45]. Thus the heart rate data was used to assess system performance with different antennas. The data shown suggests that the increment in signal radian amplitude strength shown in Fig. 4.12, due to the high directivity and symmetric E and H patterns of the helical antenna, can enhance the SNIR of Doppler-based vital signs systems. Further development of the system includes implementing dc offset error corrections and movement detection algorithms to reduce motion artifacts, allowing improvements in system performance

## CHAPTER 5

### CONCLUSION AND FUTURE WORK

Robust, accurate and energy-efficient sensor systems are required for the continuous monitoring of physiological vital signs, and the task is especially challenging and important for the heart rate monitoring. With massive strides made in technology advancement over last few decades, it is now desirable to spread the reach of high-quality health care to as many individuals as possible. This can be realized by providing convenient and cost-effective wireless-assisted living, reliable ambulatory healthcare and wireless-acute-care. One key enabler of such a high-tech revolution of the healthcare industry lies on the versatile low power wireless biosensors, where the analog front-end (AFE) IC design of the cardiac monitoring system is of critical importance, as it not only require to be accurate in sensing the cardiac activities, but also needed to be ultralow-power as it has to stay on throughout the entire operational period of the sensor. Thus, an efficient and skillful design of the AFE IC holds the key to propel the overall healthcare system reform for embracing the “wireless revolution”.

An efficient implementation of the AFE circuitry involves an efficient instrumentation amplifier (INA), which is the first circuit interfacing with the electrode. In this context, research and investigations were done to understand the various CMOS circuit topologies and techniques for low-power and low-noise implementation of the INAs. Chopper-stabilization, which recently has emerged as one of the prevalent techniques to suppress the effect of flicker noise in bio-signal amplifiers, was studied in this thesis. An INA circuit incorporating this technique was designed, simulated and fabricated using a TI proprietary LBC7 0.35 $\mu\text{m}$  BCD process. The measurement results and simulation results were found to be in good agreement. The chopper INA achieved a low  $1/f$  noise of 0.24 $\mu\text{V}$  @10Hz, with a current consumption of less than 2.8 $\mu\text{A}$ . Further circuit analysis for noise and power optimization was done, and a combination of techniques such as the chopper

stabilization, sub-threshold operation and current-scaling were used to design and simulate another INA circuit using the TSMC 0.18 $\mu\text{m}$  analog/RF CMOS process. The post-layout simulation results of which showed improvement over the previous 0.35 $\mu\text{m}$  CMOS chopper INA design, with an impressive sub-100 nV/ $\sqrt{\text{Hz}}$  noise power spectral density.

If a cardiac monitoring system can be built to detect cardiac activities without any contact to the individual being monitored, it can drastically enhance the overall comfort level and experience of heart monitoring, thus making the continuous and ubiquitous heart rate monitoring possible. Investigations were carried out to make the existing PCB-based Doppler-based non-contact vital signs (NCVS) system more reliable and robust. The effect of heart rate sensing based on the different antenna characteristics were studied, and it was shown that the directivity of an antenna is a key factor in determining the detection accuracy. Furthermore, a frequency synthesizer was used in lieu of a simple VCO as the RF signal generator to reduce this residual phase noise and improve frequency stability, thereby improving the sensitivity of the system which is crucial for the detection of the heavily attenuated cardiac signal.

## **5.1 Future Work**

In the continuous pursuit to improve the present systems and designs, a few implementations as listed below are being evaluated.

### **5.1.1 dc-servo loop (DSL) for electrode offset reduction**

Chopper stabilization technique aids in the suppression of the flicker noise as well as the dc-offset exhibited by the amplifier. But in order to suppress the offset presented by the electrodes, a circuit technique known as dc-servo loop (DSL) may need to be implemented. DSL is a switch-capacitor (SC) based technique, which provides a high-pass transfer function in spite of the presence of chopper stabilization.[50], [54]. The DSL technique entails the usage of an additional feedback loop involving a SC integrator and a chopper modulator. The resulting system, though

effective, involves increased design complexity and uncertainties as well as higher power consumption.

### **5.1.2 Active grounding for ECG measurements**

Typically, ECG measurement systems use passive grounding which, even though easier to use, lacks the higher level of attenuation of the 60Hz interference provided by the active feedback based grounding [16]. The active grounding technique not only effectively suppresses the common-mode interference, but also relaxes the overall amplifier requirements for CMRR. The implementation of active grounding enhances the ECG signal quality, thereby making the system more robust and reliable. As the name suggests, there is an additional active element to be used for active grounding, which implies a slightly higher power requirement. But smart utilization of low-power circuit techniques can still make it possible to realize active grounding with considerably low-power consumption [16].

### **5.1.3 System-on-a-Chip (SoC) realization of the NCVS system**

The PCB-based NCVS sensor system will eventually be implemented as a System-on-a Chip (SoC). A SoC realization will improve the sensitivity of the system, as the COTS hardware related mismatches and path losses will be suppressed (such as those caused by discrete baluns and mismatches of COTS parts), thus should be achieving higher signal integrity with smaller form factors. A NCVS-SoC will reduce the overall size, cost and possibly the power requirements of the sensor, thus taking it a big step closer to wide-scale deployments of the NCVS sensors. A high-fidelity RF transceiver will be the core of the NCVS-SoC where an efficient RF low-noise amplifier (LNA), a pair of I/Q passive mixers and a high quality frequency synthesizer and smart DSP with clutter-rejection algorithms would largely determine the overall NCVS system performance.

#### **5.1.4 Harmonic Cancellation for the NCVS sensor system**

The pulmonary signal, being orders of magnitude stronger than the cardiac signal, has harmonics large enough to overwhelm the cardiac signals, and this phenomenon can lead to erratic heart rate detection and reduction of the overall NCVS sensing accuracy. Harmonic cancellation based on least-mean square (LMS) algorithm is being probed to mitigate the interference of the respiration signal harmonics [35]. One way is to estimate the respiration harmonics using weighting functions generated on the basis of minimization of the mean square error. The estimated respiration signal is then deducted in the time-domain from the cardio-pulmonary signal and ideally this cancellation method is expected to improve the sensing of the cardiac signal significantly.

## REFERENCES

- [1] C.G. Caro and J.A. Bloice, "Contactless apnea detector based on radar", *Lancet*, vol 2, no.7731, pp. 959-961, Oct. 1971.
- [2] Schematic representation of normal ECG, in Wikipedia. Retrieved from <http://en.wikipedia.org/wiki/Electrocardiography>
- [3] J.G. Webster, *Medical Instrumentation: Application and Design*, 4<sup>th</sup> ed., John Wiley & Sons, 2009.
- [4] J.A. Warren, R.D. Drehe, R.V. Jaworski, and J.J. Putzke, "Implantable cardioverter defibrillators," *Proc. IEEE*, vol. 84, issue 3, pp. 468-479, March 1996.
- [5] R. Fensli, E. Gunnarson and T. Gundersen, "A wearable ECG-recording system for continuous arrhythmia monitoring in a wireless tele-home-care situation," *Proc. 18<sup>th</sup> IEEE Symp. Comput. Med. Syst.*, pp. 407- 412, 23-24 June 2005.
- [6] J. Welch, F. Guilak and S.D. Baker, "A Wireless ECG Smart Sensor for Broad Application in Life Threatening Event Detection," *Proc. 26<sup>th</sup> Annu. Int. Conf. IEEE EMBS*, vol.2, pp. 3447- 3449, 1-5 Sept. 2004.
- [7] C. Park, P.H. Chou, Ying Bai, R. Matthews and A. Hibbs, "An ultra-wearable, wireless, low power ECG monitoring system," *IEEE Biomed. Circuits Syst.*, pp. 241-244, Nov. 29 2006-Dec. 1 2006.
- [8] C. Assambo and M.J. Burke, "Amplifier input impedance in dry electrode ECG recording," *Annu. Int. Conf. IEEE Eng. Med. Biol. Soc.*, pp. 1774-1777, 3-6 Sept. 2009.
- [9] F. Pini, C. O'Mahony and K.G. McCarthy, "Electrical characterisation of dry microneedle electrodes for portable bio-potential recording applications," *IEEE Int. Conf. Microelectronics Test Structures (ICMTS)*, pp. 87-90, 19-22 March 2012.
- [10] W. H. Ko, M. R. Neuman, R. N. Wolfson, and E. T. Yon, "Insulated active electrodes," *IEEE Trans. Ind. Elect. Contr. Instrum.*, vol. IECI-17, pp. 195-198, 1970.
- [11] R.M. David and W.M. Portnoy, "Insulated electrogram electrodes," *Med Biol. Eng.*, vol. 10, pp. 742-751, 1972.

- [12] C.-L. Chang, C.-W. Chang, H.-Y. Huang, C.-M. Hsu, C.-H. Huang, J.-C. Chiou and C.-H. Luo, "A power-efficient bio-potential acquisition device with DS-MDE sensors for long-term healthcare monitoring applications," *Sensors*, vol. 10(5), pp. 4777-4793, 2010.
- [13] Henry Gray, *Anatomy of the Human Body*, 20<sup>th</sup> ed., Philadelphia: Lea & Febiger, 1918.
- [14] E. Nemati, M.J. Deen and T. Mondal, "A wireless wearable ECG sensor for long-term applications," *IEEE Commun. Mag.*, vol.50, no.1, pp.36-43, January 2012.
- [15] A. Ueno, Y. Akabane, T. Kato, H. Hoshino, S. Kataoka and Y. Ishiyama, "Capacitive sensing of electrocardiographic potential through cloth from the dorsal surface of the body in a supine position: A Preliminary Study," *IEEE Trans. Biomed. Eng.*, vol. 54, no. 4, pp. 759-766, April 2007.
- [16] L. Fay, V. Misra and R. Sarpeshkar, "A micropower electrocardiogram amplifier," *IEEE Trans. Biomed. Circuits Syst.*, vol. 3, no. 5, pp. 312-320, Oct. 2009.
- [17] M. Mirowski, "Standby automatic defibrillator," *Arch. Intern. Med.* vol. 126, pp. 158, 1970.
- [18] J.C. Schuder, H. Stoeckle, J.H. Gold, J.A. West and P.Y. Keskar, "Experimental ventricular defibrillation with an automatic and completely implanted system," *Trans. Amer. Soc. Artif. Int. Organs*, vol. 16, pp. 207, 1970.
- [19] W. Hu, Y-T. Liu, T. Nguyen, B. Dsouza and D.Y.C. Lie, "Ultralow-power analog front-end IC design for an implantable cardioverter defibrillator (ICD)," *2011 IEEE 9th Int. Conf. ASIC (ASICON)*, pp.1018-1021, 25-28 Oct. 2011.
- [20] U. Cho, Y. Jung, S. Lim and J. Kim, "Implantable bio-medical SoC for ICD with wireless communication system," *59<sup>th</sup> Electron. Compon. Technol. Conf.*, pp.1086-1091, 26-29 May 2009.
- [21] A.E. Zadeh, "Nano-power switched-capacitor bandpass filters for medical implantable pacemakers and defibrillators," *51<sup>st</sup> Midwest Symp. Circuits Syst.*, pp.29-32, 10-13 Aug. 2008.

- [22] H.M. Haqqani and H.G. Mond, “The implantable cardioverter-defibrillator lead: principles, progress, and promises,” *Pacing Clin. Electrophysiol.*, vol. 32, pp. 1336-1353, 2009.
- [23] A. Gupta, A. Al-Ahmad and P.J. Wang, “Subcutaneous implantable Cardioverter defibrillator technology”, *Card. Electrophysiol. Clin.*, vol. 1, issue 1, pp. 147-154, December 2009.
- [24] G.H. Brady, W.M. Smith, M.A. Hood, I.G. Crozier, I.C. Melton, L. Jordaens, D. Theuns, R.E. Park, D.J. Wright, D.T. Connelly, S.P. Flynn, F.D. Murqatroyd, J. Sperzel, J. Neuzner, S.G. Spitzer, A.V. Ardashev, A. Oduro, L. Boersma, A.H. Maass, I.C. Van Gelder, A.A. Wilde, P.F. van Dessel, R.E. Knops, C.S. Barr, P. Lupo, R. Capatto and A.A Grace, “ An entirely subcutaneous implantable cardioverter defibrillator,” *N Engl. J Med.*, vol. 363, pp. 36-44, 2010.
- [25] R. Capatto, W.M. Smith, M.A. Hood, I.G. Crozier, L. Jordaens, S.G. Spitzer, A.V. Ardashev, L. Boersma, P. Lupo, A.A Grace and G.H. Brady, “Subcutaneous chronic implantable defibrillation system in humans,” *J Interv. Card. Electrophysiol.*, vol.34(3), pp. 325-32, Sept, 2012.
- [26] C.I. Franks, B.H. Brown and D.M. Johnston, “Contactless respiration monitoring of infants,” *Med. Biol. Eng.*, vol. 14(3), pp. 306-312, May 1976.
- [27] J.C. Lin, J. Kiernicki, M. Kiernicki and P.B. Wollschlaeger, “Microwave apexcardiography,” *IEEE Tran. Microw. Theory and Tech.*, vol. 27, pp. 618-620, 1979.
- [28] K.M. Chen, Y. Huang, J. Zhang, and A. Norman, “Microwave life-detection systems for searching human subjects under earthquake rubble and behind barrier,” *IEEE Trans. Biomed. Eng.*, vol. 27, pp. 105–114, Jan. 2000.
- [29] A.D. Droitcour, “Non-contact measurement of heart and respiration rates with a single chip microwave Doppler radar,” Ph.D. dissertation, Dept. Elect. Eng., Stanford University, CA, 2006.
- [30] B.K. Park, O. Boric-Lubecke and V. Lubecke, “Arctangent demodulation with dc offset compensation in quadrature Doppler radar receiver systems,” *IEEE Trans. Microw. Theory Tech.*, vol. 55, no. 5, pp. 1073-1079, 2007.

- [31] R. Ichapurapu, S. Jain, M.U. Kakade, D.Y.C. Lie and R.E. Bannister, "A 2.4GHz non-contact biosensor system for continuous vital-signs monitoring on a single PCB," *Proc. IEEE ASICON*, pp. 925-928, 2009.
- [32] A.D. Droitcour, O. Boric-Lubecke, V. Lubecke, J. Lin and G.T.A. Kovacs, "Range correlation and I/Q performance benefits in single chip silicon Doppler radars for non-contact cardiopulmonary monitoring," *IEEE Trans. Microw. Theory Tech.*, vol. 52, no. 3, pp. 838-848, March 2004.
- [33] B.K. Park, S. Yamada, O. Boric-Lubecke, V. Lubecke, "Single-channel receiver limitations in Doppler radar measurements of periodic motion," *IEEE Radio Wireless Symp.*, pp. 99- 102, 17-19 Jan. 2006.
- [34] R. Ichapurapu, "A 2.4GHz non-contact biosensor system for continuous vital-signs monitoring", M.S. Thesis, Dept. Elec. Comp. Eng., Texas Tech University, TX, 2010.
- [35] D.R. Morgan and M.G. Zierdt, "Novel signal processing techniques for Doppler radar cardiopulmonary sensing," *Signal Process.*, vol. 89, issue 1, pp. 45-66, January 2009.
- [36] V. Das, A. Boothby, R. Hwang, T. Nguyen, J. Lopez and D.Y.C. Lie, "Antenna evaluation of a non-contact vital signs sensor for continuous heart and respiration rate monitoring," *IEEE Topical Conf. Biomed. Wireless Technol., Netw. Sens. Syst. (BioWireleSS)*, pp. 13-16, 15-18 Jan. 2012.
- [37] M. Valkama, M. Renfors and V. Koivunen, "Advanced methods for I/Q imbalance compensation in communication receivers," *IEEE Trans. Signal. Process.*, vol. 49, no. 10, pp. 2335-2344, Oct 2001.
- [38] B.K. Park, V. Lubecke, O. Boric-Lubecke and A. Host-Madsen, "Center tracking quadrature demodulation for a Doppler radar motion detector," *Microw. Symp. IEEE/MTT-S Int.*, pp. 1323-1326, 3-8 June 2007.
- [39] A.M. Vergara, O. Boric-Lubecke and V. M. Lubecke, "DC information preservation for cardiopulmonary monitor utilizing CW Doppler radar," *30<sup>th</sup> Annu. Int. Conf. IEEE Eng. Med. Biol. Soc.*, pp. 1246-1249, 20-25 Aug. 2008.
- [40] M.C. Budge Jr. and M.P. Burt, "Range correlation effects on phase and amplitude noise," *Proc. IEEE Southeastcon, Charlotte, NC*, pp. 5-9, 1993.

- [41] W. Hu, D.Y.C. Lie, M.U. Kakade, R. Ichapurapu, S. Mane, J. Lopez, Y. Li, C. Li, R.E. Banister, A. Dentino, T. Nguyen, S. Zupancic and J. Griswold, "An intelligent non-contact wireless monitoring system for vital signs and motion detection," *Intl Conf. Syst. Sci. Eng. (ICSSE)*, pp. 190-194, 1-3 July 2010.
- [42] R. Ichapurapu, S. Jain, G. John, T. Monday, D.Y.C. Lie, R.E. Banister and J. Griswold, "A 2.4GHz non-contact biosensor system for continuous vital-signs monitoring," *IEEE 10<sup>th</sup> Annu. Wireless Microw. Technol. Conf., WAMICON '09*, pp. 1-3, 20-21 April 2009.
- [43] A. Boothby, R. Hwang, V. Das, J. Lopez and D.Y.C. Lie, "Design of Axial-mode Helical Antennas for Doppler-based continuous non-contact vital signs monitoring sensors," *IEEE Radio Wireless Symp. (RWS)*, pp. 87-90, 15-18 Jan. 2012.
- [44] B. Razavi, *RF Microelectronics*, 2<sup>nd</sup> ed. Upper Saddle River, NJ: Prentice-Hall, 2011.
- [45] B.-J. Jang, S.-H. Wi, J.-G. Yook, M.-Q. Lee, and K.-J. Lee, "Wireless bio-radar sensor for heartbeat and respiration detection," *Prog. Electromag. Research C*, vol. 5, pp. 149-168, 2008.
- [46] A. Droitcour, A. Vergara, T. Shing, C. E. Hourani, R. Nakata, I. Mostafanezhad, S. Miyasato, "Systems and methods for non-contact multiparameter vital signs monitoring, apnea therapy, sway cancellation, patient identification and subject monitoring sensors,". *U.S. Patent 002,234,8A1*, Jan 26, 2012.
- [47] R. F. Yazicioglu, P. Merken, R. Puers and C. V. Hoof, "A 60 $\mu$ W 60nV/ $\sqrt{\text{Hz}}$  readout front-end for portable biopotential acquisition systems," *IEEE J. Solid-State Circuits*, vol. 42, no.5, pp. 1100-1109, May 2007.
- [48] N. Verma, A. Shoeb, J. Bohorquez, J. Dawson, J. Guttag and A. Chandrakasan, "A micro-power EEG acquisition SoC with integrated feature extraction processor for a chronic seizure detection system," *IEEE J. Solid-State Circuits*, vol. 45, no. 4, pp. 804-816, April 2010.
- [49] C. Assambo and M. J. Burke, "Amplifier input impedance in dry electrode ECG recording," *Annu. Int. Conf. IEEE Eng. Med. Biol. Soc. (EMBC)*, pp. 1774-1777, 3-6 Sept. 2009.

- [50] T. Denison, K. Consoer, W. Santa, A. Avestruz, J. Cooley and A. Kelly, “A  $2\mu\text{W}$   $100\text{nV}/\sqrt{\text{Hz}}$  chopper-stabilized instrumentation amplifier for chronic measurement of neural field potentials,” *IEEE J. Solid State Circuits*, vol. 42, no. 12, pp. 2934-2945, December 2007.
- [51] Analog Devices Inc., “ADAS1000 – low-power, five electrode electrocardiogram (ECG) analog front-end,” *ADAS1000 Data Sheet, Rev.*, Aug 2012.
- [52] Texas Instruments, “ADS1292R – low-power, 2-channel, 24-bit analog front-end for biopotentials measurements”, *ADS1292R Data Sheet, Rev. B*, Sept 2012.
- [53] W. Wattanpanitch, M. Fee and R. Sarpeshkar, “An energy efficient micropower neural recording amplifier,” *IEEE Trans. Biomed. Circuits Syst.*, vol. 1, no. 2, pp 136-147, Jun 2007.
- [54] Q. Fan, F. Sebastiano, J. H. Huijsing and K. A. A. Makinwa, “A  $1.8\mu\text{W}$   $60\text{nV}/\sqrt{\text{Hz}}$  capacitively-coupled chopper instrumentation amplifier in 65nm CMOS for wireless sensor nodes,” *IEEE J. Solid State Circuits*, vol. 46, no. 7, pp 1534-1543, July 2011.
- [55] P. K. Chan, K. A. Ng and X. L. Zhang, “A CMOS chopper-stabilized differential difference amplifier for biomedical integrated circuits,” *47<sup>th</sup> IEEE Intl. Midwest Symp. Circuits Systems*, vol. III, pp. 33-36, 2004.
- [56] C.Enz and G.Temes, “Circuit techniques for reducing the effects of op-amp imperfections: autozeroing, correlated double sampling and chopper stabilization,” *Invited Paper, Proc. IEEE*, vol. 84, no. 11, pp. 1584-1612, November 1996.
- [57] J. Guo, J. Yuan, J. Huang, J. K-Y. Law, C-K. Yeung and M. Chan, “ $32.9\text{nV}/\text{rt Hz}$   $-60.6$  dB THD dual-band micro-electrode array signal acquisition IC,” *IEEE J. Solid State Circuits*, vol. 47, no. 5, pp. 1209-1220, May 2012.
- [58] Paul R. Gray and Robert G. Meyer, “MOS operational amplifier design – a tutorial overview,” *Special Papers, IEEE J. Solid State Circuits*, vol. SC-17, no. 6, pp. 969-982, Dec 1982.
- [59] C. Enz, E. A. Vittoz and F. Krummenacher, “A CMOS chopper amplifier,” *Invited Paper, IEEE J. Solid-State Circuits*, vol. SC-22, no.3, pp 335-342, June 1987.

- [60] E. Sackinger and W. Guggenbuhl, "A versatile building block: the CMOS differential difference amplifier," *IEEE J. Solid-State Circuits*, vol. SC-22, no. 2, pp. 287-294, April 1987.
- [61] P. E. Allen and D. R. Holberg, *CMOS Analog Circuit Design*, 2<sup>nd</sup> ed. New York: Oxford University Press, 2003.
- [62] J. M. Rabaey, A. Chandrakasan and B. Nikolic, *CMOS Analog Circuit Design*, 2<sup>nd</sup> edition. Upper Saddle River, NJ, Prentice-Hall, 2002.
- [63] R.R. Harrison and C. Charles, "A low-power low-noise CMOS amplifier for neural recording applications," *IEEE J. Solid-State Circuits*, vol. 38, no. 6, pp. 958-965, June, 2003.
- [64] C. Qian, J. Parramon and E. Sánchez-Sinencio, "A micropower low-noise neural recording front-end circuit for epileptic seizure detection", *IEEE J. Solid-State Circuits*, vol. 46, no. 6, pp. 1392-1405, June 2011.
- [65] R. Wu, K. A. A. Makinwa and J. H. Huijsing, "A chopper current feedback instrumentation amplifier with 1mHz  $1/f$  noise corner and an ac-coupled ripple reduction loop," *IEEE J. Solid-State Circuits*, vol. 44, no. 12, December 2009.
- [66] F. Silveria, D. Flandre and P. G. A. Jespers, "A  $g_m/I_D$  based methodology for the design of CMOS analog circuits and its application to the synthesis of a silicon-on-insulator micropower OTA," *IEEE J. Solid-State Circuits*, vol. 31, no. 9, pp. 1314-1319, September 1996.
- [67] P. R. Gray, P. J. Hurst, S. H. Lewis and R. G. Meyer, *Analysis and Design of Analog Integrated Circuits*, 5<sup>th</sup> ed. New York: Oxford University Press, 2009.
- [68] R. E. Kalbunde, *Cardiovascular Physiology Concepts*, 2<sup>nd</sup> ed, Lippincott Williams and Wilkins, 2011.
- [69] A. L. Goldberger, L. A. N. Amaral, L Glass, J. M. Hausdorff, P. Ch. Ivanov, R. G. Mark, J. E. Mietus, G. B. Moody, C. -K. Peng and H. E. Stanley, *PhysioBank, PhysioToolkit, and PhysioNet: components of a new research resource for complex physiologic signals*, *Circulation* 101(23):e215-e220, June 2000.
- [70] C.I. Franks, J. B. Watson, B. H. Brown and E. F. Foster, "Respiratory patterns and risk of sudden unexpected death in infancy," *Arch. Dis. Child*; vol. 55(8), pp. 595-604, 1980.

- [71] E. M. Staderini, "UWB radars in medicine," *IEEE AESS Syst. Mag.*, pp. 13-18, January 2002.
- [72] O. Boric-Lubecke, P. -W. Ong, V. M. Lubecke, "10 GHz Doppler radar sensing of respiration and heart movement," *Proc. IEEE 28<sup>th</sup> Annu. Northeast Bioengineering Conf.*, pp. 55-56, 2002.
- [73] T. Lee, *The Design of CMOS Radio-Frequency Integrated Circuits*, 2<sup>nd</sup> ed, Cambridge University Press, 2009.
- [74] F. Ellinger, *Radio-Frequency Integrated Circuits and Technology*, Springer-Verlag Berlin Heidelberg, 2007
- [75] C.A. Balanis, *Antenna Theory: Analysis and Design*, 2<sup>nd</sup> ed, John Wiley Sons, 1997.
- [76] W.L. Stutzman., "Estimating directivity and gain of antennas," *IEEE Antennas Propag. Mag.*, vol. 40, no. 4, pp. 7-11, Aug 1998.